JOHANNES KEPLER
UNIVERSITY LINZ

Author
Katharina Matura BSc

Submission
Institute of Physical Chemistry and Linz Institute of Organic Solar Cells

Thesis Supervisor
a. Univ. Prof. Dr. Markus Scharber

October 2023

Ambient Processing of “Green” Non-Fullerene Organic Solar Cells for Light-Soaking Stability Tests

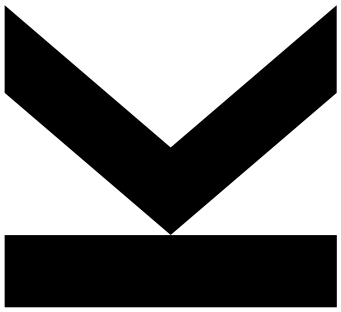

Master’s Thesis

to obtain the academic degree of

Diplom-Ingenieurin

in the Master’s Program

Chemistry and Chemical Technology

JOHANNES KEPLER UNIVERSITY LINZ
Altenberger Straße 69
4040 Linz, Austria
jku.at

SWORN DECLARATION

I hereby declare that the thesis submitted is my own unaided work, that I have not used other than the sources indicated, and that all direct and indirect sources are acknowledged as references.

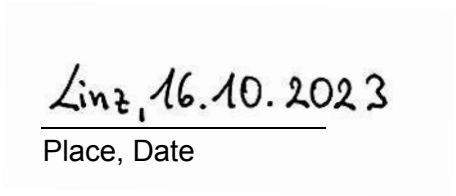

Place, Date

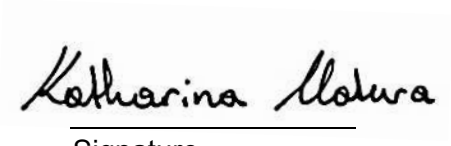

Signature

Acknowledgment

First of all, I want to express my deepest gratitude towards a. Univ. Prof. DI Dr. Markus Scharber for his continuous guidance, support and feedback throughout this work. I am sincerely grateful for his constant commitment to discuss and share his enormous scientific knowledge as well as experience.

I also would like to express my sincere appreciation to o. Univ.-Prof. Mag. Dr. DDr. h.c. Niyazi Serdar Sariciftci for his inspirational talks and for providing me the opportunity to work at his institute together with the LIOS team.

I want to extend my sincere thanks to Priv.-Doz. Dr. Egelhaaf and his research group for visiting their research institution at the Energy Campus. Many thanks to Robin Basu, who has guided me throughout my stay and shared his valuable working experience in the fabrication of organic solar cells. I would also like to gratefully acknowledge the financial support for this collaboration provided by the Emerging Printed Electronics Research Infrastructure.

Next, I want to especially thank my colleagues and friends Felix Mayr and Katarina Gugujonovic, who always had an open ear for my problems and offered me extremely helpful advice and support for conducting the experimental work, as well as for completing this thesis.

I am also grateful to Stefano Favero Costa for his willingness to teach me the Italian language and for making laboratory work, especially *J-V* response measurements, much more entertaining. Moreover, I would like to thank Elisabeth Leeb, Christoph Putz, and Bekele Teklemariam for helping me with my measurement setups and for always being available for discussions.

I want to say thank you to every LIOS team member for contributing to the exceptional working and group climate that I was allowed to experience during my work. A special thank you to all of my colleagues in the big office who provided their encouragement and support not only in the form of group chats but also in sugary delights.

I could not have undertaken this scientific journey without the support of my friends and studying colleagues. In this respect, I want in particular to thank Katharina Nußböck, Sebastian Bönisch, and Florian Kühberger for being my lab partners in crime, for being housemates, and most importantly, for becoming like family to me.

Last but not least, I want to sincerely thank my partner, my parents, my brother, and the rest of my family for their unconditional support and love.

Abstract

Organic solar cells (OSCs) represent a light-weight, low-cost, and solution-processable light-harvesting technology that has been in the research focus for years. Especially lately, OSCs have regained increasing interest for emerging as promising candidates for indoor applications. To achieve their commercialization, an excellent device performance and high operational stability are crucial elements whereby process scale-up requirements such as a non-toxic, non-halogenated solvent, as well as the device fabrication under ambient conditions, should be fulfilled at the same time. In this thesis, an ambient processing procedure for the novel PM6:Y6 material combination was optimized to yield OSCs with a high power conversion efficiency (PCE) of up to 13.5 % using o-xylene as a solvent and 1-chloronaphthalene (CN) or 1,2-dimethylnaphtalene (DMN) as high-boiling solvent additives. Furthermore, the prepared OSCs showed high operational stability over more than 600 hours under indoor light illumination, thereby retaining more than 80 % of their initial PCEs. The low-light intensity power output obtained from already operated devices has resulted in values similar to a standard silicon solar cell. These findings demonstrate the great potential of implementing these OSCs, e.g., into low-power electronic devices such as wireless sensors or radio-frequency identification tags.

Kurzfassung

Organische Solarzellen (OPVs) stellen eine leichtgewichtige, kostengünstige und aus Lösung herstellbare Lichtsammmeltechnologie dar, die seit Jahren im Forschungsmittelpunkt steht. Insbersonders in letzter Zeit, haben OPVs wieder an steigendem Interesse gewonnen aufgrund der Tatsache, dass sie sich auch als vielversprechende Kandidaten für Innenanwendungen herausgestellt haben. Um deren Kommerzialisierung zu erreichen, sind eine hohe Gerätleistung und eine hohe Betriebsstabilität elementar, wobei auch prozessvergrößerdene Anforderungen wie einem ungiftigen, nicht halogenierten Lösungsmittel und die Geräterstellung unter Umgebungsbedingungen erfüllt werden sollen. In dieser Arbeit wurde das an Luft durchführbare Verarbeitungsverfahren für die neuartige Materialcombination PM6:Y6 optimiert, um, unter Verwendung von *o*-Xylol als Lösungsmittel und 1-Chlornaphthalin (CN) oder 1,2-Dimethylnaphthalin (DMN) als hochsiedende Lösungsmittelzusätze, OPVs mit einem hohen Wirkungsgrad von bis zu 13,5 % zu erhalten. Zusätzlich zeigten die hergestellten Geräte über mehr als 600 Stunden eine hohe Betriebsstabilität unter Innenbeleuchtung und behielten dabei mehr als 80 % ihres urspürunglichen Wirkungsgrades bei. Die aus den bereits betriebenen Geräten gewonnenene Schwachlicht-Leistung wies ähnlichen Werte wie die von einer Standard-Silizium-Solarzelle vor. Diese Ergenisse presentieren das große Potenzial der OPV Implementierung zum Beispiel in elektronische Geräte mit geringem Stromverbrauch wie drahtlose Sensoren oder Radiofrequenz-Indentifikationsetiketten.

Contents

1 Introduction

At the moment, finding a sustainable alternative to fossil fuel-based energy is one of the most critical challenges to satisfy the increasing demand for energy as well as to reduce CO_2 emissions [1,2]. Since the sun irradiates the earth with solar energy in the range of 120 000 TW, which corresponds to 6000 times the global energy demand in 2022 [3], photovoltaics represents a promising technology that has already been under research for years [4]. From 2018 to 2022, the number of PV installations worldwide almost doubled, achieving an output of approx. 1.2 TW [5]. The single-crystalline solar cell is thereby the most prominent device type on the market; however, also other solar cell types are heavily under research with the final goal of commercialization [2]. Organic solar cells (OSCs) represent a cost-efficient [6], light-weight [7], and flexible [2,8] alternative to classical crystalline silicon devices. A primary advantage compared to other technologies is the option to adjust the color, light transparency, and energy levels of the photoactive layer by choosing the corresponding organic donor (D) and acceptor (A) material [9]. Additionally, the fabrication is simple since the photoactive layer can be coated on large areas using solution-based processes [10,11]. All these device characteristics open the door for many versatile applications, e.g., in the fields of building-integrated photovoltaics, indoor power supply, or electronic textiles [7,9].

1.1 Organic Solar Cell

1.1.1 Device Structure

Typical bulk heterojunction (BHJ) organic solar cells (OSCs) are built up in a layered device architecture, as depicted in **Figure 1**. To allow an efficient charge carrier extraction, interlayers are introduced between the photoactive layer and the electrodes [12]. In specific, the electron transport layer (ETL) and the hole transport layer (HTL) are implemented next to the cathode and anode, respectively [12,13]. Since the photoactive layer is enclosed on both sides by the interlayers as well as the electrodes, either a “conventional” or an “inverted” device structure is represented [14]. Both device structures use a transparent conductive oxide (TCO) as the bottom electrode, which is coated onto a transparent substrate (e.g., glass). In this respect, indium tin oxide (ITO) corresponds to a commonly used TCO material since it shows an exceptional performance in the areas of optical transparency as well as electrical conductivity [14–16]. In a normal device structure, an HTL is deposited on top of the bottom electrode. The most frequently used HTL material for organic photovoltaics (OPVs) is PEDOT:PSS (poly(3,4-ethylene dioxythiophene):polystyrene sulfonate) [17], whereby also thin films of transition metal oxides (e.g., nickel(II) oxide, chromium dioxide, and molybdenum

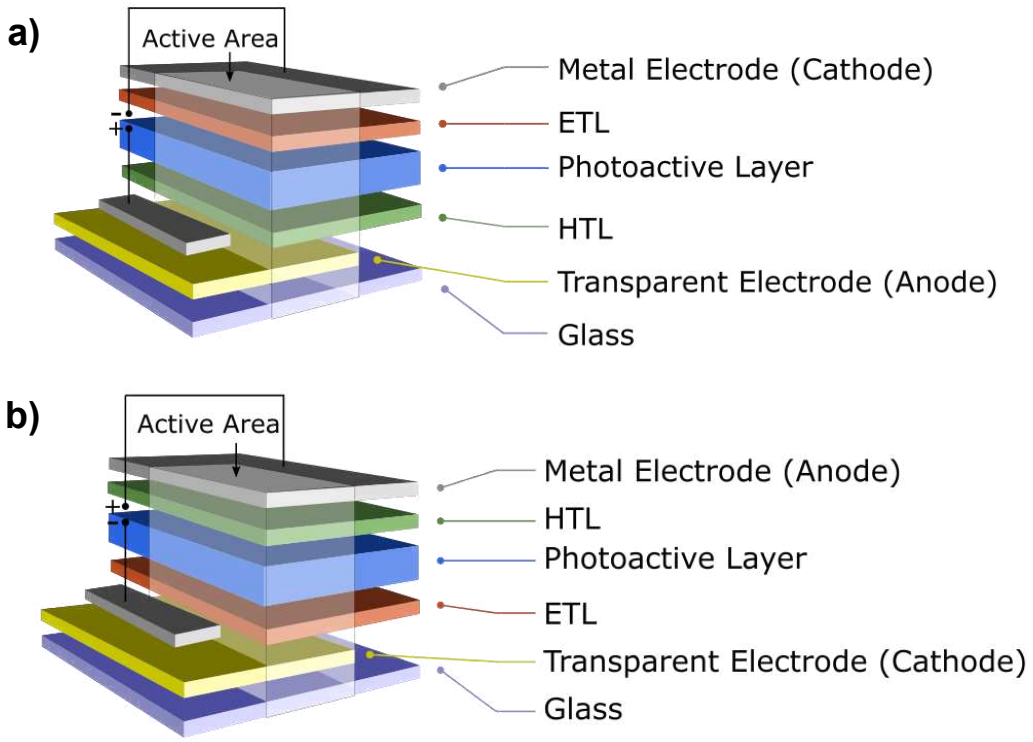

Figure 1. Schematic illustration of **a)** the conventional and **b)** the inverted device structure of a common BHJ OSC.

oxide (MoO_x)) [18,19] have been commonly used. Next, the photoactive layer is deposited, whereby a blend mixture of donor and acceptor material in a specific ratio is used. After this, the ETL layer is processed on top of the absorber layer, followed by an electrode material with a low work function like aluminum or calcium [15,20,21]. In comparison to the normal configuration, in the inverted device structure, the HTL and the ETL layers are switched. In the inverted configuration, commonly used metal oxides for the HTL include MoO_x [19,22], whereas, for the ETL layer, oxides such as zinc oxide (ZnO) [14,22–24,25] or tin(II) oxide (SnO_2) are applied [23]. Following the HTL, a metal anode with a high work function, like silver (Ag), is thermally evaporated [14,22]. Inverted devices offer not only higher stability against oxygen and moisture-related degradation but also a layered architecture that does not include PEDOT:PSS, which is reported to negatively influence the device performance by altering the ITO surface due to its acidic moieties [24,26–28].

The most essential component of an OSC is the photoactive layer. This layer is composed of a defined mixture of a donor and an acceptor material, whereby the choice of material determines the characteristic solar cell parameters [29]. In research, different types of donor molecules are applied, such as conjugated polymers and dye molecules [14]. On the other side, functionalized fullerene molecules correspond to frequently used acceptors [14]. Lately, also

non-fullerene acceptors (NFAs) have become extremely important, which has led to improved PCE of more than 18 % [22]. In many cases, these donor and acceptor materials can be categorized as organic semiconductors [30]. In general, organic semiconductors are classified by overlapping p_z-orbitals of sp_2-hybridized carbon atoms, which create an π-conjugated system, as illustrated in **Figure 2** [31–33]. The π-bond is thereby substantially weaker compared to a σ-bond, which is most often a strong covalent bond within a molecule [33]. Therefore, the energy difference in π-π*-transitions is lower. Typically, π and π* are also known as valence band and conduction band, respectively, which show characteristic energy band gap values of 1.5 - 3 eV [31,34]. Since these energies correspond to wavelengths in the visible spectral range, organic semiconductors are strong absorbers but simultaneously also good emitters [31]. This feature allows tuning the organic D/A materials, e.g., to achieve high absorption when being illuminated with a specific light spectrum [31].
Furthermore, within the photoactive layer, the donor and acceptor domains should be well-distributed in a D-A interpenetrating network-like structure [35]. A large interfacial area between both material types, as well as high-level phase segregation, are thereby crucial for an effective charge carrier formation [20,22,35].

To better understand the origin of this typical device structure as well as how to optimize the performance of a device, in the next chapter, the basic working principle of an OSC will be discussed.

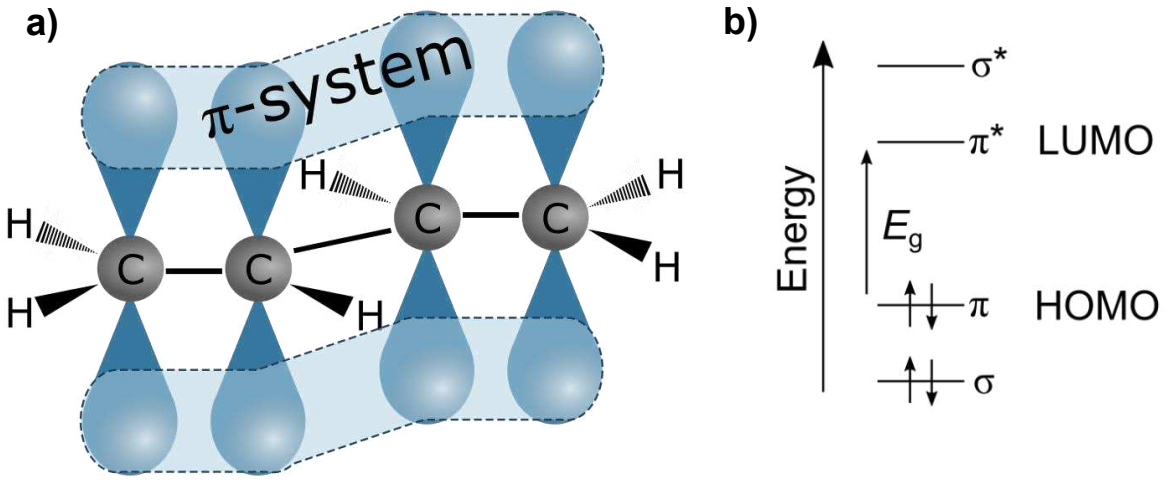

Figure 2. a) Exemplary depiction of an π-conjugated system (here for the 1,3-butadiene molecule), whereby π-electrons are delocalized due to overlapping p_z-orbitals of sp^2-hybridized carbon (C) atoms. **b)** The energy level diagram represents the energy levels of binding (σ and π) and anti-binding (σ* and π*) molecular orbitals. Due to the interaction of several orbitals within the conjugated molecule, a semiconductor-like band gap with a specific band gap energy (E_g) is formed. Redrawn from [33].

1.1.2 Working principle

To be able to harvest solar energy and efficiently convert it into electrical energy, four main mechanisms within OSCs during operation have to be considered (see **Figure 3**) and consequently optimized: 1) Light absorption, excitation and exciton formation, 2) exciton diffusion, 3) exciton dissociation as well as 4) charge carrier transport and collection at the electrodes [14,36].

A prerequisite for the generation of any charged species is the absorption of light. When a photon is absorbed by a photoactive organic material, an electron in the highest occupied molecular orbital (HOMO) is excited into the lowest unoccupied molecular orbital (LUMO). Thus, a bound electron-hole pair, also called exciton, is generated [14]. Since organic materials are known to have a small dielectric constant, the Coulomb attraction force between the bound charges is high. Consequently, the high exciton binding energy of ca 0.2 - 0.5 eV [36] can hardly be surpassed solely by thermal energy present at ambient conditions [14]. The addition of an acceptor material to an organic semiconductor donor polymer is drastically increasing the probability of exciton dissociation into free charge carriers [14,37]. So upon exciton generation in the polymer moieties within the photoactive layer, the exciton diffuses to the interlayer of donor and acceptor domains and will dissociate into free charge carriers by moving the electron from the LUMO of the donor to the HOMO of the acceptor domain [14,38]. Similarly, excitons generated in the acceptor domain can be converted to free-charge carriers by the transfer of

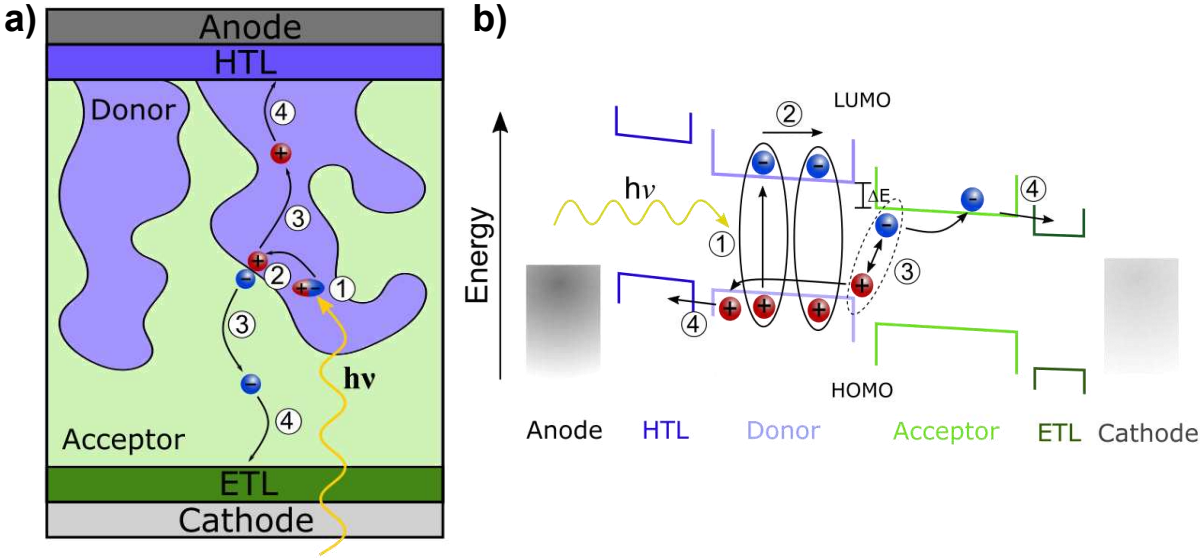

Figure 3. Graphical illustrations of the working principle of an organic solar cell, whereby a) represents the inverted device structure and b) the band diagram of a BHJ OSC. 1) Absorption of light with energy hv leads to the excitation of an electron from the HOMO to the LUMO in the donor material. 2) These created exciton diffuses towards the D/A interface, where the 3) exciton splits into free charge carriers. 4) The free charge carriers, including the electron and the hole diffuse towards the electrodes, where they are collected. Adapted from [33,38].

a hole from the HOMO to the HOMO of the donor material. This charge generation and transfer process can, although, only occur if the exciton generation takes place within the exciton diffusion length, which corresponds to approx. 10 nm [39]. In this respect, the D/A interpenetrating nanostructure within the photoactive film needs to be optimized to realize a large interfacial area between both material types as well as high-level phase segregation, which should ensure the successful generation of free charge carriers [14,20,22,35,39]. As a last step, the generated free charge carriers are transported through the respective material domains due to diffusion induced by an concentration gradient as well as due to the support of an internal electric field [36]. More specifically, electrons are transported through the acceptor material phase to the cathode, whereby holes are transferred within the donor material to the anode [36].

As previously described in section 1.1.1, a variety of different acceptor and donor materials have been developed in the last years to tune, e.g., the optical characteristics as well as the morphology of the photoactive film of an OSC [40]. In the next section, a novel, highly efficient donor-acceptor system will be discussed, which will also be employed in the device structure of this work.

1.1.3 Non-Fullerene OSCs

The urge to produce highly efficient OSCs has led research toward finding new D/A materials as well as novel device structures. Up to 2015, fullerene and their derivatives have been commonly applied as acceptors in OSCs owing to their advantageous features, such as strong electron affinity and high electron mobility [41–43]. However, these materials suffer from a low absorption in the visible-light range and restrictions in the control of energy levels, which limits the power conversion efficiency to a value of 12 % [42,44,45]. The development of novel non-fullerene acceptor materials has broken these limitations and defined new record PCEs with values of over 13 % [10,42,44,46,47]. When mixing these small molecule non-fullerene acceptors (NFAs) with polymer donor molecules, in contrast to FAs, the possible absorption range is expanded, as the NFAs and the donor molecules absorb in the near-infrared and the visible region of the light spectrum, respectively [46]. The acceptor-donor-acceptor (A-D-A) NFA type is the most common kind of NFA that has been in the research focus for years [41,42]. This structure is built up from an electron-donating fused-ring central core corresponding to the D unit, which is enclosed by two electron-withdrawing end groups, the so-called A units [41,42]. Recently, a novel NFA material, Y6, was tested in combination with a fluorinated D/A copolymer derivative PM6 (also called PBDB-TF), which led to an astonishing device performance showing a PCE of 15.7 % [48], a short circuit current (J_{SC}) of more than 25 mA cm^{-2} as well as an open circuit voltage (V_{OC}) of over 0.8 V [41,47]. Characteristically, for this Y6

acceptor is its internal structure, A-DA'D-A, which incorporates a benzothiadiazole unit as an electron-deficient core (A'), as seen in **Figure 4.** Attached to this central unit are N-alkyl pyrrole units (D) which induce an increase in the energy level of the HOMO to ca. -5.65 eV [10]. This implies a smaller band gap, and it prevents the presence of uncontrolled agglomeration mechanisms [49]. Apart from this, the alkyl chains attached to the D units sterically influence the π-stacking behavior [49]. As a result of the excellent device performance, further Y6 derivative acceptors, the so-called Y6-series, have been developed to improve the solubility and crystallization behavior in various solvents [41]. Regardless of the ongoing research for alternative polymer donor materials, PM6 has proven to be one of the most efficient polymer materials in combination with various NFAs [41]. In general, PM6 corresponds to the D-π-A copolymers group as it is composed of benzothiophene, thiophene, and benzodithiophene-4,8-dione units. Thereby, benzothiophene acts as an electron donor that provides two connection sites for fluorine atoms per molecule unit [40,41]. These halogen atoms induce a decrease in the energy level of the HOMO to a value of approx. -5.56 eV [10], resulting in an enlarged transport gap, which thus improves the device performance [40]. Due to the presence of these atoms, a dipole moment develops, which enhances the aggregation and molecular stacking behavior, leading to higher crystallinity and increased charge carrier mobility [40].

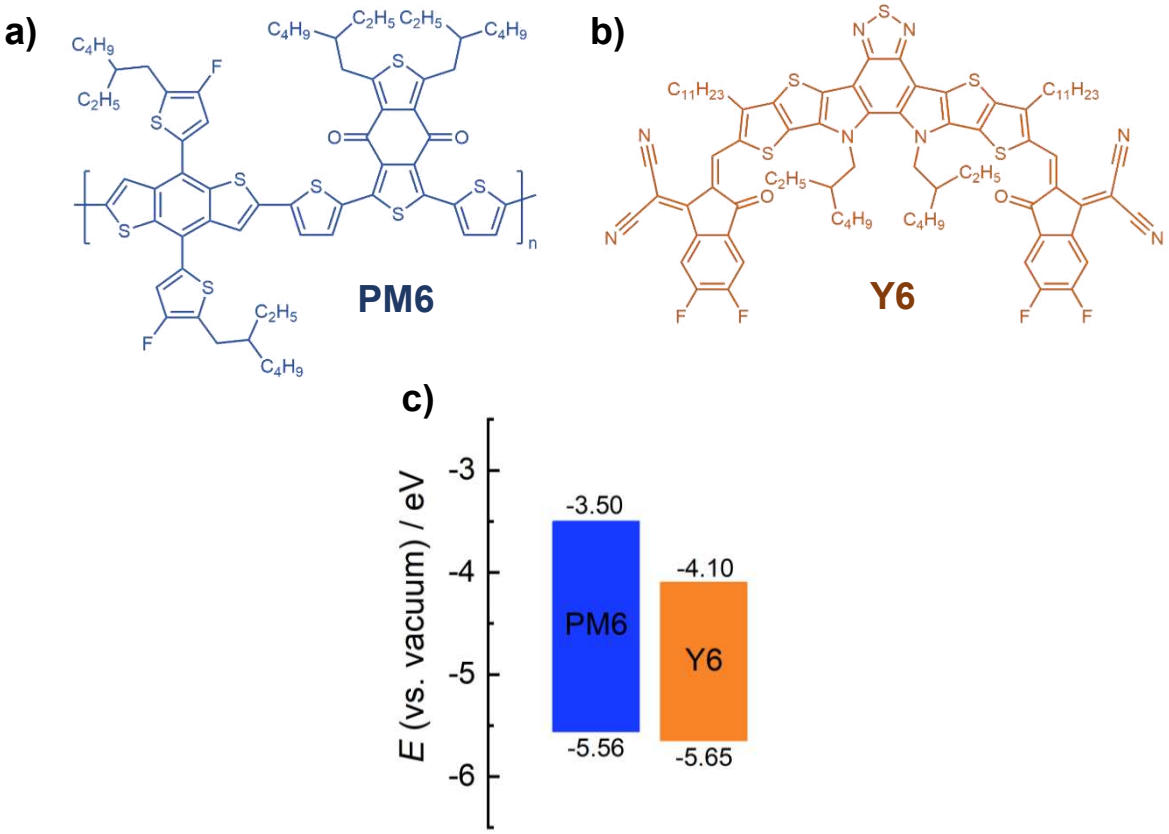

Figure 4. Molecular structure of **a)** PM6 and **b)** Y6; **c)** energy level diagram of PM6 and Y6 adapted from Guo *et al.* [41].

1.2 Optimization for an Industrial-Scale Oriented OSC Fabrication

As previously described, the PM6:Y6 D/A system shows incredible performance on a laboratory scale. To make this highly efficient system also commercially available, the manufacturing process still needs to be adapted [50]. At the moment, halogenated solvents such as chloroform or chlorobenzene are standard solvents used for PM6:Y6 blends owing to their high solubility, which is crucial to obtain a high degree of crystallinity and a good film morphology [51]. Due to the high toxicity of chlorinated solvents, alternatives have to be found that do not pose a risk to the environment and human life so that they can be employed in industrial applications [50,51]. In this respect, non-halogenated solvents like toluene, o-xylene, and 1,2,4 – trimethylbenzene (TMB) have been tested for PM6:Y6 systems, which showed promising results with a PCE of over 15 % [52]. However, to achieve such results, the processing conditions, like the processing temperature as well as the coating technique, have to be accurately optimized for the given D/A system since the solubility of these materials is significantly lower in non-halogenated solvents [50]. In addition, to further optimize the morphological structure of the photoactive layer, techniques like thermal annealing [41,53–55], solvent vapor annealing [50], or heated spin-coating [56] can be employed in the fabrication process. When considering thermal annealing, the substrate coated with photoactive material is heated to temperatures in the region of the material's glass transition points. Thereby, recrystallization of the film is induced, resulting in higher crystallinity and an improved film morphology [57]. These mentioned methods, although, show an increased sensitivity towards minor variations in process conditions as well as suffer from inconsistent performance, which is inappropriate for industrial applications [50]. Another possibility to optimize the D/A blend nanostructure for non-halogenated solvent-based films is to add small amounts of materials, including solid and high-boiling solvent additives. These solvent additives strongly influence the drying behavior of the wet film [53]. In more detail, during the drying period of the coated film, the primary solvent (e.g., *o*-xylene) will evaporate, which increases the local concentration of the solvent additive due to its lower volatility [53]. This increases the solubility difference within the D/A blend. When the high-boiling solvent additive is evaporated, the D or A material that shows a lower solubility towards the additive is more concentrated at the bottom of the film [53]. On the other hand, the second material accompanies the solvent until vaporization and accumulates at the top part of the film [53,58,59]. Despite the beneficial influence of the solvent additives on the device performance, it was previously reported in literature that these additives induced a substantial reduction in photostability [39,57]. To avoid such effects, solid additives can be used, which can be classified as volatile or non-volatile. As the name implies, volatile solid additives can be evaporated out of the blend nanostructure by applying higher

temperatures (thermal annealing), whereas non-volatile solid additives remain in the film. Both additive types influence the orientation of the D/A blend mixture as well as the morphology without significantly changing the photostability of the devices [57].

Another important factor for optimizing the fabrication process using non-halogenated solvents is finding a suitable coating process. Concerning industrial roll-to-roll applications, blade-coating is favored since the scale-up is simpler compared to other coating methods, e.g., spin-coating [60]. Besides, the coating procedure also influences the film morphology since the application of the ink solutions, as well as the drying behavior, significantly affect the formation of the nanostructure in the D/A blend [61].

All in all, the goal for industrial-oriented PM6:Y6 device manufacturing is to find the sweet spot of the trade-off between a high device performance and a sustainable fabrication process without using halogenated solvents.

1.3 Indoor Light Harvesting

Besides the well-known application of photovoltaics for harvesting solar energy, in recent years, also indoor ambient light harvesting has gained interest among the scientific community [62]. By using indoor light, electronic devices that only need a low-energy supply, such as wireless sensors and radio-frequency identification tags [63,64], could be operated. This type of electronic device can be related to the term “Internet of Things” (IoT), which corresponds to an extensive network that comprises more than 200 billion electronic devices up to now [62,65,66]. Batteries are commonly used as power supply, whereby their use implies the regular exchange of old batteries, which might be not only inappropriate for long-term autonomic applications but also economically not feasible and bear a risk of contaminating nature due to improper disposal [62]. In this sense, efficient photovoltaic devices could be a promising candidate as the powering source for IoT systems [62].

It is important to note that concerning outdoor PV applications, the operational requirements change for indoor light-harvesting devices. Typical indoor light sources like light-emitting diodes (LEDs), halogen lamps or fluorescent lamps emit light in the wavelength range of 300-800 nm [64]. To reach a high PCE, the spectral absorption range of a photovoltaic device must be optimized for this wavelength range. By applying OSCs for indoor light harvesting, the spectral properties could be tuned by molecularly modifying acceptor and donor materials. This provides both an increased J_{SC} but also a high V_{OC} [64]. It has been lately reported that organic photovoltaic devices showed astonishing PCE values of over 30 % under fluorescent lighting and LEDs, which even exceeds the PCE value of standard single-crystal silicon (Si) solar cells [9]. These highly efficient OPV systems lead to the production of more than 30 μW cm^{-2}

under indoor light illumination (500 lux), which corresponds to the power needed to operate small electronic devices related to the IoT [65]. Despite that, the change to indoor light is reported to increase the operational stability of OSCs due to the lack of UV light as well as the lowered illumination light intensity [67]. Additionally, the OSC device performance is reported to be less affected by changes in the angle of the incoming light, which was observed for Si solar cells [67].

A second important aspect concerning indoor device operation is the absence of harsh weather conditions, such as strong variations in temperature as well as any form of precipitation [62]. Consequently, the operational stability of the devices is promoted [62]. This increases the potential of OPV systems to be applied for applications in the field of IoT, although much work still has to be invested in this research topic.

In this work, the central goal is to find a fabrication process that yields not only highly efficient OSCs using PM6 and Y6 as photoactive materials but also fulfills requirements for a potential scale-up (e.g., for roll-to-roll processing), including the use of non-halogenated solvents as well as ambient conditions. Secondly, performing light-soaking stability tests with the best-performing devices under operation in indoor conditions should allow to evaluate their potential for indoor applications.

2 Experimental

2.1 Materials

The materials used in this work, as well as the corresponding abbreviation, purity, and supplier, are listed in **Table 1**.

Table 1. List of chemicals used in this study.

Photoactive material	**Abbreviation**	**Purity**	**Supplier**
PBDB-T-2F[1)]	PM6	-	1-material
BTP-4F[1)]	Y6	-	1-material
Solvent	**Abbreviation**	**Purity**	**Supplier**
Toluene	-	ACS, Reag. Ph. Eur.	VWR
o-Xylene	-	Anhydrous, 97 %	Sigma-Aldrich
Chloroform	$CHCl_3$	99 %	VWR
Ethanolamine	-	≥ 99.5 %	Sigma-Aldrich
Additive	**Abbreviation**	**Purity**	**Supplier**
1-Chloronaphthalene	CN	grade tech., ≥ 90 %	Sigma-Aldrich
1,2-Dimethylnaphthalene	DMN	98 %	Thermo Fischer Scientific
PTQ10[1)]	-	-	1-material
Electrode material	**Abbreviation**	**Purity**	**Supplier**
Silver shot	Ag	99.9999 %	Sigma-Aldrich
ETL/HTL material	**Abbreviation**	**Purity**	**Supplier**
Zinc acetate dihydrate	-	≥ 99.5 %	Fluka
Molybdenum Oxide	MoO_x	99.95 %	Kurt J. Lesker
Cleaning step	**Abbreviation**	**Purity**	**Supplier**
Toluene	-	ACS, Reag. Ph. Eur.	VWR
Acetone	-	technical	VWR
2-Propanol	*i*-Prop	ACS, Reag. Ph.Eur.	VWR

[1)]See List of Abbreviations in Appendix 4A.1 for the full chemical name.

2.2 Optimized Standard Procedure for the Fabrication of OSCs

In this work, all non-fullerene organic solar cells were prepared in the inverted device geometry of ITO/ZnO/BHJ/MoO_x/Ag. Devices that were used for the experiments in sections 2.3.1- 2.3.8, 1.27 cm × 1.27 cm substrate were cut from an ITO-coated glass sheet with a glass cutting apparatus. Two-thirds of the substrate area was covered with a polyvinyl chloride (PVC) tape and subsequently etched by immersion into concentrated hydrochloric acid (37 % (w/w) in H_2O) for 20 minutes. Following this, the substrates were rinsed with deionized water. After removing the tape, the substrates were wiped using a microfiber cloth wetted with toluene to remove traces of the remaining tape glue. Subsequently, the substrates were successively cleaned in an ultrasonic bath starting with a 2 % (v/v) aqueous solution of Hellmanex III, deionized water, acetone, and isopropanol at 50 °C for 15 minutes each. The samples were then blow-dried with nitrogen. For the devices used in sections 2.3.9-2.4, 26 mm × 26 mm × 1.1 mm pre-patterned ITO glass substrates (15 Ω sq^{-1}, Xin Yan Technology Limited) were used. The substrates were wiped with toluene-soaked microfibre cloths and subsequently treated with the same cleaning procedure as described previously, excluding the etching step. Before further usage, all cleaned substrates were oxygen plasma treated at 100 W for 10 min in a Plasma Etch PE-25 plasma cleaner.

2.2.1 ETL

For the electron transport layer (ETL), a ZnO sol-gel solution was prepared by dissolving 0.5 g (2.3 mmol) zinc acetate dihydrate as well as 0.14 g (2.3 mmol) ethanolamine in 5 mL 2-methyoxyethanol. This ZnO sol-gel solution was then continuously stirred at room temperature overnight and was then filtered using a 0.45 µm PTFE filter. Finally, a clear, slightly yellowish solution was obtained, which is usable for up to one month upon constant stirring and proper sealing with a Parafilm foil. The ZnO solution was then deposited via spin-coating at 4000 rpm for 20 s, obtaining a layer of approx. 30 nm. The ZnO layer was then annealed at 150 °C for 15 min. Both the spin-coating process and the thermal annealing were conducted under ambient conditions. This ETL deposition procedure was not changed during the whole work and was used for every experiment and device fabrication.

2.2.2 Photoactive Layer

For the active layer, a PM6:Y6 solution in a total concentration of 16 mg mL^{-1} and in a 1:1.2 (w/w) ratio was made in *o*-xylene, whereby the solutions were stirred at 80 °C overnight. Moreover, 0.5 % (v/v) 1-chloronaphthalene (CN) was added to the solution if not stated otherwise. The ink solution was then deposited via spin-coating or doctor blade-coating.

For the first coating method, the *o*-xylene ink solutions were deposited *via* spin-coating using 500 rpm for 2 s, followed by 1500 rpm for 30 s under ambient conditions. Important to note is that the solution was constantly stirred at 80 °C during the deposition process. Moreover, the solution was transferred onto the substrate within 15 s, whereby the solution was left to cool on the glass substrate approx. 45 s before starting the spin-coating program. With this deposition method, a layer thickness of approx. 70 nm was obtained. Next, the films were thermally annealed at 130 °C for 5 min under ambient conditions. Using a cotton swab wetted with toluene, the active layer material was carefully removed from the area where the hole transport layer, as well as the top and bottom electrodes, are going to be deposited (see **Figure 5**).

In addition, as a second deposition method, doctor blade-coating (Erichsen Coatmaster 409 MC) was used for the active layer deposition of the ink solutions under ambient conditions. In this respect, the *o*-xylene solutions were constantly stirred at 80 °C, and the thin films were formed at a blade velocity of 15 mm s^{-1} and a hot plate temperature of 80 °C. Before the deposition process, the glass/ITO/ZnO substrates were put onto the hot plate for approx. 1 min before the coating process, allowing it to heat up to 80 °C. The slit of the blade was set to 500 µm for all experiments. Consequently, a layer thickness of approx. 80 nm was obtained, whereby slight variations in the ink concentration or volume used for the coating process might

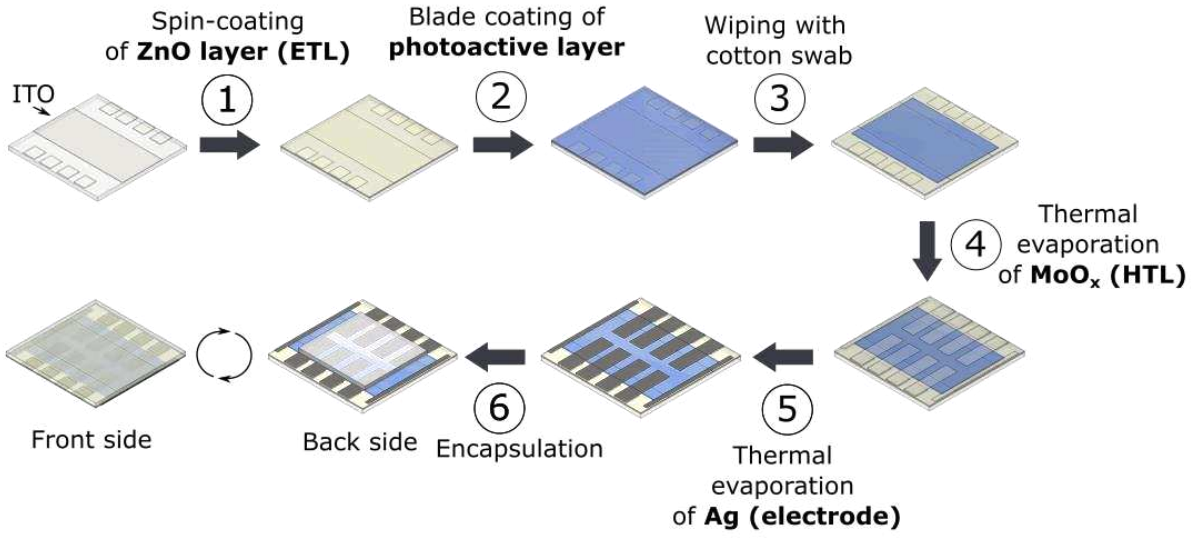

Figure 5. An exemplary illustration of the main processing steps of the OSCs fabrication (without annealing steps), whereby in this case, 26 mm × 26 mm substrates (à eight pixels) are used for the device fabrication. 1) The patterned glass/ITO substrate is spin-coated with a layer of ZnO. 2) The photoactive material is deposited onto the ZnO layer. 3) The photoactive material is wiped off at specific areas using a toluene-soaked cotton swab. On top, 4) a layer of MoO_x and subsequently 5) a layer of silver (Ag) is deposited *via* thermal evaporation. 6) The devices are encapsulated (only applied for 26 mm × 26 mm substrates).

slightly change the final thickness. In analogy to the spin-coating process, the films were thermally annealed at 130 °C for 5 min in air.

2.2.3 HTL and Top Electrodes

To complete the device structure, the substrates were fixed in the respective shadow mask (see **Figure 6**), and a 10 nm HTL-layer of molybdenum oxide (MoO_x) as well as a 100 nm top electrode layer of Ag was thermally evaporated at a pressure of 1-8 × 10^{-6} mbar using the UNIVEX 350 (Leybold). To determine the area of the solar cells, a caliper was used.

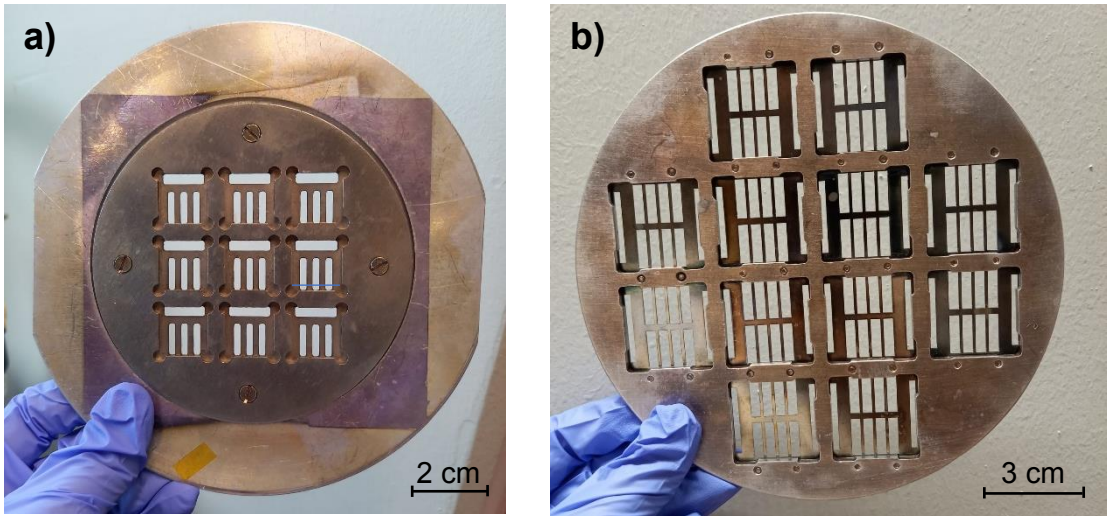

Figure 6. Picture of the shadow mask used for the **a)** 1.27 cm × 1.27 cm substrates (small) and **b)** for the 2.6 cm × 2.6 cm (large) substrates.

2.2.4 Encapsulation

As the last step, the devices (prepared on 2.6 cm × 2.6 cm × 1.1 mm pre-patterned ITO glass substrates) were encapsulated under inert conditions using either the EMCAST 1500 LI Clear (Electronic Materials, EMIUV) or the DELO® KATIOBOND® LP655 as an epoxy resin as well as 1.7 cm × 1.7 cm cleaned glass slides under inert conditions. Both epoxy sealants were cured under UV light three times for 1 minute each.

2.3 Optimization of the Device Fabrication

2.3.1 Thicknesses of the Spin-Coated Absorber Layers

For the tests of different spin-coated absorber layer thicknesses, shown in section 3.1.1, solutions of 16 mg mL^{-1} PM6:Y6 (1:1.2, w/w) in *o*-xylene and an 8 mg mL^{-1} PM6:Y6 (1:1.2, w/w) solution in toluene were prepared. The solutions were stirred at 80 °C overnight under ambient conditions. All solutions were cooled down to room temperature before the spin-coating process. The solutions were then coated onto glass/ITO substrates already covered with the ZnO layer following the standard procedure (see section 2.2.1). For the coating process, different spin-coating programs were used, as visible in **Table 2**, whereby the rotation speed and acceleration were varied for step 2. The solar cells were thermally annealed at 110°C for 10 minutes. Following this, the HTL and the Ag electrodes were applied according to the procedure described in section 2.2.3.

Table 2. Spin-coating parameters used for the deposition of the photoactive layers from solutions of PM6:Y6 (1:1.2 w/w) of 16 mg mL^{-1} in o-xylene and 8 mg mL^{-1} in toluene, respectively, for the tests of different film thicknesses.

Solvent	Step	*t* / s	rpm / min^{-1}	ramp / rpm s^{-1}
toluene	1	2	500	250
	2	30	500	250
			750	375
			1000	500
o-xylene	1	2	500	250
	2	30	730	365
			900	450
			1075	538
			1250	625
			1500	750

2.3.2 Comparison of Solvents

To compare the different solvent systems, a 16 mg mL^{-1} PM6:Y6 (1:1.2, w/w) solution with 0.5 % (v/v) of the additive 1-chloronaphthalene (CN) in chloroform as well as in *o*-xylene was prepared. Additionally, an 8 mg mL^{-1} PM6:Y6 (1:1.2, w/w) solution with 0.5 % (v/v) CN was made in toluene. The chloroform solutions were stirred at 40 °C and the *o*-xylene and toluene inks at 80 °C overnight. Before the spin-coating, all solutions were cooled down to room temperature. Next, the active layer was spin-coated onto glass/ITO/ZnO using the spin-coating programs shown in **Table 3**. Furthermore, the toluene and the *o*-xylene solutions were reheated to 80 °C under constant stirring for 10 minutes. Subsequently, new devices were prepared by spin-coating the hot ink solutions onto glass/ITO/ZnO substrates using the spin-coating recipes from **Table 3**. All devices were thermally annealed at 110 °C for 10 min. The

HTL and the Ag electrodes were evaporated according to standard procedure see section 2.2.3.

Table 3. Spin-coating parameters used for the deposition of the photoactive layers from solutions of PM6:Y6 (1:1.2 w/w) of 16 mg mL^{-1} in chloroform or *o*-xylene and 8 mg mL^{-1} in toluene, respectively, for the test of different solvents.

Solvent	Step	*t* / s	rpm / min^{-1}	ramp / rpm s^{-1}
chloroform	1	30	3000	1500
toluene	1	2	500	250
	2	30	750	375
o-xylene	1	2	500	250
	2	30	1500	750

2.3.3 Delay Time for Hot Spin-Coating

To investigate how variations in the period starting with the transfer of the ink from the vial onto the substrate to the activation of the spin-coating program affects the performance of the devices, two 16 mg mL^{-1} PM6:Y6 (1:1.2, w/w) solution in *o*-xylene were prepared, whereby to one solution 0.5 % (v/v) CN was added. The ink solutions were stirred at 80 °C overnight. For the deposition process, the ink was constantly stirred at 80 °C and was then transferred onto each substrate within 15 s. The spin coater program was then started with a delay of 5 to 45 s, resulting in total delay times of 20, 30, 40, 50 and 60 s. The ink solutions were deposited *via* spin-coating using 500 rpm for 2 s followed by 1500 rpm for 30 s under ambient conditions. The solar cell devices were subsequently annealed at 110 °C for 10 min. The HTL and the Ag electrodes were evaporated following the standard procedure described in section 2.2.3.

2.3.4 D/A Blend Composition Test for the Photoactive Layer

Different PM6:Y6 blend ratios were tested to find the composition giving the best device performance. For this purpose, 16 mg mL^{-1} PM6:Y6 solutions in *o*-xylene with 0.5 % (v/v) CN were prepared using the three different weight ratios: 1:1, 1:1.2, and 1:2. The solutions were then stirred at 80 °C overnight. The deposition of the ink solution was performed at 80 °C stirring temperature with a delay time of approx. 1 min and a spin-coating program of 500 rpm for 2 s, followed by 1500 rpm for 30 s under ambient conditions. The solar cell devices were subsequently annealed at 110 °C for 10 min. The following device fabrication, including the deposition of the HTL and the Ag electrodes, was performed according to the standard procedure described in section 2.2.3.

2.3.5 Optimal HTL Thickness

For further optimization of the solar cell performance, the influence of the thickness of the hole transport layer (MoO_x) on the device performance was examined. In this respect, a 16 mg mL^{-1}

PM6:Y6 (1:1.2, w/w) solution in *o*-xylene with 0.5 % (v/v) CN was prepared and stirred at 80 °C overnight. For coating the glass/ITO/ZnO substrate, the standard spin-coating procedure from section 2.2.2 was applied. Afterward, the substrates were thermally annealed at 110 °C for 10 min. Next, for the HTL, MoO_x was deposited in varied thin film thicknesses of 5, 7, 9, 10, 11 and 15 nm. Following this, the substrates were coated with 100 nm Ag.

2.3.6 Annealing Temperature for the Photoactive Layer

To test different annealing temperatures and annealing durations of the active layer, a standard solar cell was produced using 16 mg mL^{-1} PM6:Y6 (1:1.2, w/w) solutions in *o*-xylene with 0.5 % (v/v) CN for the spin-coating process of the active layer. In contrast to the standard device fabrication procedure, the devices were thermally annealed after the deposition of the Ag electrodes. For the evaluation of the best annealing process, the devices were characterized before the annealing and after 5 and 10 minutes of annealing, respectively. The temperatures tested for the annealing of the complete devices were 95, 100, 105, 110, 115, 120, 130 and 150 °C.

Additionally, a second annealing experiment was conducted. For the device fabrication, the standard procedure (see section 2.2) was performed, with the only variation being the thermal annealing step for the absorber material. In this case, the annealing was conducted after the coating process of the absorber material, and substrates were annealed for 5 minutes at either 100, 110, 120, 130 or 140 °C.

2.3.7 PTQ10 as an Additive for the Photoactive Layer

Besides CN, PTQ10 was also tested as a possible additive for increasing the solar cell performance and morphology of the absorber layer. In this respect, four 16 mg mL^{-1} PM6:Y6 (1:1.2, w/w) solutions in *o*-xylene with 0.5 % (v/v) CN were prepared, whereby PTQ10 was mixed to the solutions in 0, 0.5, 1 and 2 mg mL^{-1} concentrations with respect to the solvent volume. These ink solutions were then stirred at 80 °C overnight. The following device fabrication was conducted according to the optimized standard spin-coating procedure see section 2.2.2

2.3.8 Influence of Inert Conditions on the Spin-Coating Process

For the comparison of ambient and inert coating conditions of the active layer, standard devices were prepared under ambient conditions following the procedure, as described in section 2.2. Moreover, with the same standard ink solution in *o*-xylene, the spin-coating process and the following annealing step were conducted under inert conditions in a glovebox. Apart from the inert conditions, the spin-coating and the annealing process did not differ in any other point from the standard device fabrication process (see section 2.2).

2.3.9 Optimal Thickness and Coating Temperature for the Blade-Coating Process

For finding the best-performing thickness of the absorber layer, different blade-coating velocities were examined, ranging from 10 mm s^{-1} to 20 mm s^{-1} at a temperature of ca. 56 °C. For the experiment, the standard ink solution was prepared, and device fabrication, including ETL, annealing of the active layer, HTL and the Ag electrodes, was performed according to the procedure stated in section 2.2. To determine the layer thickness (according to section 2.5.1) resulting from the different blade-coating velocities, cleaned glass substrates were coated with the same procedure used for the device fabrication in this experiment.

For the blade-coating process, additionally, the influence of the temperature of the substrate on the blade-coater, as well as the effect of the blade velocity during the coating process on the device performance, were investigated. Therefore, substrates were coated with a newly prepared standard ink solution at a blade-coating velocity of 12 mm s^{-1} at temperatures of approx. 56, 70, 80 and 90 °C. To test the different blade velocities, the velocities were varied between 12.5 mm s^{-1} and 25 mm s^{-1} while the plate was heated to 80 °C. Subsequently, the devices were prepared following the consecutive steps in the process of section 3.1. In difference to the first thickness test for the blade-coating, the film thickness was determined via the optical density of the thin films of each substrate using a UV-vis fiber spectrometer, as described in section 2.5.1

2.3.10 Comparison of Additives for Blade-Coating

For examining the influence of the additives CN and 1,2-dimethylnaphthalene (DMN) on the performance of the prepared solar cell devices, several batches of devices were produced whereby three types of ink solutions were applied for the blade-coating standard device fabrication process, as described in section 2.2. These three types include a standard ink solution (16 mg mL^{-1} PM6:Y6 (1:1.2, w/w) solution in *o*-xylene with 0.5 % (v/v) CN, a 16 mg mL^{-1} PM6:Y6 (1:1.2, w/w) solutions in *o*-xylene with 0.5 % (v/v) DMN and a blank 16 mg mL^{-1} PM6:Y6 (1:1.2, w/w) in *o*-xylene without additive.

2.4 Stability Tests

2.4.1 Storage under Inert and Ambient Conditions

To evaluate the stability of standard devices encapsulated using either the epoxy glue EMCAST or DELO®, two substrates (each eight devices) were stored in a glovebox (dark condition) and two substrates under ambient conditions, whereby for both storage locations, one EMCAST and one DELO encapsulated substrate was used. The devices were prepared according to the optimized standard procedure for blade-coating (see section 2.2). The device performance was periodically tracked by measuring the *J-V* curves.

2.4.2 Light-Soaking Stability Tests under Operation

The light soaking stability of devices was tested, which were prepared without additives and with CN additive or DMN additive added to the PM6:Y6 solution, respectively, according to the procedure stated in section 3.2.10. On each substrate, three pixels were selected for the light-soaking stability tests. The *J-V* response of one of these devices was measured with a Keithley 2400 SM when illuminated with an ordinary table lamp (Sylvania CF-S 11 W fluorescent lamp) at 1200 lux. Consequently, the maximum power point (MPP) was determined. Next, to operate the respective devices at the MPP, a suitable resistor was chosen. Since all devices showed a similar MPP, resistors in the range of 13 – 15 kΩ were used. Furthermore, the top and the back contact were coupled via cable with crocodile clips, whereby the resistor was connected in series, as shown in **Figure 7 a)** and **b)**. Secondly, on each substrate, a second cell was operated at J_{SC}. For this, the top and the back contact were directly connected via cables equipped with crocodile clips. The third selected pixel on each substrate was operated at V_{OC}. This light-soaking stability test was conducted in four different testing setups and was all performed under ambient conditions using Sylvania CF-S 11 W fluorescent lamps as illumination sources. The testing setups are shown in **Figure 7 c)**. For each test, three substrates with eight pixels were used, whereby for the device fabrication, one substrate was coated with ink solution without solvent additive, one with CN, and one with DMN. In test setups 1-3, a light intensity of 1200 lux was used, while for the fourth test setup, a light intensity of 3000 lux was applied. To calibrate the light intensity, a lux meter (EasyView 30, EXTECH instruments) was utilized. The devices measured in test setups 1 and 2 were encapsulated using the EMCAST epoxy resin, while for devices in setups 3 and 4, the DELO epoxy glue was used (see section 2.2.4). To avoid strong scratching and losing contact to the thin Ag electrode when using crocodile clips for contacting, a small amount of an indium wire was pressed onto the contact points on the Ag electrodes of all devices. A summary of the varied testing conditions is seen in **Table 4**.

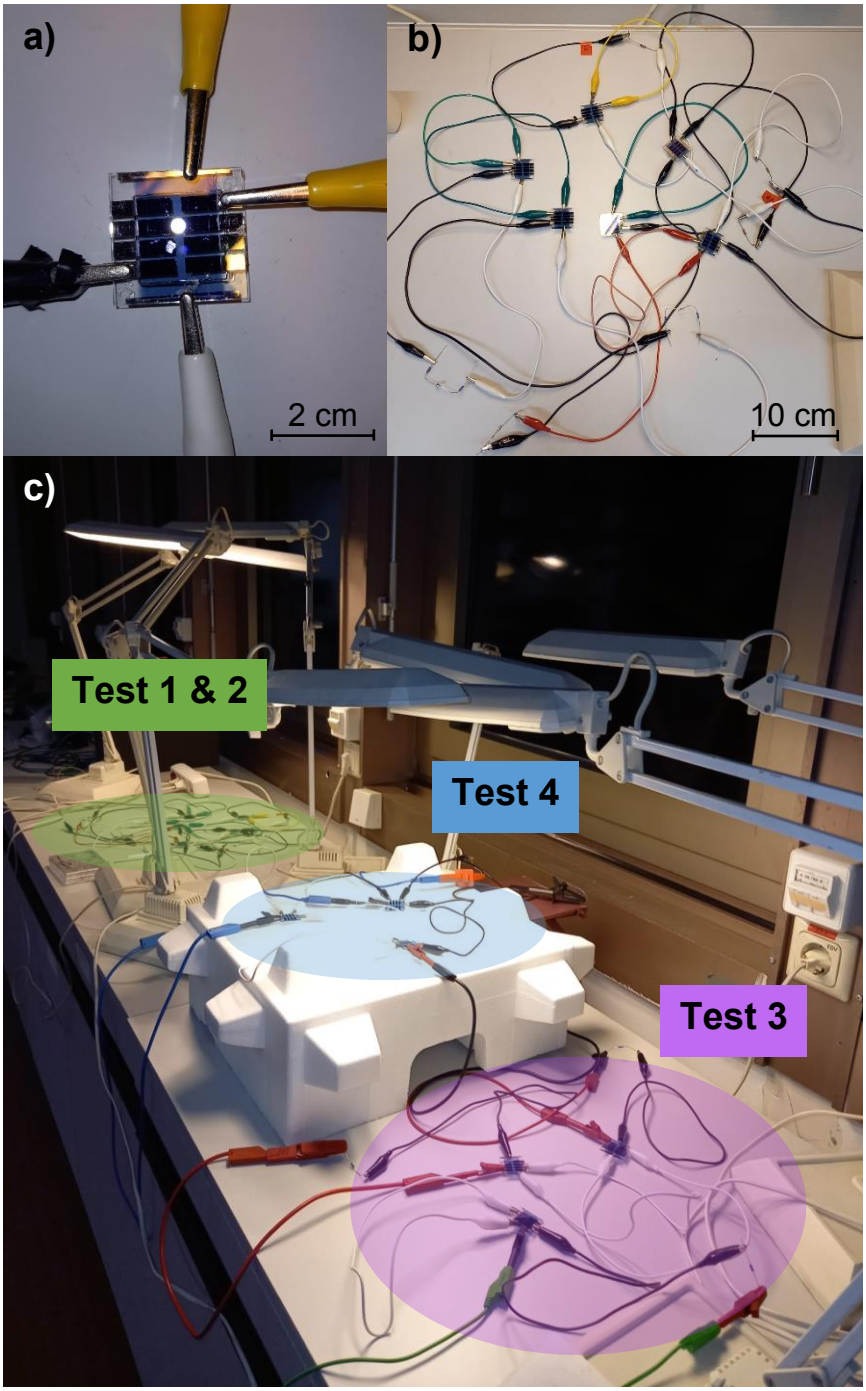

Figure 7. Picture of **a)** an exemplary substrate whose devices are connected using crocodile clips (in this case for operation at J_{SC}: yellow cables, for MPP: black and white cables), **b)** the exemplary arrangement of devices, cable and resistors (in this case test setups 1 and 2) and **c)** the overall experimental set-up for the four light-soaking stability test setups.

Table 4. Experimental conditions used in the four light-soaking stability test setups.

Test Nr.	Epoxy glue	Resistor	Light intensity / lux
1	EMCAST	13.5 kΩ	1200
2	EMCAST	15 kΩ	1200
3	DELO	13 kΩ	1200
4	DELO	13 kΩ	3000

To track the device performance, all operated devices were periodically characterized by measuring the *J-V* curves at 1 sun (see section 2.5.2). Additionally, the EQE curves of the devices from test setups 2,3 and 4 were recorded.

2.4.3 Power Output at Low-Light Intensity Illumination

The devices of test setup 2 operated at the MPP, as described in section 2.4.2, were utilized for measuring *J-V* curves under the illumination of the low-light intensity of 1000 lux using a table lamp. The light intensity was fixed using a certain position of the device with respect to the light source, and the intensity was calibrated using a lux meter. The *J-V* response measurement was conducted under ambient conditions using a Keithley 2400 SM.

2.5 Characterization Measurements

2.5.1 Film Thickness Measurement

For the measurements of film thicknesses, a Bruker Dektak XT profilometer was used. For the determination of the thickness of the active layer used in the solar cells, the absorber layer solution was directly deposited on a cleaned and plasma-treated glass substrate using the same spin-coating program used for the respective device fabrication. For all measurements, a stylus force of 2 mg was applied.

Additionally, the thin film thickness of the absorber layer was determined by the relation of film thickness to optical density. For the measurement of the absorbance spectra, a Fiber Optic spectrometer (AvaSpec-2048, Avantes) was applied, whereby a tungsten halogen lamp (AvaLight Hal, Avantes) served as a light source. For the calibration of absorbance versus film thickness, a standard ink solution was blade-coated at 80 °C with different coating velocities ranging from 10 to 25 mm s^{-1} onto cleaned and O_2 plasma-treated glass substrates. The thickness of the obtained thin film was measured using profilometry. The absorbance spectra of each thin film were recorded, whereby a glass substrate was used as a reference. The peak absorbance values were measured at wavelengths of approx. 630 nm and 830 nm, which correspond to the wavelength at maximum absorbance of PM6 and Y6, respectively [68,69]. For both wavelengths, a calibration line was prepared by relating the measured thickness to the corresponding optical density of the thin film (for linear fits, see **Figure 32** in Appendix). For the determination of the active layer thickness of a sample, the average value obtained from the values of the PM6 and the Y6 calibration lines was used.

2.5.2 Current Density-Voltage Measurements

For conducting current density voltage (*J-V*) measurements of the solar cell devices, a LOT-QD solar simulator (LS0821) as well as a Keithley 2401 SMU was used. The devices were irradiated using a xenon arc-discharge lamp, which provides a continuous AM1.5 G spectrum. The light intensity was calibrated with a reference silicon diode (Si-01 TC, Mencke Tegtmeyer). For the measurement, only forward bias was used. The evaluation of the measured data was performed using a custom-made software. For the statistical assessment of the device performance parameters within each experimental series, only devices were included that exhibited a FF of up to 15 % points below the FF corresponding to the device with the maximum PCE value measured within each experimental data set.

2.5.3 External Quantum Efficiency

For the external quantum efficiency (EQE) measurement, a custom-made set-up was used. A xenon lamp (Oriel instruments) served as a light source, whereby the light was guided to a mechanical chopper wheel operated at a frequency of 173 Hz. The light is then coupled to a

monochromator (Oriel Instruments) and subsequently focussed with a lens onto the solar cell substrate. The solar cell was connected to a Jaissle potentiostat 1002 T-NC *via* two electrodes. For the conversion from current to voltage, a gain of 10^4 V A^{-1} was selected. Furthermore, the use of a lock-in amplifier (Model SR830, Stanford Research systems) allows to perform EQE measurements with high sensitivity. The current output of the measured solar cell was measured over a spectral range of 350 to 1000 nm, whereby the obtained spectra were corrected for the xenon lamp spectrum using a silicon photodiode (S2281, Hamamatsu). During the measurement of the devices, the spectral photocurrent ($I_{SC}(\lambda)$) is detected, which can be used to determine the EQE at a specific wavelength given by

$$I_{SC}(\lambda) = q \cdot \mathrm{EQE}(\lambda) \cdot \Phi_{\text{light source}}(\lambda) \tag{1}$$

where q is the elementary charge, and $\Phi_{\text{light source}}$ corresponds to the photon flux at a respective wavelength from the light source. When using the measured photocurrent ($I_{SC,ref.}(\lambda)$) of the reference Si photodiode, whose $\mathrm{EQE}_{ref.}(\lambda)$ is already determined, one can rearrange Eqution 2 for $\Phi_{\text{light source}}$ and insert it into Equation 1. From this, the EQE per wavelength can be calculated following Equation 3.

$$I_{SC,\mathrm{ref.}}(\lambda) = q \cdot \mathrm{EQE}_{\mathrm{ref.}}(\lambda) \cdot \Phi_{\text{light source}}(\lambda) \tag{2}$$

$$\mathrm{EQE}(\lambda) = I_{SC}(\lambda)\, \frac{\mathrm{EQE}_{\mathrm{ref.}}(\lambda)}{I_{SC,\mathrm{ref.}}(\lambda)} \tag{3}$$

Following this, $J_{SC,calc.}$ can be derived from the EQE(λ), as given by Equation 4 [70]

$$J_{\mathrm{SC,\,calc.}} = \frac{q}{h \cdot c} \int \mathrm{EQE}(\lambda) \cdot S_{\mathrm{AM1.5G}}(\lambda)\, d\lambda \tag{4}$$

with h corresponding to the Plank constant, c to the speed of light (in vacuum) and $S_{AM1.5G}$ to the solar spectral irradiance at AM1.5G conditions. It has to be mentioned that the value of calculated $J_{SC,calc}$ might differentiate up to 5 - 10 % from the value of J_{SC}, which is extracted from the corresponding *J-V* curve. This observation might originate from approximating the photoactive area. Secondly, for the EQE calculation, a correction with a reference spectrum was made, which should account for the strong intensity peak of the emission spectrum of the xenon lamp in the range of 800 - 950 nm [71]. Since this correction was not performed for the recorded *J-V* curves, the J_{SC} was always slightly overestimated with respect to the $J_{SC,calc.}$ Furthermore, as already mentioned, the light intensity of the xenon lamp used for the solar simulator frequently showed strong fluctuations in light intensity, which also led to variations in the measured J_{SC}.

2.5.4 Optical Microscope

The microscope pictures of the thin films were taken using a Nikon Eclipse LV100 ND microscope in bright field mode.

3 Results and Discussion

3.1 Optimization of Device Fabrication Using Spin-Coating

3.1.1 Thickness for Spin-Coated Devices

In the course of the study, the focus was to process solar cells in conditions that facilitate the application in large-scale production, including ambient processing conditions, as well as the usage of non-halogenated solvents. In this respect, the two non-halogenated solvents, toluene and *o*-xylene, were tested. Chloroform was taken as a reference system due to its well-established use as a solvent yielding highly efficient solar cells [72]. When testing the solubility of the donor and acceptor material in chloroform, toluene, and *o*-xylene, it could be seen that chloroform fully dissolved the materials when stirred overnight at 40 °C. In contrast, the material was not fully dissolved in toluene and *o*-xylene under the same conditions. Consequently, the non-halogenated were stirred overnight at 80 °C. Under these conditions, *o*-xylene solutions showed complete dissolution, unlike toluene, which solution still showed solid particles. Also, at higher temperatures, the particles could not be dissolved in toluene at a concentration of 16 mg mL^{-1}. The dissolution in toluene was achieved when using a solution with a concentration of 8 mg mL^{-1}.

To test different thicknesses of the absorber layer to obtain the best photovoltaic performance for both solvents, the second step of the spin coating program was varied, as described in section 2.3.1. With toluene as solvent, it could be seen that when decreasing the rotation speed to 500 rpm, the homogeneity of the thin film surface was lowered, and agglomerates were formed on the substrate. When increasing the rotation speed to improve the uniformity of the film, a film thickness of approx. 70 nm was produced, as visible in **Table 5**. Moreover, it could be seen that the photovoltaic performance was independent of the layer thickness. Important to mention is that for the statistical evaluation of the performance, only devices with a FF above 38 % were used, as described in section 2.5.2. According to literature, typically applied absorber layer thicknesses range from 60 – 110 nm [13,73–75]. In this thickness range, constructive interferences due to the reflection of light at the electrode promote a high degree of light absorption [73,76]. Additionally, devices with a photoactive layer thickness above 110 nm might be negatively affected by a restriction in charge carrier mobility as well as morphology, which leads to a decreased FF [73]. Conforming to this trend, the FF of the fabricated PM6:Y6 solar cells slightly decreases with increasing film thickness, as visible in **Table 5**. As a trade-off between morphology and absorber layer thickness, a spin-coating program of 500 rpm for 2 s followed by 750 rpm for 30 s was chosen as the standard recipe for toluene solutions.

Table 5. Photovoltaic performance of the solar cells prepared from an 8 mg mL^{-1} PM6:Y6 (1:1.2, w/w) solutions in toluene, whereby different thicknesses of the absorber layer are shown that are obtained using different rotation speeds in the spin-coating process (see section 2.3.1). n is the number of devices measured for each set of processing parameters.

rpm / min^{-1}	*approx. d / nm*	V_{OC} / V	J_{SC} / mA cm^{-2}	FF / %	PCE / %	n
500	120	0.74 (0.75 ± 0.01)	7.6 (7.1 ± 0.6)	51 (50 ± 1)	2.9 (2.7 ± 0.2)	6
750	100	0.75 (0.74 ± 0.00)	7.91 (7.6 ± 0.2)	52 (52 ± 1)	3.2 (3.0 ± 0.1)	6
1000	70	0.74 (0.73 ± 0.02)	8.66 (7.4 ± 1.1)	53 (53 ± 3)	3.5 (2.9 ± 0.4)	6

In contrast to toluene, PM6 and Y6 was fully dissolved in *o*-xylene at a concentration of 16 mg mL^{-1} when stirred overnight at 80 °C. Similarly to toluene, different spin-coating programs were tested for the *o*-xylene solutions to optimize the spin-coating process for obtaining the best device performance. For the statistical evaluation of this experiment, only devices with a FF higher than 41 % were included (see section 2.5.2.). As visible in **Table 6**, the layer thickness for the *o*-xylene test showed that for all prepared devices, a similar performance was obtained independent of the film thickness in the scope of 60 – 90 nm. However, the lowest film thickness (60 nm) was found to produce a slightly higher average FF as well as a higher maximum power conversion efficiency (PCE). Consequently, 500 rpm for 2 s followed by 1500 rpm for 30 s was used as the standard spin-coating program for *o*-xylene as solvent.

Table 6. Photovoltaic performance of the devices prepared using a 16 mg mL^{-1} PM6:Y6 (1:1.2, w/w) solution in *o*-xylene using different rotation velocities during the spin-coating process (see section 2.3.1). n is the number of devices measured for each set of processing parameters.

rpm / min^{-1}	*approx. d / nm*	V_{OC} / V	J_{SC} / mA cm^{-2}	FF / %	PCE / %	n
730	90	0.74 (0.74 ± 0.00)	10.2 (9.1 ± 1.0)	53 (53 ± 0)	4.0 (3.6 ± 0.4)	6
900	80	0.74 (0.74 ± 0.01)	9.5 (9.6 ± 0.6)	56 (54 ± 3)	3.9 (3.8 ± 0.1)	4
1075	70	0.74 (0.74 ± 0.00)	10.1 (9.9 ± 0.3)	54 (54 ± 1)	4.1 (3.9 ± 0.2)	5
1250	65	0.74 (0.73 ± 0.00)	9.6 (9.5 ± 0.1)	54 (55 ± 1)	3.8 (3.8 ± 0.0)	3
1500	60	0.73 (0.73 ± 0.01)	10.5 (9.6 ± 0.7)	55 (56 ± 1)	4.2 (3.9 ± 0.2)	6

3.1.2 Solvent Selection for Photoactive Material

To optimize the device performance for solution-processed OSCs, the selection of a proper solvent is crucial. During solvent evaporation, the D/A components are arranged in a solvent-specific interpenetrating network [30,53,77]. The characteristics of the obtained film morphology strongly affect the device performance [53]. In this respect, the photovoltaic performance of devices prepared from toluene and *o*-xylene ink solutions with the optimized spin-coating parameters (see section 2.3.2 for experimental details) was compared to devices produced based on a chloroform ink solution using the spin-coating process reported by Van der Pol *et al.* [72]. To all ink solutions, 1-chloronaphthalene (CN) was mixed as an additive, and the solutions were deposited at room temperature (see section 2.3.2). When observing the produced thin films, it was found that for both the toluene and the *o*-xylene solutions, needle-shaped polymer agglomerates formed, as visible in **Figure 8**. This effect was more pronounced for toluene as a solvent. The crystal formation might indicate the precipitation of recrystallized D/A material owing to the lowered solubility of the photoactive material in the solutions at room temperature [52,78,79]. To reduce this effect, the ink solutions were reheated and used for spin-

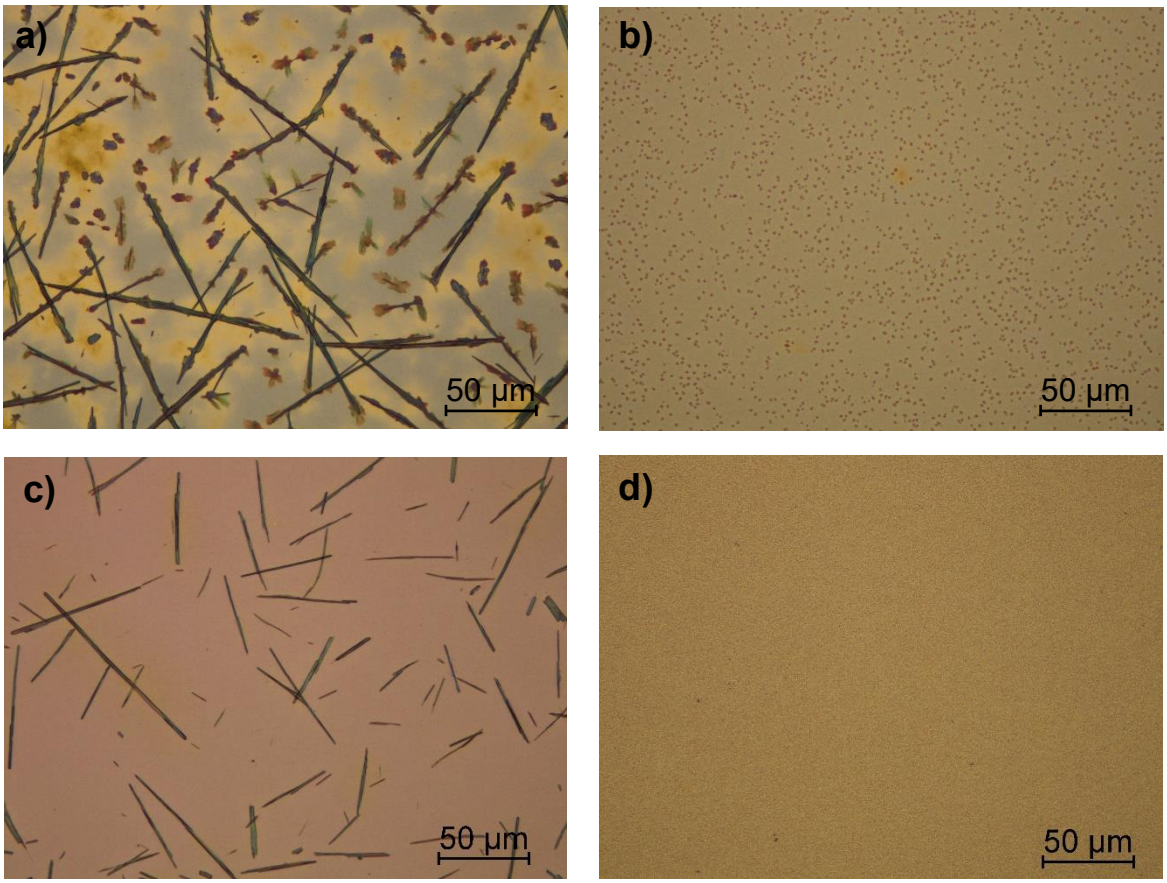

Figure 8. Microscope pictures (magnification: 40x) of thin films prepared from PM6:Y6 (1:1.2, w/w) + 0.5 % (v/v) CN in toluene solutions stirred **a)** at room temperature and **b)** at 80 °C as well as thin films processed from PM6:Y6 (1:1.2, w/w) + 0.5 % (v/v) CN in *o*-xylene solutions **c)** at room temperature and **d)** at 80 °C.

coating at a constant stirring temperature of 80 °C. In **Figure 8 b)** and **d),** one can directly compare the microscope pictures of toluene and *o-xylene*-based thin films deposited at 80 °C. In comparison to the microscope picture of the films processed at room temperature, no crystal needles have formed for both solvent types at 80 °C processing. However, the toluene-based film still shows a more inhomogeneous surface as well as a higher roughness than the *o*-xylene films based on the microscope picture. This surface structure might be attributed to increased aggregation and phase separation of the donor and acceptor material [51]. Additionally, the film thickness of both films was checked via the optical density of the films (see section 2.5.1), and no change in film thickness could be observed when using the hot solution spin-coating process.

In **Table 7**, the photovoltaic performance is listed for devices where the photoactive layer was coated from different solvents and processing temperatures ($T_{processing}$). For the statistical evaluation, only devices exhibiting a FF above 49 % were included (see section 2.5.2).

Table 7. PV performance of devices prepared using different solvents as well as different stirring temperatures directly before coating.

Solvent	$T_{processing}$ / °C	V_{OC} / V	J_{SC} / mA cm^{-2}	FF / %	PCE / %	n
chloroform	25	0.78 (0.78 ± 0.03)	22.5 (21.0 ± 1.9)	62 (61 ± 3)	11.1 (10.3 ± 0.9)	8
toluene	25	0.79 (0.79 ± 0.03)	7.1 (6.5 ± 0.4)	55 (54 ± 2)	3.2 (2.8 ± 0.3)	9
toluene	80	0.68 (0.66 ± 0.02)	14.4 (13.9 ± 1.3)	64 (58 ± 5)	6.27 (5.2 ± 0.6)	6
o-xylene	25	0.76 (0.76 ± 0.01)	16.0 (15.6 ± 1.3)	60 (58 ± 3)	7.4 (7.0 ± 0.6)	7
o-xylene	80	0.78 (0.75 ± 0.01)	18.2 (16.0 ± 1.0)	59 (58 ± 2)	8.5 (7.2 ± 0.6)	21

As presented in **Table 7** and **Figure 9**, the highest average J_{SC}, FF and PCE with the respective values of 21.0 mA cm^{-2}, 61 % and 10.3 % could be achieved when using chloroform as solvent. In literature, much higher performance parameters for the chloroform system were reported with a PCE of 15.7 %, FF of 76.1 %, V_{OC} of 0.82 V, and a J_{SC} of 25.3 mA cm $^{-2}$ [48]. Although this strong difference in device performance was observed, this data was only used as a reference for other solvent systems. Consequently, no further optimization of the chloroform system was

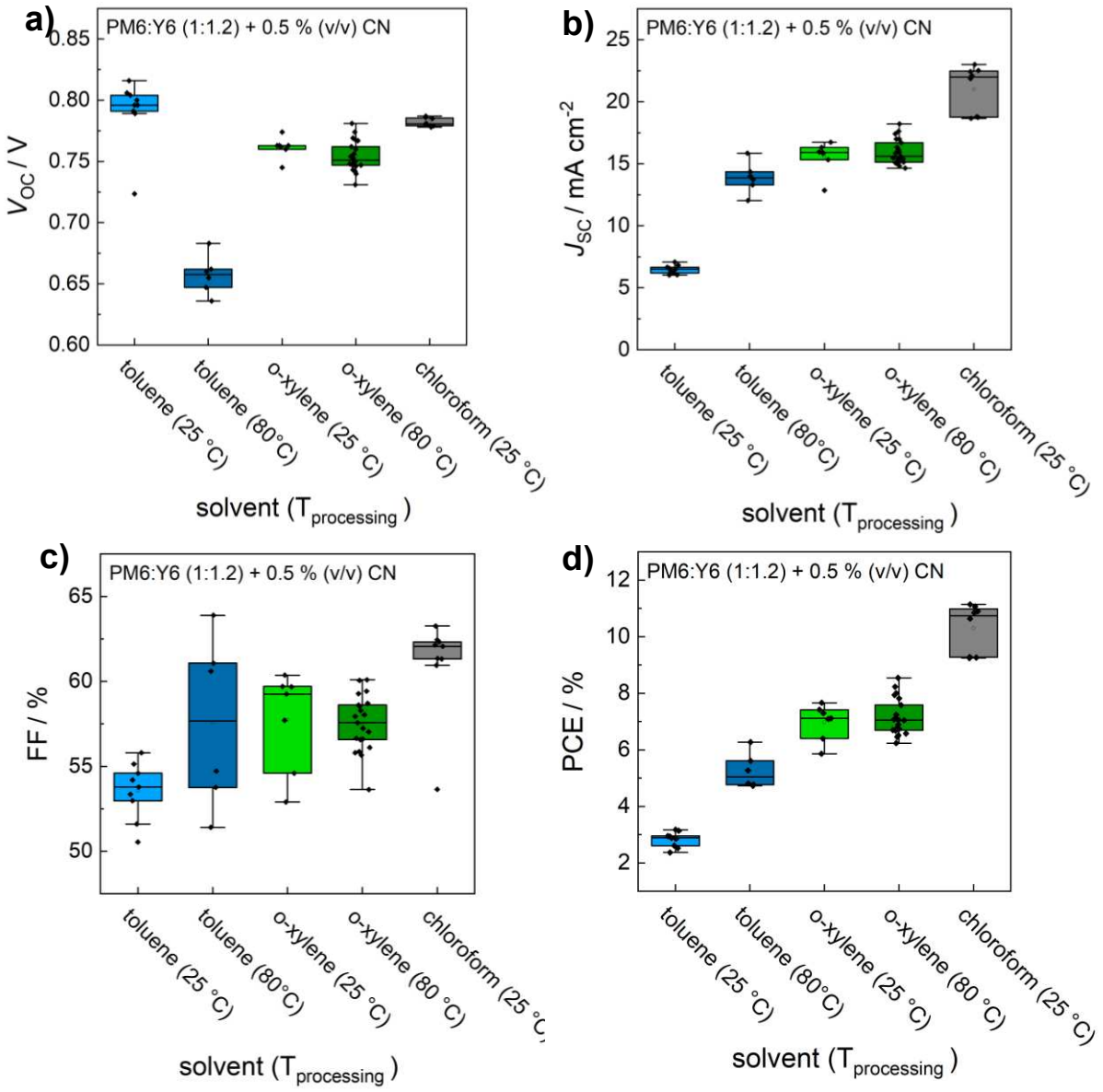

Figure 9. Box plot diagrams of solar cell parameters obtained from current-voltage curves of devices fabricated by using chloroform, toluene and *o*-xylene as solvent for the D/A blend mixture, whereby **a)** the V_{OC}, **b)** J_{SC}, **c)** FF, and **d)** PCE are shown.

performed. Compared to this, for the toluene solutions coated at room temperature, only a low average PCE of 2.8 % could be obtained, whereby this PCE value could be nearly doubled for a coating temperature of 80 °C. On the other hand, the performance of o-xylene-based devices was not noticeably affected by the stirring temperature overall, showing similar PV performance. In the direct comparison with toluene, *o*-xylene-based films exhibit comparable fill factors but approx. 2 % points higher PCE values. According to Di Wang *et al.*[79], an increase in device performance could be achieved by not only heating the ink solution but also the substrate during the spin-coating process. However, this approach was not applied in this work to keep the spin-coating procedure as simple as possible as well as to provide a good

reproducibility of the fabricated devices. When directly comparing toluene and *o*-xylene as solvents, using *o*-xylene has not only led to the formation of more homogenous thin films at higher temperatures (see **Figure 8**) but also to a better PV performance of the solar cells. Consequently, toluene was not further used for the rest of this work.

3.1.3 Delayed Processing for Hot Solution Spin-Coating with CN as a Solvent Additive

As previously shown in section 3.1.2, the application of a higher stirring temperature of the ink solution directly before spin-coating has positively influenced the performance of the resulting devices. This may be attributed to a higher film homogeneity as well as to an increase in the crystallinity [52]. To ensure equal spin coating conditions for every substrate during hot processing, it was investigated how variations in the delayed processing time affect the performance of the solar cell (experimental details see section 2.3.3). In this respect, the delay time refers to the period between the transfer of the ink from the vial onto the substrate and the activation of the spin-coating program. Different delay times were tested for the preparation of solar cells with PM6:Y6 active layers processed from *o*-xylene, with and without 0.5 % (v/v) CN additive. The PV performance data of the devices can be seen in **Table 8**, whereby the data of solar cells with a FF above 45 % was considered for the statistics (see section 2.5.2).

Table 8. PV performance of devices prepared from 16 mg mL^{-1} PM6:Y6 (1:1.2, w/w) solutions in *o*-xylene with 0.5 % (v/v) CN and without additive using different delayed processing times.

Additive	Delay time / s	V_{OC} / V	J_{SC} / mA cm^{-2}	FF / %	PCE / %	n
w.o.	20	0.74 (0.74 ± 0.00)	12.5 (12.6 ± 0.2)	60 (59 ± 1)	5.8 (5.7 ± 0.1)	3
	30	0.75 (0.74 ± 0.00)	12.5 (12.3 ± 0.2)	60 (60 ± 0)	5.8 (5.7 ± 0.1)	3
	40	0.75 (0.74 ± 0.01)	12.4 (12.1 ± 0.3)	59 (60 ± 1)	5.7 (5.6 ± 0.1)	3
	60	0.75 (0.74 ± 0.00)	12.3 (12.0 ± 0.3)	60 (61 ± 1)	5.8 (5.7 ± 0.1)	3
0.5 % (v/v) CN	20	0.76 (0.76 ± 0.00)	17.8 (17.3 ± 0.8)	58 (58 ± 0)	7.6 (7.4 ± 0.3)	3
	30	0.76 (0.76 ± 0.00)	16.1 (16.1 ± 0.2)	60 (60 ± 1)	7.2 (7.2 ± 0.0)	3
	40	0.76 (0.76 ± 0.00)	16.8 (16.6 ± 0.4)	59 (58 ± 1)	7.4 (7.2 ± 0.0)	3
	50	0.75 (0.76 ± 0.01)	16.3 (16.4 ± 0.8)	58 (58 ± 1)	7.0 (6.8 ± 0.2)	3
	60	0.76 (0.76 ± 0.01)	17.2 (16.6 ± 0.8)	58 (58 ± 0)	7.5 (7.0 ± 0.5)	3

It can be seen in **Table 8** that upon variating the delay duration, a similar device performance could be obtained, whereby this effect was the same for devices with and without additives. Consequently, it was assumed that temperature changes within this period do not affect the spin-coating conditions and, consequently, also the PV performance. Due to this reason, a delay time between 20 s to 1 min was used for all following experiments using the spin-coating process for *o*-xylene solutions.

Another important observation is that the cell processed with CN as an additive showed higher J_{SC} as well as higher PCEs of more than 1 % points. This observation can be related to the fact that CN is reported to induce increased molecular π-stacking, which results in improved film crystallinity and phase segregation [41,58,80]. As already described in section 1.2, solvent additives like CN influence the drying behavior of the wet film, resulting in a specific vertical distribution of the D/A material within the photoactive layer [58]. In more detail, during the drying period of the coated film, the o-xylene will evaporate first, which increases the local concentration of CN due to its lower volatility. This is enlarging the difference in solubility within the PM6:Y6 blend. As soon as CN is evaporated, the Y6 material is more concentrated at the bottom of the layer as it shows a lower solubility towards CN. Oppositely, the PM6 material accompanies CN and accumulates at the top part of the film [58,59].

Since CN represents a frequently used high-boiling solvent additive and has enhanced the device performance, it will be used as an additive in the standard ink solution, as described in section 2.3.3.

3.1.4 D/A Blend Composition of the Photoactive Layer

To further improve the morphology of the photoactive layer and, consequently the device performance, different PM6:Y6 blend ratios were tested (see section 2.3.4 for experimental details). The calculation for the statistic representation includes only the measurement data of cells prepared in this experiment series. This should ensure a similar processing environment in terms of humidity or air temperature within the experimental series. Furthermore, only the PV performance of solar cells having a FF above 50 % was considered for the statistic (see section 2.5.2). In **Table 9**, the obtained characteristic PV parameters are listed whereby the data is extracted from current-voltage curves measured for devices using different PM6:Y6 weight ratios. Additionally, **Figure 10** shows the corresponding box plot diagram for V_{OC}, J_{SC}, FF, and PCE of the respective PM6:Y6 blend ratios.

Table 9. Average performance of the device from 16 mg mL^{-1} PM6:Y6 solutions in *o*-xylene with 0.5 % (v/v) CN using different PM6:Y6 blend weight ratios.

weight ratio (D:A)	V_{OC} / V	J_{SC} / mA cm^{-2}	FF / %	PCE / %	n
1:1	0.77 (0.76 ± 0.01)	16.9 (15.7 ± 0.9)	53 (53 ± 1)	6.9 (6.3 ± 0.5)	12
1:1.2	0.74 (0.73 ± 0.01)	21.8 (20.2 ± 1.0)	63 (61 ± 1)	10.1 (9.0 ± 0.6)	11
1:2	0.75 (0.73 ± 0.02)	15.7 (13.1 ± 1.3)	65 (60 ± 4)	7.3 (5.6 ± 0.8)	11

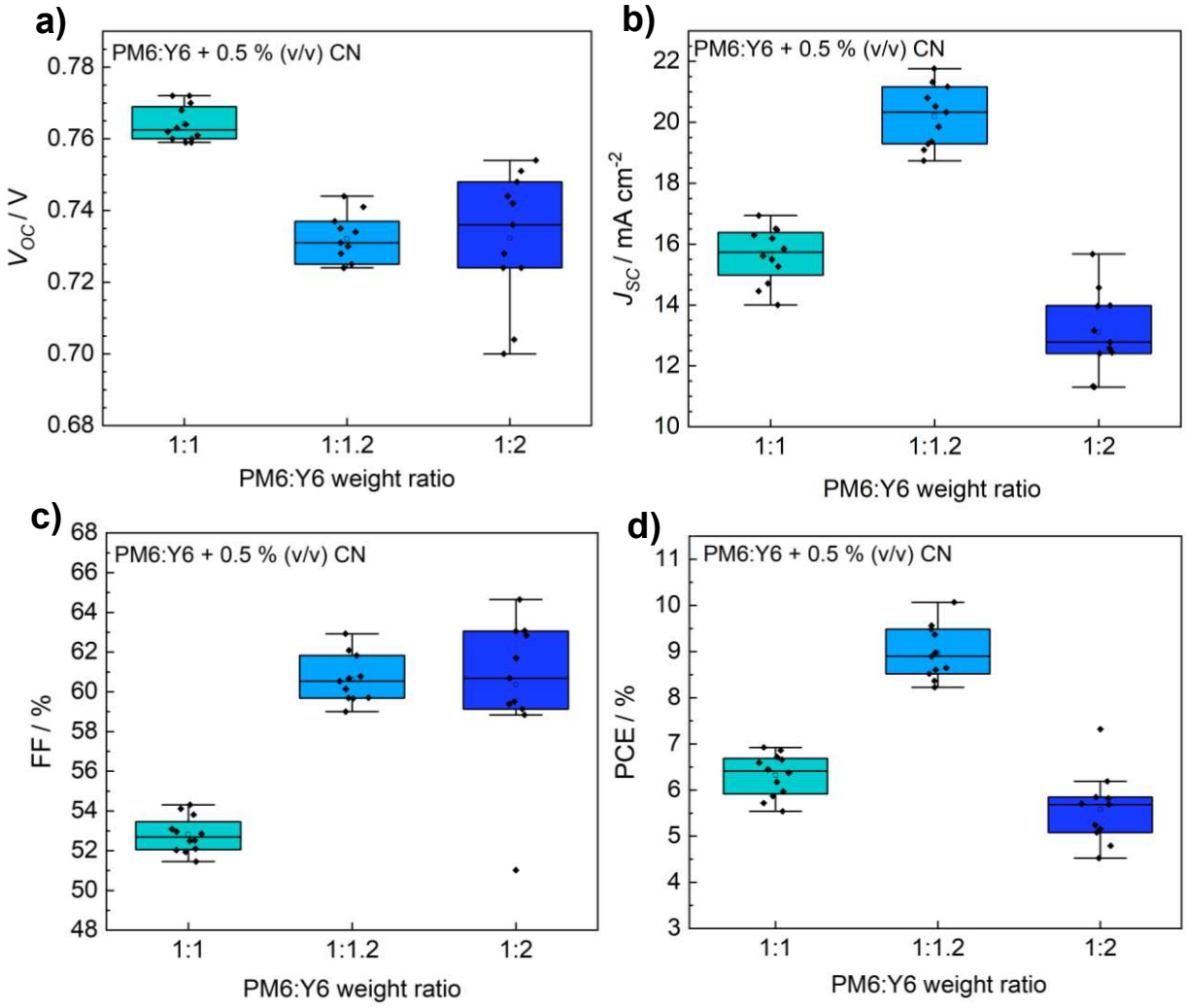

Figure 10. Box plot diagrams of characteristic PV parameters obtained from current-voltage curves of devices prepared from different PM6:Y6 blend weight ratios., whereby **a)** the V_{OC}, **b)** J_{SC}, **c)** FF, and **d)** PCE are shown.

As seen in **Table 9**, the highest average J_{SC} and PCE was obtained for the 1:1.2 (w/w) PM6:Y6 blend mixture. This observation is similar to the experimental results found by Zhou *et al.* [81]. In their work, they stated that the best performance could be produced using a D/A weight ratio of 1:1 achieving a PCE of 17.23 % and a FF of 77.65 %. As the second-best blend ratio, a ratio of 1:1.2 with a PCE of 15.24 % and a FF of 75.46 % was reported. Here, it has to be mentioned that in this literature (publication) a different device structure was used as well as PM6:Y6 was dissolved in chloroform [81]. In general, a higher concentration of Y6 molecules in the blend mixture leads to a better performance owing to a higher degree of exciton and charger carrier diffusion in the acceptor moieties. When using similar amounts of D and A in the blend mixture, the film morphology can be improved which results in an enhanced exciton diffusion as well as transport of charge carriers. Simultaneously, the recombination of excitons and charge carriers is hindered leading to a notably increased J_{SC} [81]. The results of this experiment (see **Table 9** and **Figure 10**) are in accordance with this theory. The significantly highest average J_{SC} (20.2 mA cm^{-2}) as well as average PCE (9.0 %) could be obtained for a blend weight ratio of 1:1.2. In contrast to this, for a 1:1 and 1:2 D/A blend ratio only a J_{SC} of 15.7 and 13.1 mA cm^{-2} as well as a PCE of 6.3 and 5.6 % was obtained, respectively.

3.1.5 HTL Thickness

To further optimize the standard processing procedure for solar cells, the influence of the hole transport layer (MoO_x) thickness on the performance of the prepared solar cells was examined (for experimental details see section 2.3.5). The results of this experiment are presented in **Table 10** and **Figure 11**, whereby for the calculation of the statistic distribution only the PV performance of devices with a FF above 42 % was included (see section 2.5.2).

This experiment has shown that a higher PV performance was obtained for devices prepared with MoO_x layer thickness of ≥ 10 nm. However, devices with a 10 nm HTL show slightly better PV parameters than the other layer thicknesses. As a consequence, 10 nm was chosen as the standard HTL thickness for the rest of this work for both the spin-coating as well as the blade-coating process which will be discussed later in this work.

Table 10. Average performance of the device from 16 mg mL^{-1} PM6:Y6 (1:1.2, w/w) solution in *o*-xylene using different thicknesses of the MoO_x layer (HTL).

d_{MoOx} / nm	V_{OC} / V	J_{SC} / mA cm^{-2}	FF / %	PCE / %	n
5	0.75 (0.73 ± 0.01)	14.1 (12.7 ± 1.1)	54 (53± 0)	5.6 (4.8 ± 0.5)	6
7	0.73 (0.72 ± 0.01)	12.9 (12.3 ± 0.4)	52 (50 ± 2)	4.7 (4.3 ± 0.3)	6
9	0.74 (0.75 ± 0.00)	12.6 (11.9 ± 0.6)	51 (50 ± 1)	4.7 (4.4 ± 0.2)	4
10	0.75 (0.75 ± 0.01)	16.7 (15.1 ± 0.7)	57 (56 ± 1)	7.1 (6.3 ± 0.4)	13
11	0.76 (0.75 ± 0.00)	14.5 (13.9 ± 0.5)	55 (55 ± 1)	6.1 (5.7 ± 0.3)	3
15	0.76 (0.75 ± 0.01)	14.7 (14.4 ± 0.5)	57 (56 ± 0)	6.4 (6.0 ± 0.3)	6

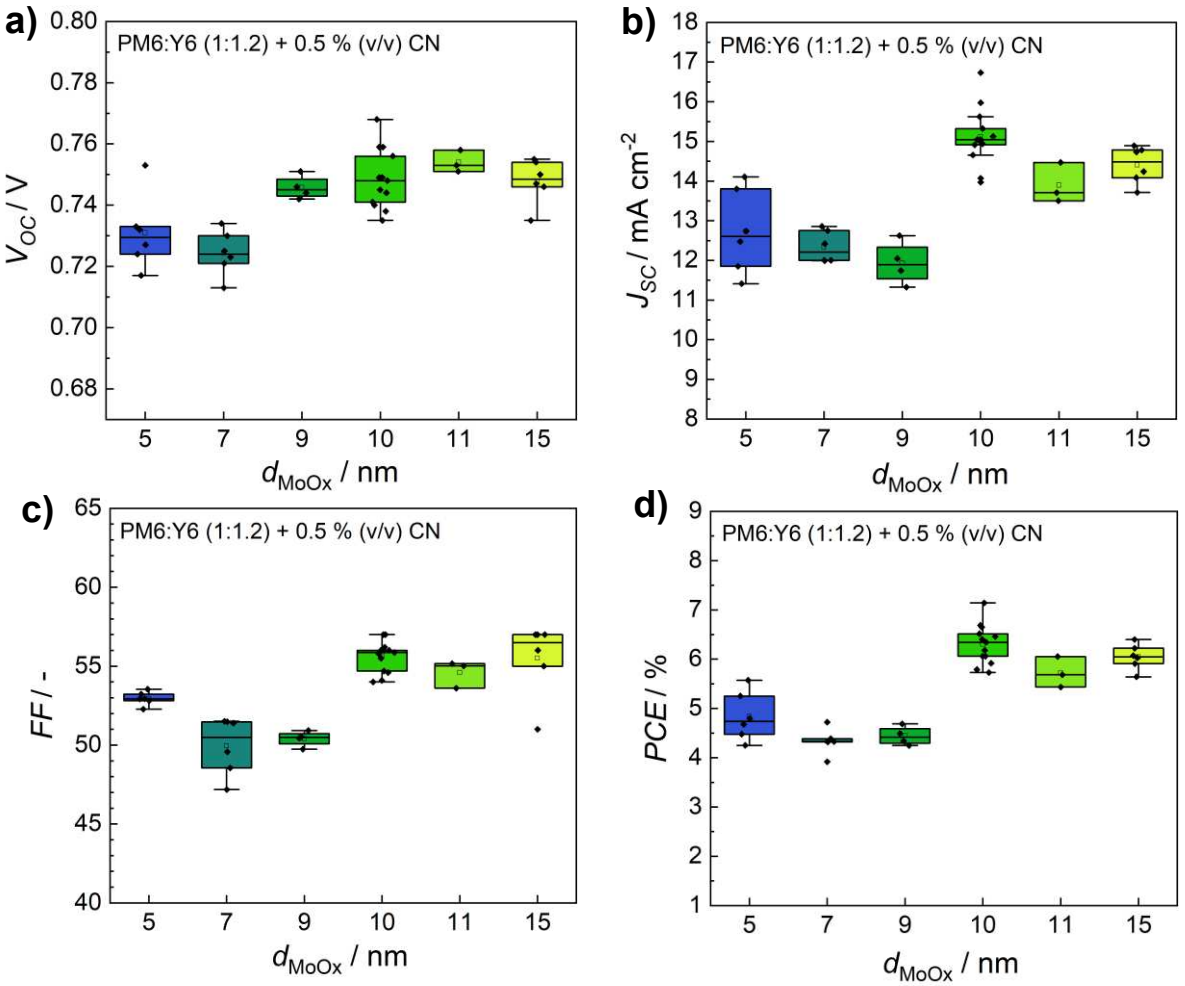

Figure 11. Box plot diagrams of solar cell parameters obtained from current-voltage curves of devices with a different MoO_x layer thickness *d*, whereby **a)** the V_{OC}, **b)** J_{SC}, **c)** FF, and **d)** PCE are shown.

3.1.6 Annealing Temperature of the Photoactive Layer

As previously mentioned, thermal annealing can be applied to improve the morphology and performance of the device [54,82,83]. The used Y6 acceptor material has reportedly a high tendency to agglomerate upon the application of high temperatures of about 110 °C [58]. So, to further improve the phase segregation and crystallization of the photoactive layer different annealing temperatures as well as durations were examined, as described in section 2.3.6. In the first screening test, it was observed that when applying the standard annealing program (110 °C for 10 min) used in different literature procedures [72,82,84–86] an increase of 1.2 % points of the average PCE could be achieved, as shown in **Figure 12**. Interestingly, the highest increase in the average PCE could be found using a temperature of 130 °C for 5 minutes. With this program, the PCE has risen 1.8 % points. By applying a higher temperature of 150 °C, the average PCE was decreasing.

In this respect, a second annealing experiment was conducted, whereby the corresponding results are shown in **Table 11** and **Figure 13**. For the statistical evaluation of the data only devices were included that showed a FF higher than 44 %, as described in section 2.5.2). These results match the experimental data listed in **Figure 12**. As previously seen, the highest value for the average PCE and J_{SC} was obtained for a temperature of 130 °C. This temperature-dependent rise of the average J_{SC} from 14.6 to 18.3 mA cm^{-2} corresponds to the optimization of the EQE [87,88]. In this respect, Fernández-Castro *et al.* similarly found that thermal annealing at 120 °C improved the PCE of devices coated at temperatures below 80 °C [88]. Furthermore, at 140 °C the devices showed low average values for all characteristic

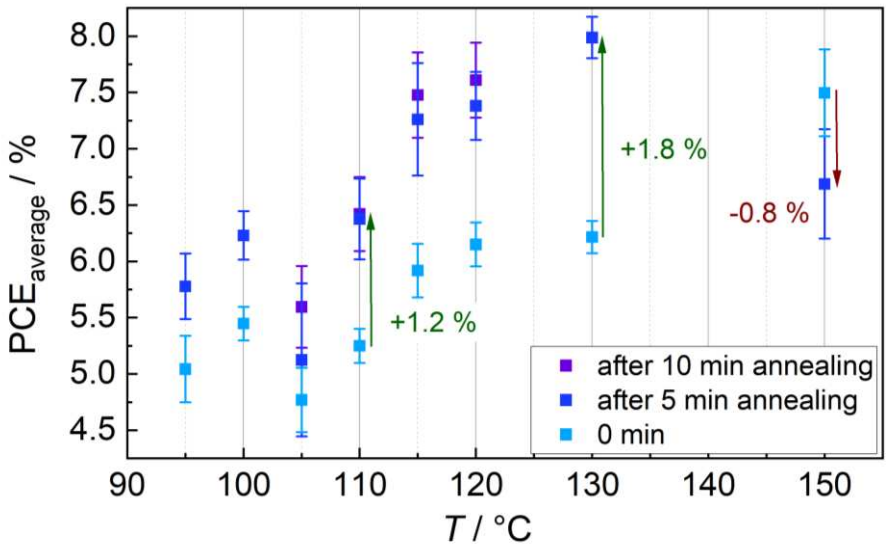

Figure 12. Average power conversion efficiency ($PCE_{average}$) as a function of the annealing temperature *T* at different annealing durations, whereby for each data point n = 3 was used for the statistical representation.

PV parameters. Considering these results, 130 °C for 5 minutes was selected as the new standard annealing program for the absorber layer.

Table 11. PV performance of the devices from standard ink solutions, whereby the annealing of the spin-coated thin film was performed for 5 minutes at different temperatures.

T / °C	V_{OC} / V	J_{SC} / mA cm^{-2}	FF / %	PCE / %	n
100	0.76 (0.76 ± 0.00)	14.8 (14.6 ± 0.5)	57 (57 ± 0)	6.4 (6.2 ± 0.2)	3
110	0.75 (0.75 ± 0.00)	16.0 (15.2 ± 0.7)	59.2 (58± 1)	7.1 (6.7 ± 0.4)	3
120	0.76 (0.75 ± 0.01)	18.1 (16.8 ± 1.0)	58.0 (59 ± 1)	7.8 (7.2 ± 0.5)	6
130	0.76 (0.75 ± 0.01)	19.8 (18.3 ± 0.3)	59.0 (60 ± 1)	8.7 (8.1 ± 0.4)	4
140	0.74 (0.74 ± 0.00)	16.2 (16.1± 0.3)	56.0 (56 ± 1)	6.5 (6.5 ± 0.0)	2

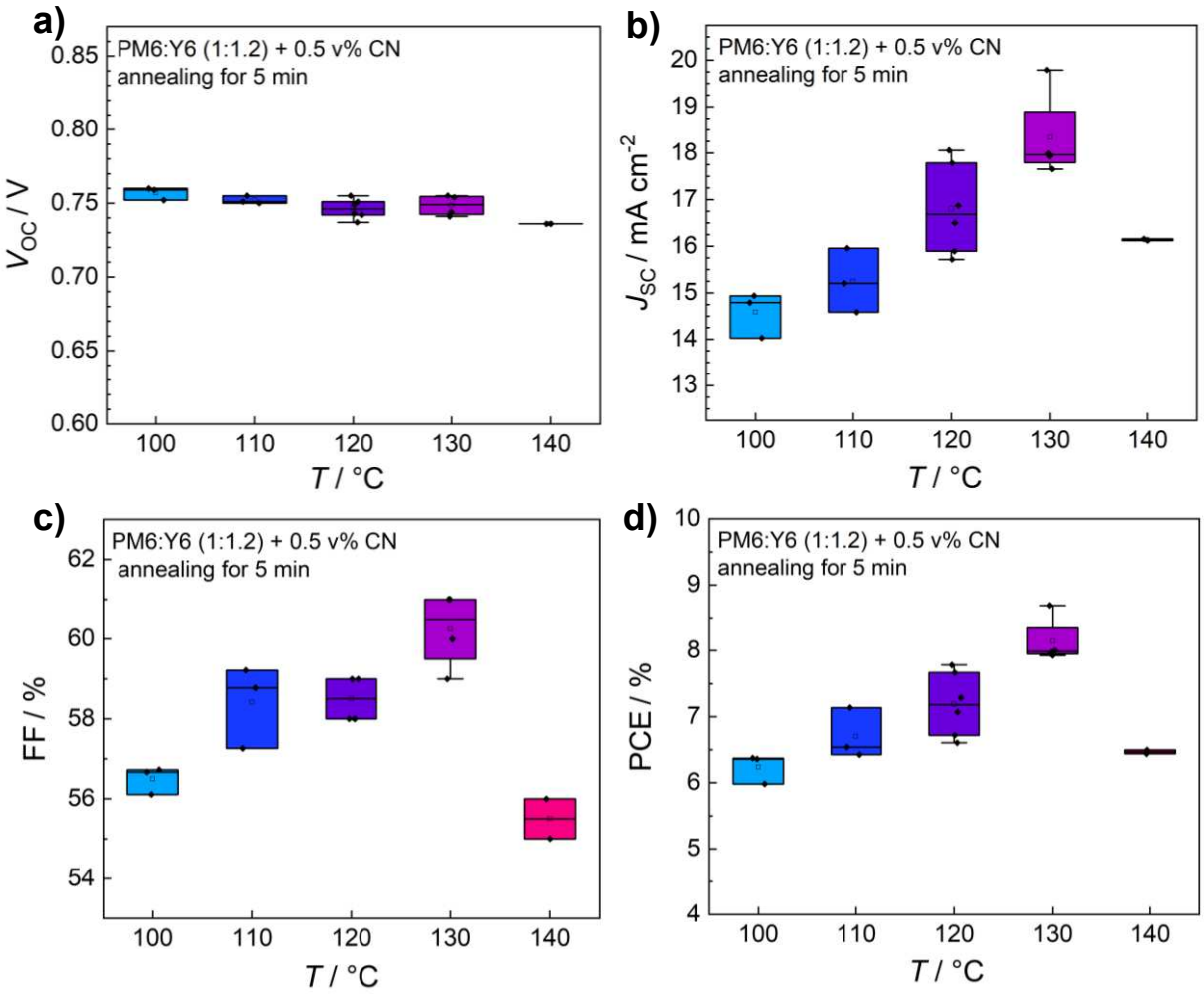

Figure 13. Box plot diagrams of the characteristic solar cell parameters extracted from current-voltage curves of devices annealed for 5 minutes at different temperatures, whereby **a)** the V_{OC}, **b)** J_{SC}, **c)** FF, and **d)** PCE are shown.

3.1.7 PTQ10 as a Solid Additive for the Photoactive Layer

Besides high boiling solvent additives, also solid materials can be mixed into the D/A material blend to improve the crystallization behavior and morphological fine structure of the film [41]. This creates a ternary blend structured film which should advantageously boost the PV performance owing to an enlarged light absorption range as well as the promotion of charge carrier generation and diffusion [89,90]. In the course of the optimization, PTQ10 (a donor molecule) was tested as a ternary solid additive in changed concentration to achieve similar device performance as obtained using chloroform as solvent (see section 2.3.2). The PV performance obtained using different concentration of PTQ10 are listed in **Table 12** and are graphically represented in box plot diagrams in **Figure 14**. It is important to note that for the calculated statistical distribution of the performance data, only devices were included that exhibited a FF value above 44 %, as described in section 2.5.2).

Although solid additives like DRTB-T-C4 [91], anthracene [85], N2200 [92] or *i*-Y6 [93] were reported to increase the PCE values for the PM6:Y6 blend system, the results of this experiment show that the addition of PTQ10 is undesirably influencing the PCE as well as the J_{SC} values, whereby the average values are decreased from 7.7 to 6.0 % and 16.8 to 14.8 mA cm^{-2} upon changing the PTQ10 concentration in the blend from 0 to 2 mg mL^{-1}, respectively. The incorporation of PTQ10 into the PM6:Y6 blend structure might change the interpenetrating network within the film and thus, has a limiting effect on the charge carrier transport [90]. To incorporate PTQ10 more effectively into the device structure PTQ10 could potentially be applied as an additional layer between photoactive and HTL instead of using a ternary mixture of two donor and one acceptor materials [90]. This approach might be investigated in further studies. However, no improvement in performance was observed under the tested conditions and therefore, PTQ10 was not further investigated in the course of this work.

Table 12. Average solar cell parameter obtained from current-voltage curves of the devices from 16 mg mL^{-1} PM6:Y6 (1:1.2, w/w) solution in *o*-xylene with 0.5 % (v/v) CN as well as the addition of different concentrations of PTQ10.

β_{PTQ10} / mg mL^{-1}	V_{OC} / V	J_{SC} / mA cm^{-2}	FF / %	PCE / %	n
0	0.77 (0.77 ± 0.01)	18.2 (16.8 ± 0.9)	59 (58 ± 2)	8.5 (7.7 ± 0.7)	9
0.5	0.75 (0.74 ± 0.01)	18.1 (17.1 ± 0.8)	58 (58 ± 0)	7.9 (7.3 ± 0.4)	6
1	0.76 (0.75 ± 0.01)	15.8 (14.8 ± 0.6)	54 (53 ± 2)	6.5 (5.9 ± 0.4)	9
2	0.76 (0.76 ± 0.01)	14.9 (14.8 ± 0.4)	56 (54 ± 1)	6.3 (6.0 ± 0.2)	9

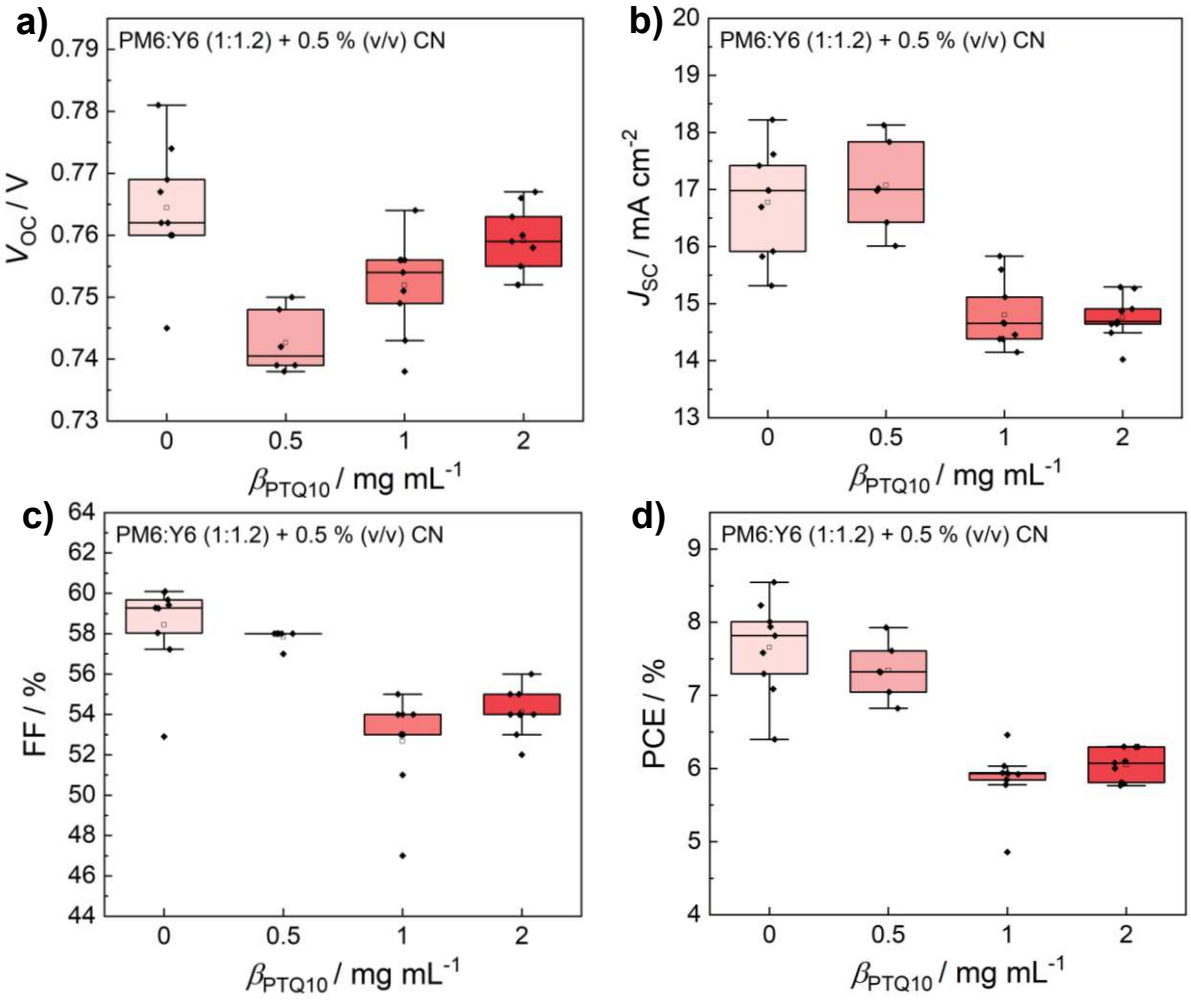

Figure 14. Box plot diagrams of characteristic PV parameters obtained from current-voltage curves of devices prepared using different concentrations of PTQ10 as a solid additive to the standard ink solution, whereby **a)** the V_{OC}, **b)** J_{SC}, **c)** FF, and **d)** PCE are shown.

3.1.8 Influence of Inert Conditions on Performance of Spin-Coated Devices

Since throughout this study the standard solar cells (prepared according to section 2.2.) showed varying values of the device parameters, it was investigated whether inert processing conditions during the coating and annealing of the photoactive layer would change the PV performance. The obtained PV performance of the devices prepared partly under ambient (approx. 30-65 % humidity) and inert conditions (approx. 1 ppm water) are listed in **Table 13** and graphically exhibited as box plot diagrams in **Figure 15**. The performance data of devices showing a FF below 43 % were excluded from the statistical representation (see section 2.5.2).

In literature, it was already observed that surrounding influences like ambient humidity affect the processing conditions and thus the device performance. However, the tolerance concerning humidity can change depending on the used D/A materials. As reported by Xu *et al.* [94] some material combinations can withstand a humidity level of up to 80 % without

significant change in the device performance. As visible in **Table 13**, the inert condition did not improve the PV performance of the devices. This result suggests maintaining the fabrication of the solar cells under ambient conditions. Additionally, with respect to an industrial application the employment of large-scale fabrication (e.g. roll-to-roll production [60]) would be facilitated since no inert room is necessary [68,94].

Table 13. PV performance of devices from standard ink solutions, whereby the spin-coating and the annealing step was performed at ambient or inert (glovebox) conditions.

Condition	V_{OC} / V	J_{SC} / mA cm^{-2}	FF / %	PCE / %	n
Ambient	0.75 (0.74 ± 0.01)	15.9 (15.6 ± 0.6)	58 (57 ± 1)	6.9 (6.6 ± 0.4)	6
Inert	0.76 (0.75 ± 0.01)	16.5 (15.4 ± 0.8)	57 (57 ± 1)	7.1 (6.5 ± 0.4)	6

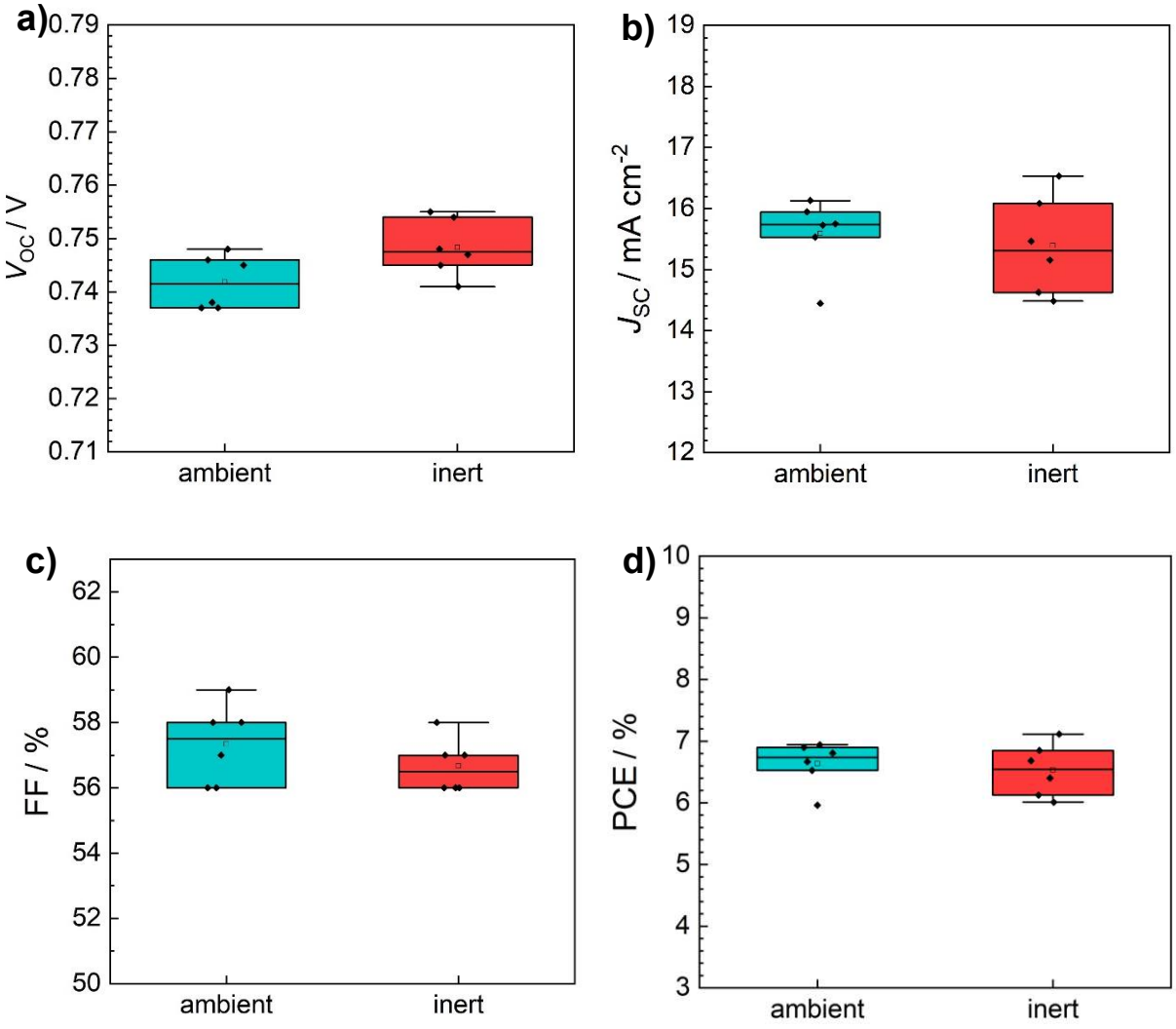

Figure 15. Box plot diagrams of the PV performance of devices whose active layer was processed under ambient and inert conditions with **a)** showing the V_{OC}, **b)** the J_{SC}, **c)** the FF, and **d)** the PCE.

3.2 Optimization of Device Fabrication Using Blade-Coating

3.2.1 Thickness and Blade-Coating Temperature of the Photoactive Layer

Similarly, to the spin-coating, the thickness of the photoactive layer needs to be optimized for the blade-coating process. Therefore, the blade-coating was performed at a plate temperature of 56 °C using different coating speeds to obtain active layer films with different thicknesses (for further experimental details see section 2.3.9). The obtained PV performance for each respective film thickness is shown in **Table 14**. For the statistical presentation of the measured data, only devices with a FF above 50 % were included (see section 2.5.2). The corresponding graphical representation of the PV performance can be seen in **Figure 16**.

Interestingly, a similar trend could be observed in this experiment as already seen for the spin-coating process. Over the whole range of investigated thicknesses, a similar average PCE was obtained, whereby the J_{SC} increased with increasing thickness. This observation might be explained by the fact that thicker layers of photoactive material can absorb more light and thus provide a larger number of charge carriers that can be extracted [95,96]. If the thickness of the photoactive layer exceeds a certain value, the charge transport to the electrodes is hindered due to the presence of charge-trapping states [95]. Moreover, a layer thickness of 90 nm was selected for the next experiment, which was obtained by a blade-coating speed of 12.5 mm s^{-1} when used with the process conditions as described in section 2.2.2.

Table 14. Characteristic solar cell parameters of the devices prepared from a standard ink solution with different absorber layer thicknesses, which were coated at 56 °C.

d* / *nm	**V_{OC} / V**	**J_{SC} / mA cm^{-2}**	**FF / %**	**PCE / %**	**n**
80	0.75 (0.73 ± 0.01)	19.2 (18.0 ± 1.1)	65 (63 ± 2)	9.3 (8.3 ± 0.7)	7
90	0.72 (0.72 ± 0.00)	20.3 (18.9 ± 0.9)	63 (61 ± 3)	9.2 (8.2 ± 0.6)	11
100	0.74 (0.73 ± 0.01)	19.6 (19.1 ± 1.1)	64 (61 ± 3)	9.3 (8.5 ± 0.6)	15
120	0.72 (0.72 ± 0.00)	20.3 (21.0 ± 0.6)	59 (59 ± 1)	9.2 (8.9 ± 0.2)	8

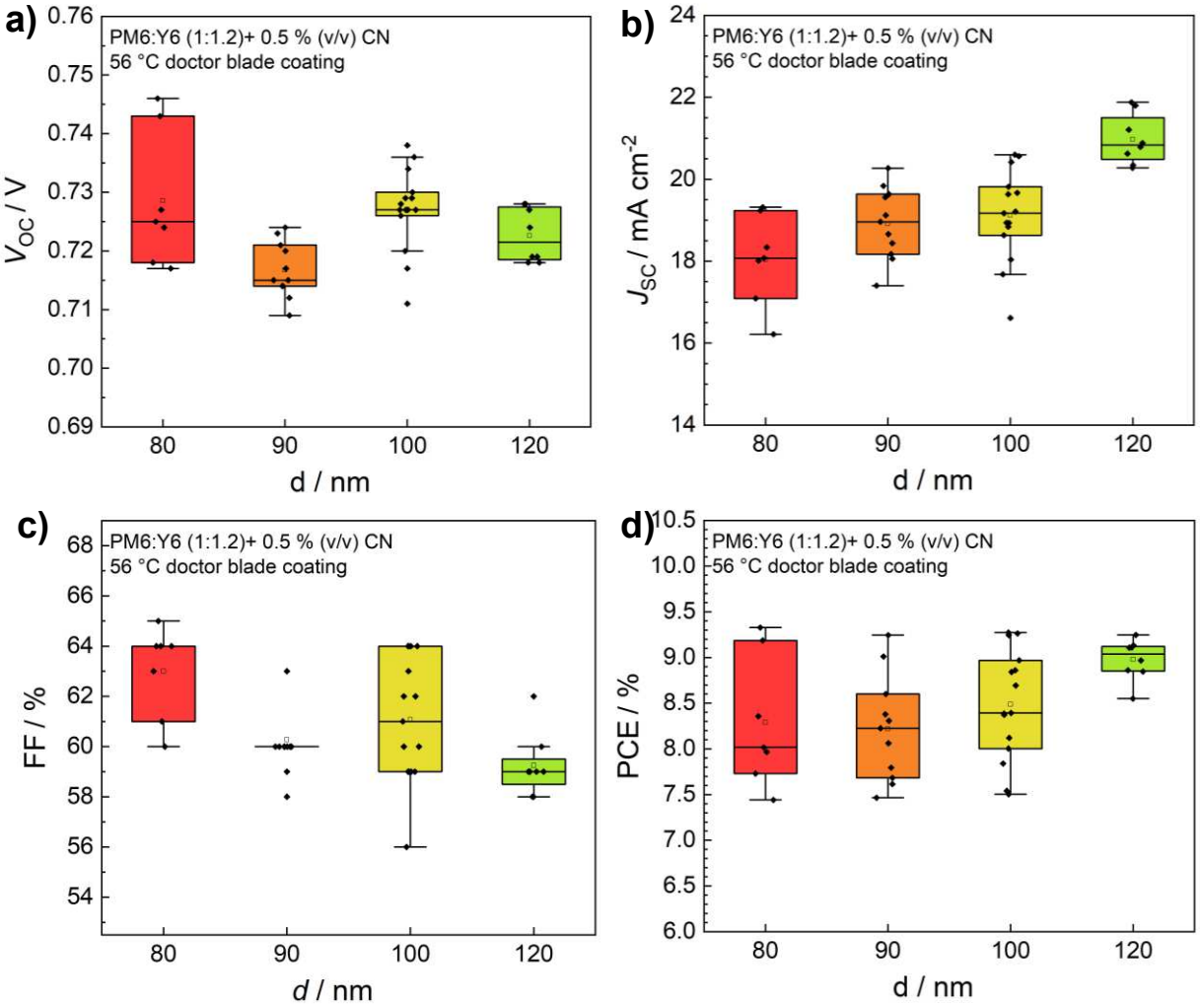

Figure 16. Box plot diagrams representing the specific PV parameters obtained from current-voltage curves of devices with photoactive layers of varied film thickness fabricated by blade-coating at a constant plate temperature of 56 °C, whereby **a)** the V_{OC}, **b)** J_{SC}, **c)** FF, and **d)** PCE are shown.

An important parameter that needs to be considered during the process optimization is the blade-coating temperature (plate temperature). According to Ro *et al.* [97], the temperature not only influences the viscosity and drying dynamics of the ink solution but also affects the morphology of the formed film. Consequently, different temperatures were tested using a constant blade-coating speed of 12.5 mm s^{-1} (see section 2.3.9 for further experimental details).

The PV performance parameters obtained from the current-voltage curves of the produced devices are shown in **Table 15** as well as in **Figure 17**. For the statistical evaluation, only devices with a FF of above 51 % were considered, as described in section 2.5.2.

Table 15. PV performance of devices prepared from standard ink solutions, which were used for blade-coating operated at a speed of 12.5 mm s^{-1} at different plate temperatures.

T / °C	V_{OC} / V	J_{SC} / mA cm^{-2}	FF / %	PCE / %	n
56	0.72 (0.72 ± 0.01)	19.0 (17.3 ± 1.1)	60 (60 ± 1)	8.2 (7.4 ± 0.5)	15
70	0.74 (0.73 ± 0.01)	19.3 (19.6 ± 0.7)	63 (63 ± 1)	9.6 (9.0 ± 0.5)	6
80	0.75 (0.74 ± 0.00)	22.4 (21.5 ± 0.4)	66 (65 ± 1)	11.0 (10.4 ± 0.3)	8
90	0.75 (0.74 ± 0.01)	22.0 (21.1 ± 0.8)	65 (64 ± 1)	10.7 (10.1 ± 0.4)	8

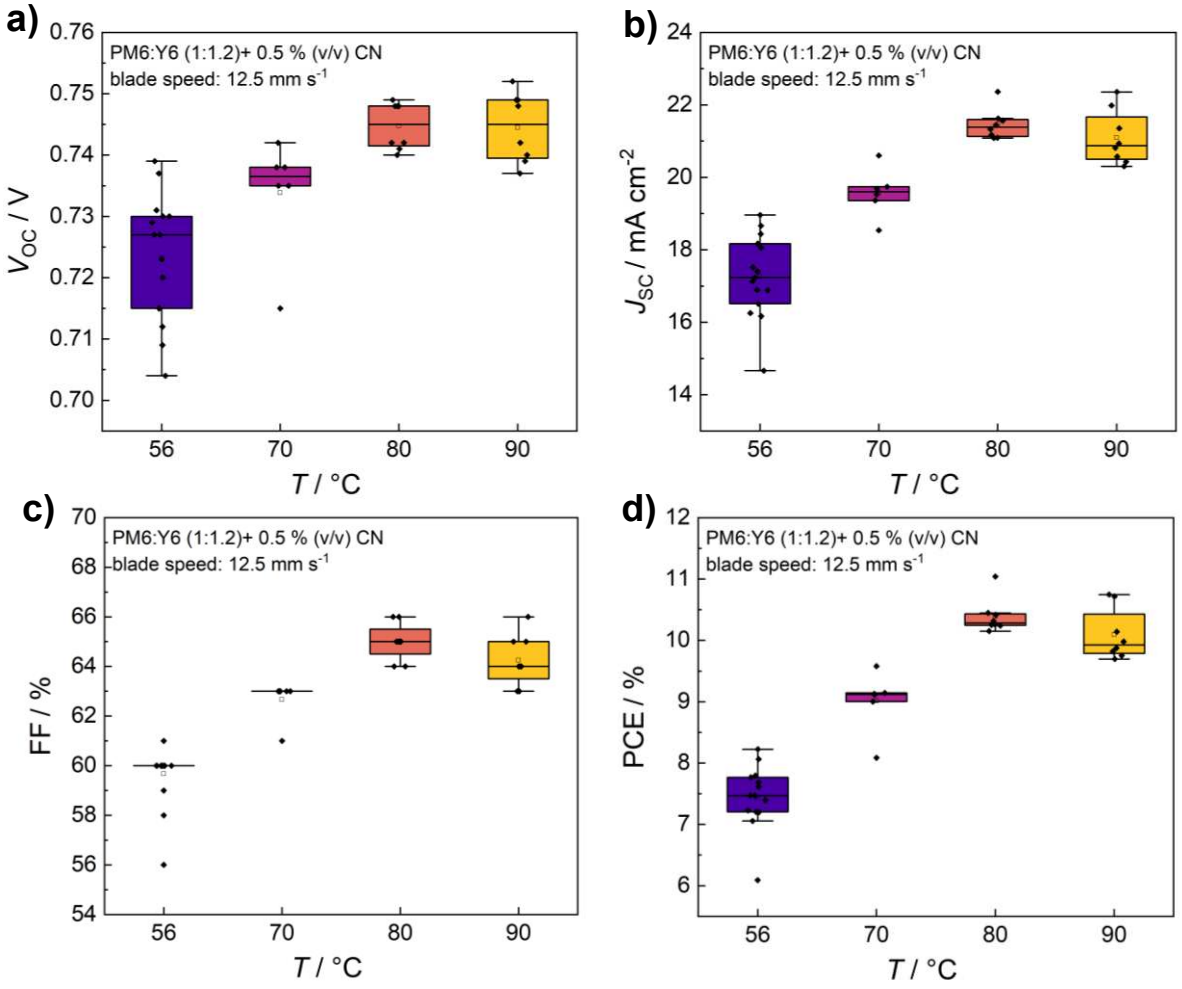

Figure 17. Box plot diagrams of the characteristic solar cell parameters obtained from current-voltage curves of devices with the photoactive layer coated at different plate temperatures at a speed of 12.5 mm s^{-1}, whereby **a)** the V_{OC}, **b)** J_{SC}, **c)** FF, and **d)** PCE are shown.

As visible in **Figure 17**, the highest average values for the J_{SC}, the FF as well as the PCE could be obtained when heating the plate to 80 °C. This result is similar to those reported by Li *et al.* [98], who found the best PV performance of PM6:Y6 devices processed from o-xylene with the additive 1,2-dimethylnaphthelene (DMN) for temperatures of 90 °C with a PCE of 15.51 %. Consequently, similar to section 3.2.1, a thickness screen was conducted to find the optimal thickness of the photoactive layer with respect to the selected plate temperature of 80 °C.

The results of this experiment match the trend that was already observed for the thickness test at 56 °C. For the data listed in **Table 16**, only the PV performance of devices with a FF above 53 % was included (see section 2.5.2). In general, all tested thicknesses except 80 nm show comparable values for the characteristic PV parameters (see **Table 16** and **Figure 18**). The deviance in performance at a thickness of 80 nm might be explained by the fact that throughout this experimental series (a period of two weeks) several devices with a thickness of 80 nm were prepared according to the process procedure (see section 2.3.9). During this period, the humidity as well as the surrounding temperature frequently changed which might have led to a variation in the PCE value [94]. Such an influence may also be a reason for the relatively large spread of the PV parameters observed for devices with a photoactive layer thickness of 80 nm, as can be observed in **Figure 18**. However, despite the spread of the values, a higher average and maximum PCE with respective values of 9.5 % and 11.2 % could be obtained with a layer thickness of 80 nm. Consequently, the respective blade-coating speed at 80 °C was selected as the standard blade-coating program (see section 2.2.2).

Table 16. Characteristic PV parameters of devices with different absorber layer thicknesses coated at 80 °C using the standard ink solution for the blade-coating process.

d* / *nm	**V_{OC} / V**	**J_{SC} / mA cm^{-2}**	**FF / %**	**PCE / %**	**n**
70	0.75 (0.74 ± 0.00)	17.9 (17.6 ± 0.3)	68 (67 ± 1)	9.1 (8.7 ± 0.2)	8
80	0.75 (0.74 ± 0.01)	22.2 (20.0 ± 1.5)	67 (64 ± 4)	11.2 (9.5 ± 1.0)	31
90	0.75 (0.74 ± 0.00)	20.5 (19.6 ± 0.9)	63 (63 ± 1)	9.7 (9.0 ± 0.4)	7
100	0.75 (0.74 ± 0.01)	19.7 (10.1 ± 0.6)	67 (65 ± 4)	9.9 (9.1 ± 0.7)	14

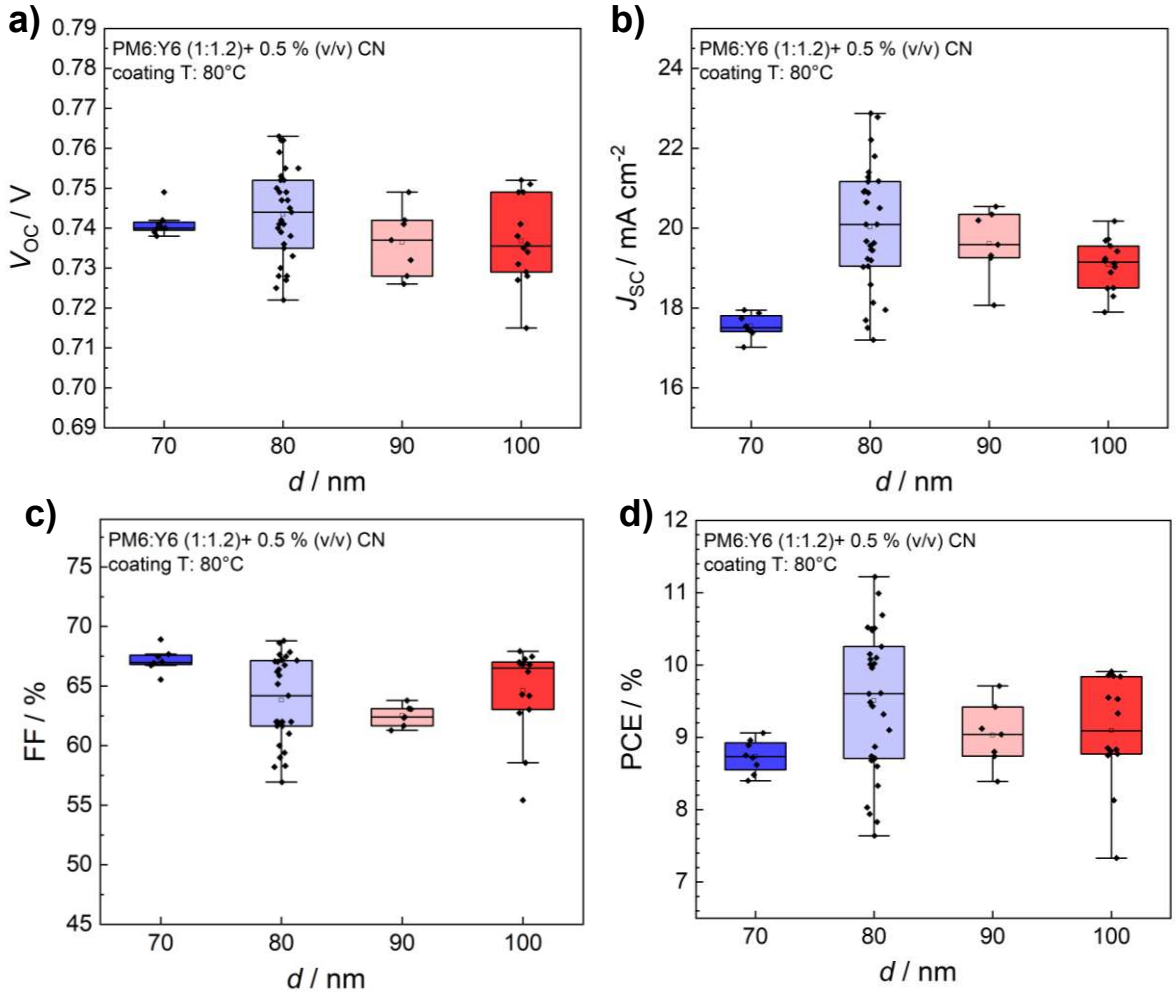

Figure 18. Box plot diagrams of solar cell parameters obtained from current-voltage curves of devices with different absorber layer thickness coated at 80 °C using the standard ink solution, whereby **a)** the V_{OC}, **b)** J_{SC}, **c)** FF, and **d)** PCE are shown.

3.2.1 Comparison of the Optimized Spin-Coating and Blade-Coating Standard Procedure

As described in section 2.2.2, the optimized procedure for the spin-coating process includes a spin-coating program of 500 rpm for 2 s followed by 1500 rpm for 30 s. For the optimized blade-coating process, a plate temperature of 80 °C was applied, whereby the coating was performed at a speed of 15 mm s^{-1}. For both coating methods, the ink solution was constantly stirred and heated to 80 °C, whereby the coating process was performed at ambient conditions. Following this, the substrates obtained for both coating methods were thermally annealed at 130 °C for 5 min, followed by the deposition of 10 nm MoO_x and 100 nm Ag. For the direct comparison of these optimized spin-coating and blade-coating process procedures, all corresponding PV performance data shown in this results and discussion section is

summarized in **Table 17** and **Figure 19**. In this way, variations in the PV performance are considered which originate in the steadily changing surrounding environment. The FF limitations for the statistics in **Table 17** are chosen in the same way as selected in every section in which the data was presented.

Table 17. Summary of the PV performance of the devices prepared using the optimized standard spin-coating and the standard blade-coating process.

Method	V_{OC} / V	J_{SC} / mA cm^{-2}	FF / %	PCE / %	n
Spin-Coating	0.76 (0.75 ± 0.01)	19.8 (16.7 ± 1.3)	59 (58 ± 2)	8.7 (7.4 ± 0.8)	19
Blade-Coating	0.75 (0.74 ± 0.01)	22.0 (20.1 ± 1.6)	69 (65 ± 3)	11.3 (9.8 ± 1.01)	87

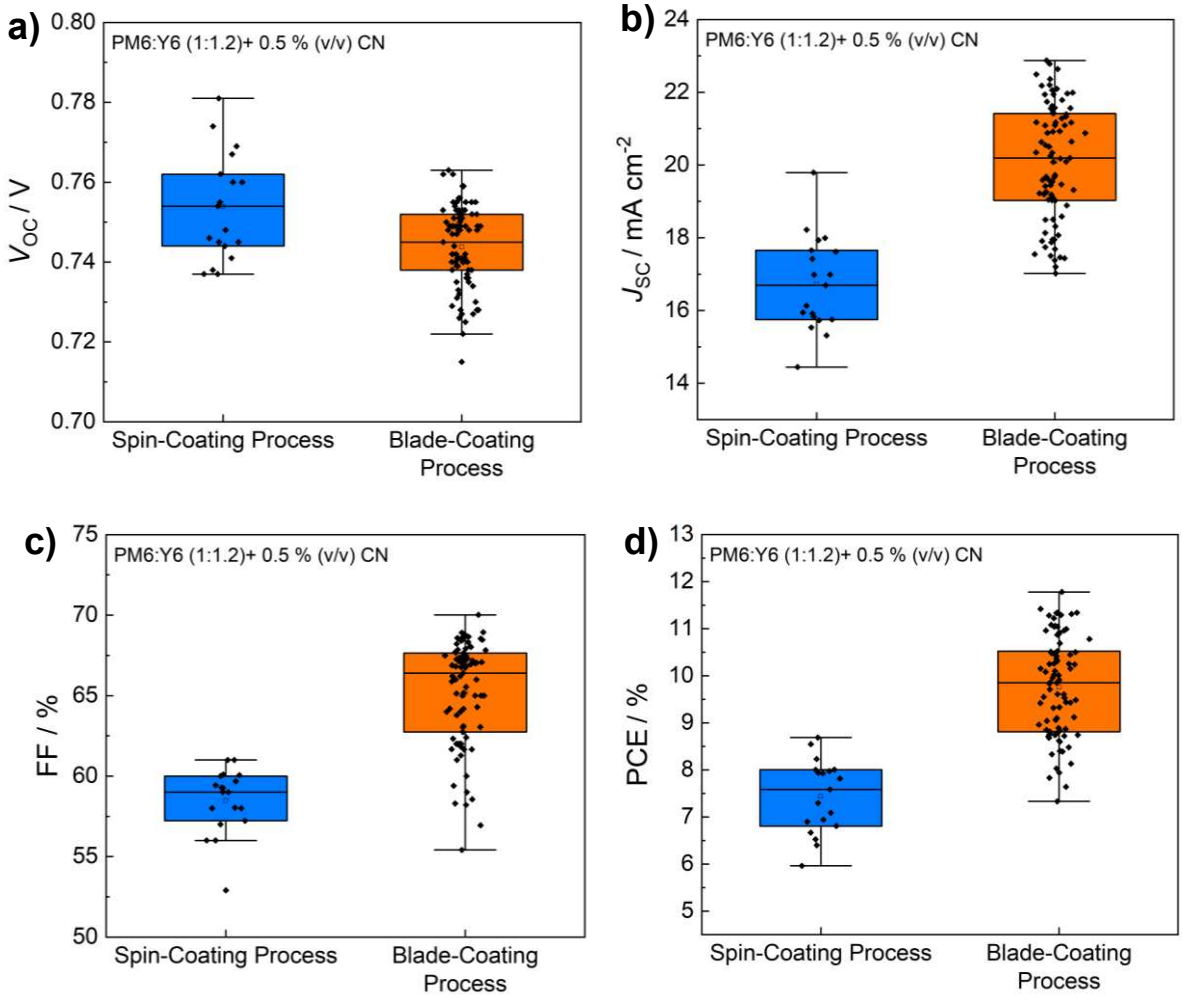

Figure 19. Comparison of the box plot diagrams of devices prepared using the optimized spin-coating and blade-coating procedures for processing PM6:Y6 active layer solution in o-xylene with 0.5 % (v/v) of CN, whereby **a)** the V_{OC}, **b)** J_{SC}, **c)** FF, and **d)** PCE are shown.

As visible in **Figure 19**, in general, a better performance could be produced with the optimized blade-coating procedure showing a maximal and average PCE of 11.3 % and 9.8 %, respectively. In contrast to this, with spin-coating only a PCE of 7.4 % (average) and 8.7 % (max.). Moreover, the J_{SC} and the FF are significantly improved for the blade-coating process, whereas the V_{OC} remained similar. A similar observation was made by Chang *et al.* [61]. They used toluene-based ink solutions, whereby the corresponding spin and blade-coated devices showed a J_{SC} of 9.3 and 11.5 mA cm^{-2}, respectively. Additionally, the FF value was higher for blade-coated solar cells, whereas the V_{OC} was unchanged [61]. A reason for this process-dependent PV performance may originate in the different coating movement directions[99] and the presence of centrifugal forces that influence the structuring mechanism of the polymer molecules during spin-coating [61]. This force is absent during blade-coating which allows the formation of a more ordered and efficient film morphology [61]. Additionally, during blade-coating the solvent, especially high-boiling solvents like o-xylene, needs more time to volatilize, which promotes the slow and continuous film formation which can be advantageous for a higher degree of crystallinity in the films [98,100]. However, to prevent uncontrolled agglomeration of donor and acceptor molecules due to this longer film drying time, the application of high temperatures can fine-tune the crystallization behavior and lead to an optimized device performance [101], which could be achieved in this work. Besides, blade-coating in contrast to spin-coating drastically reduces the waste of ink solution, which is not only environmentally important but also addresses lower material expenses [61,97,102].

Considering all this, the blade-coated devices were selected for further studies of the light-soaking stability.

3.2.2 Comparison of Solvent Additives for a Blade-Coated Absorber Layer

Similarly to the spin-coating process, the influence of solvent additives on the device performance was investigated (see section 2.3.10 for experimental details). Therefore, CN as well as 1,2-dimethylnaphthalene were tested, whereby the photovoltaic performance of the devices fabricated in this experimental series are summarized in **Table 18** and are graphically presented in **Figure 20**. For the evaluation of the statistics only devices with a FF above 55 % were included.

Interestingly, with DMN as an additive, the best-performing devices within this work could be made, whereby the average PCE corresponds to 11.9 % and the maximum PCE to 13.5 %. Additionally, the average J_{SC} is increased by a factor of 1.32 compared to devices without additives. The better performance of the devices with solvent additive can also be observed in **Figure 21**, which shows the *J-V* curves of typical devices for the respective active layer solution

type (without additive, with CN and with DMN) measured under illumination of 100 mW cm^{-2} as well as in the dark.

Table 18. Characteristic PV parameters extracted from current-voltage curves of the devices made from 16 mg mL^{-1} PM6:Y6 (1:1.2, w/w) solutions in *o*-xylene with 0.5 % (v/v) CN or DMN or without additive.

Additive	V_{OC} / V	J_{SC} / mA cm^{-2}	FF / %	PCE / %	n
w.o.	0.73 (0.73 ± 0.01)	19.9 (17.4 ± 1.3)	64 (62 ± 2)	9.3 (7.9 ± 0.7)	34
0.5 % (v/v) CN	0.75 (0.75 ± 0.01)	22.0 (21.2 ± 1.2)	69 (66 ± 2)	11.3 (10.5 ± 0.7)	50
0.5 % (v/v) DMN	0.77 (0.76 ± 0.01)	25.0 (22.9 ± 1.3)	70 (67 ± 3)	13.5 (11.8 ± 0.8)	47

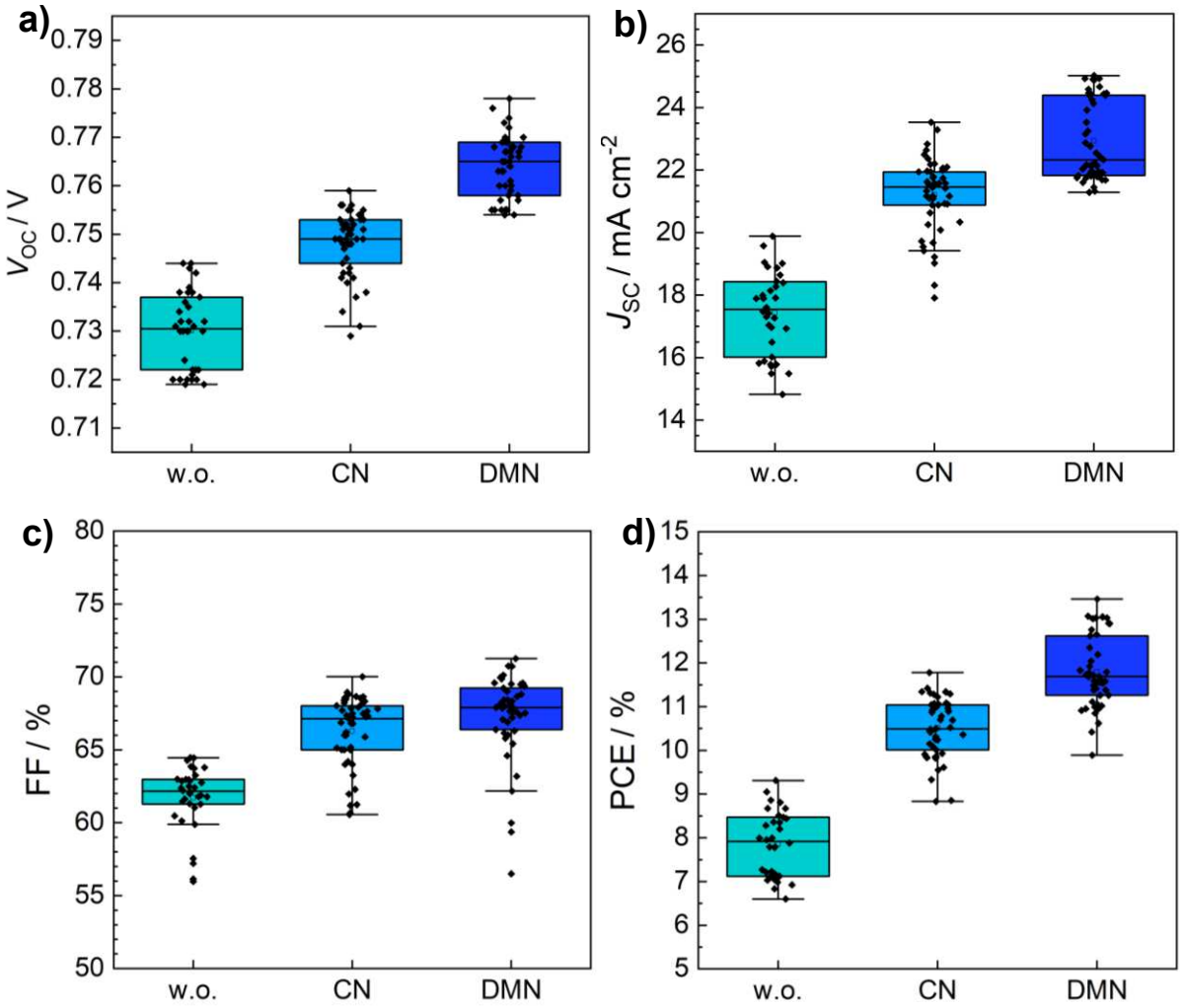

Figure 20. Box plot diagrams of the characteristic PV parameters of devices processed with the optimized standard doctor blade-coating process using different ink solutions with 0.5 % (v/v) of additive (CN or DMN) as well as without additive, whereby **a)** the V_{OC}, **b)** J_{SC}, **c)** FF, and **d)** PCE are shown.

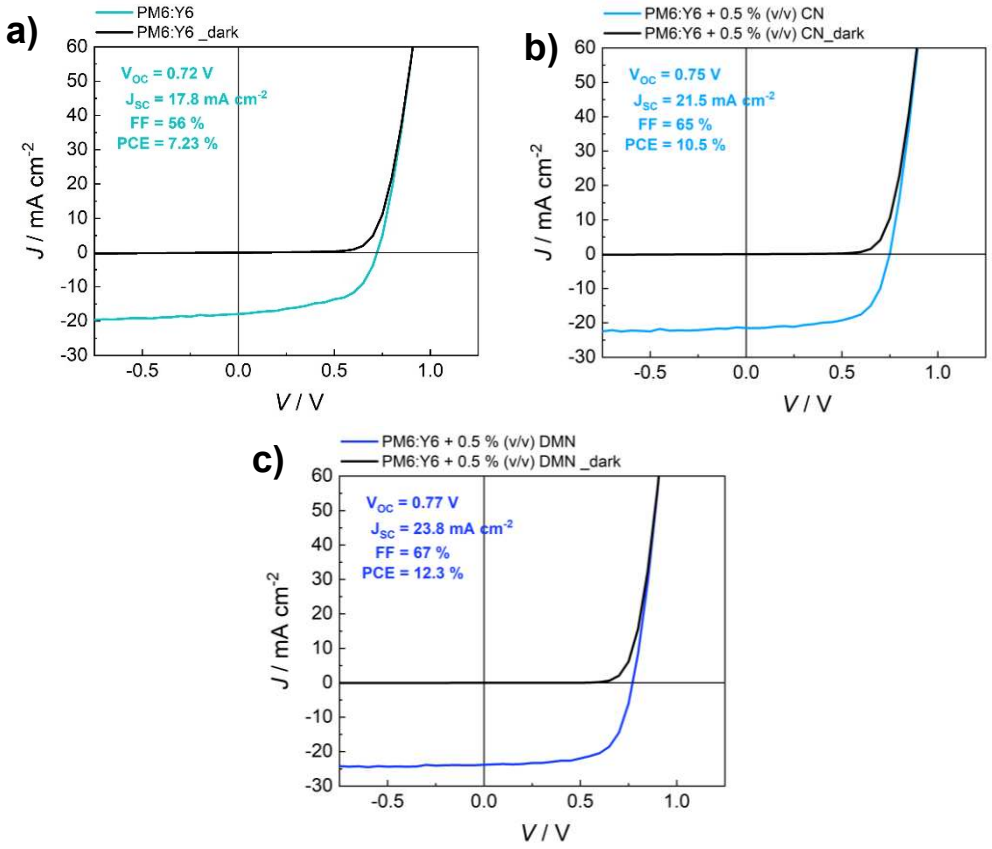

Figure 21. *J-V* curves of typical devices measured during illumination of 100 mW cm^{-2} and under dark conditions for **a)** PM6:Y6 without additive, **b)** PM6:Y6 with 0.5 % (v/v) CN, **c)** PM6:Y6 with 0.5 % (v/v) DMN.

Furthermore, the DMN devices show a higher V_{OC} compared to the pristine as well as the CN devices. Generally, devices prepared with CN also showed a better performance with respect to pristine ones, whereby this effect was not as distinct as observed for DMN. This observation might be attributed to the slight difference in boiling points of 263 °C [58] and 265 °C [103] for the additives CN and DMN, respectively. Thus, a better vertical distribution of the D/A molecules in the film may be achieved with DMN, according to the theory behind the function of high-boiling point solvent additives as proposed by McDownwell *et al.* in section 361.2 [41,53]. Additionally, DMN is a non-halogenated material that is more favorable regarding environmental friendliness in comparison to chlorinated solvents and additives [104]. When comparing this new champion system (*o*-xylene with DMN) with the chloroform-based reference recipe, not only the performance could be surpassed but the new system promotes a more sustainable and eco-friendly device fabrication without halogenated substances.

The prepared devices of this section were further used for the stability test in section 3.3 to study not only the light-soaking stability of these highly efficient OSCs but also the evaluate the influence of the solvent additives on the stability of the devices.

3.3 Light-Soaking Stability of Encapsulated Devices

Besides the device performance, the long-term stability of devices is a key factor that needs to be considered when thinking about the commercialization of OSCs [26,105–107]. Therefore, it is important to enlighten and understand the possible degradation mechanism that might occur during storage but also more importantly during the operation of the OSCs [106,108]. In this respect, different testing conditions such as inert or ambient atmosphere, light intensity, in case of illumination, as well as temperature can influence the OSC lifetime [108,109]. The encapsulation of devices plays also an important role during lifetime testing, since it can improve long-term stability by shielding the device from ambient air and water [26,86,105,106,110,111]. In the following section, stability tests of the optimized devices from section 3.2.2 are performed using different experimental conditions. Thereby, the focus lies in the comparison of three different device types whereby either no additive, CN, or DMN was used as a solvent additive.

3.3.1 Stability of Encapsulated Devices under Inert Conditions

To ensure the compatibility of the epoxy glue (EMCAST and DELO) with the standard devices as well as to exclude any related chemical degradation reaction during the operation stability tests in section 3.3.3, the devices were stored simultaneously under dark and inert conditions (glovebox conditions). In that matter, the normalized device performance parameters are plotted as a function of time for the respective used epoxy glues in **Figure 22**. The devices (G1) encapsulated with the EMCAST epoxy glue show good stability retaining 90 % of their initial PCE after a period of approx. 1000 h. Similar to this, the devices (G2) using the DELO epoxy glue experienced only a slight decrease in PCE, thereby showing 91 % of their starting PCE. As seen in **Figure 22 d)**, the PCE for both functions slightly fluctuates which could be attributed to the varying power output of the light source used for the *J-V* response measurements (see section 2.5.2) in the range of 67 – 100 mW cm^{-2}. Additionally, for both encapsulation types, the FF slowly decreases, which might be caused due to scratching the thin silver top contacts during measuring. In literature, the DELO glue has been already successfully applied for PM6:Y6 devices [112] as well as for other systems [106]. Considering all these results, it is assumed that both epoxy glues are suitable for encapsulation with respect to chemical compatibility.

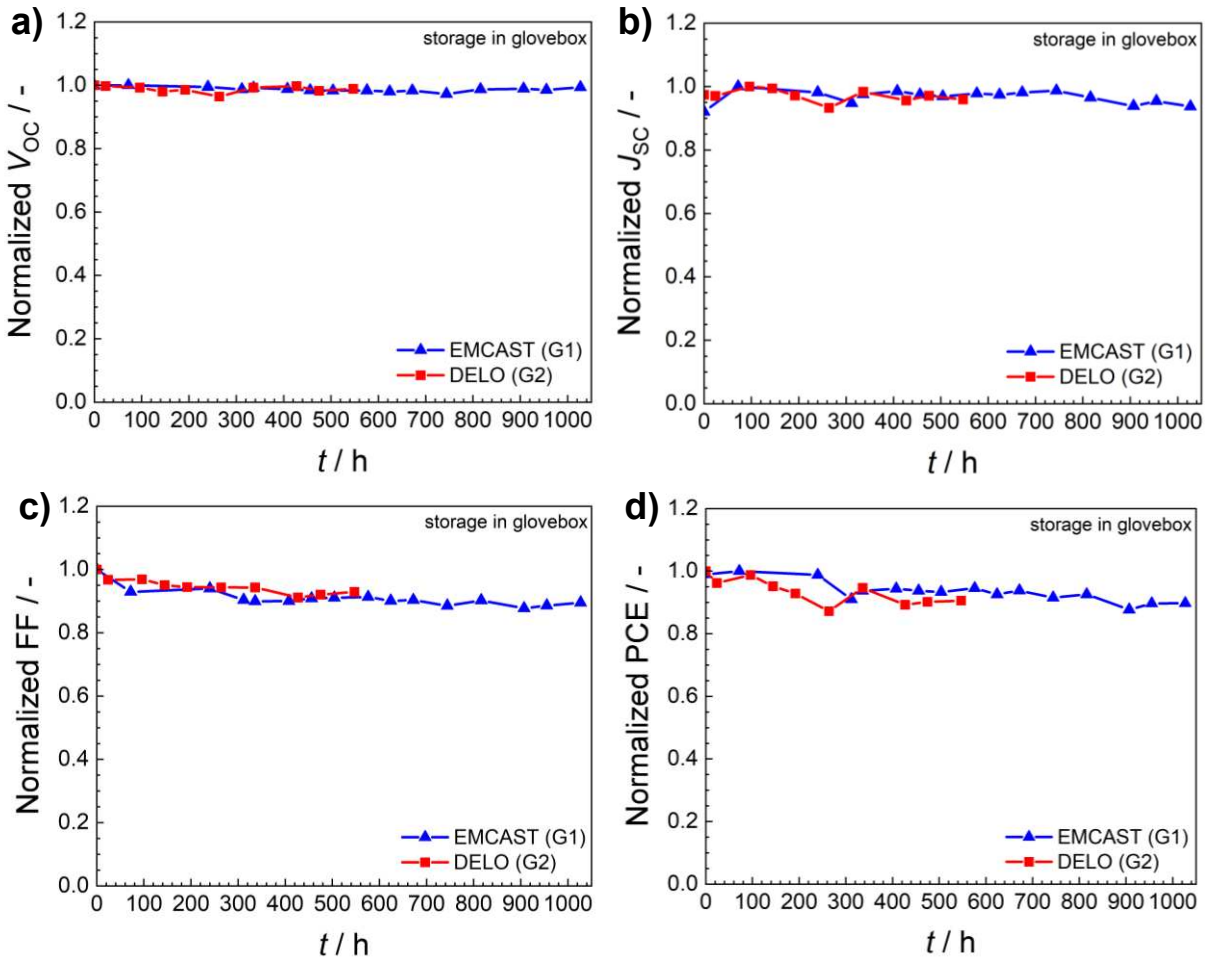

Figure 22. Comparison of the device stability over time of devices encapsulated with different epoxy glues and stored under inert atmosphere, with **a)** normalized V_{OC}, **b)** normalized J_{SC}, **c)** normalized FF, and **d)** normalized PCE plotted as a function of time. The normalization of the data points was performed on the average value considering eight devices.

3.3.2 Stability of Encapsulated Devices under Ambient Conditions

Besides the compatibility, the encapsulation was also tested under ambient conditions to evaluate its general function, as a protection shield against water and O_2. Therefore, standard devices were stored under ambient conditions, whereby the device performance was periodically measured inside a glovebox (see section 2.5.2). The results of this stability test can be seen in **Figure 23**, where the normalized parameters are plotted as a function of time for the two different encapsulation glues.

As visible in **Figure 23**, both device types (G3 and G4) only suffer a small decrease in FF as well as PCE within a period of 670 and 550 h, maintaining 88 % and 84 % of the initial PCE for the EMCAST and DELO glues, respectively. These results are slightly lower as compared to the device parameters monitored in the stability test under inert conditions. Interestingly, both J_{SC} and V_{OC} nearly constantly retained their initial value over the whole period, while the

FF slowly decreased in relation to the PCE to a FF of 92 % and 89 % of the initial value for the EMCAST and DELO encapsulated solar cells, respectively.

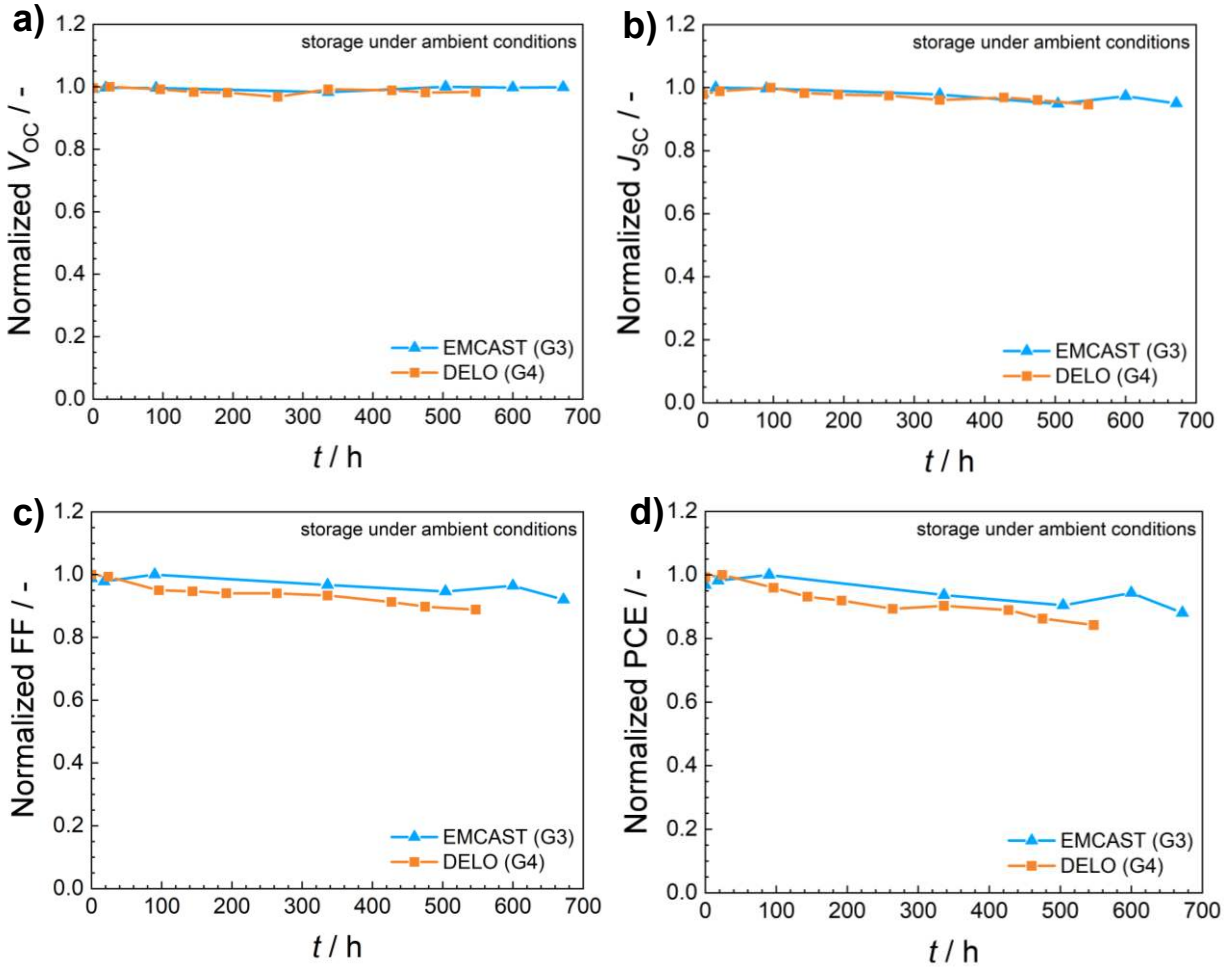

Figure 23. Comparison of the device stability over time of devices encapsulated with different epoxy glues (blue: EMCAST, orange: DELO) and stored under ambient atmosphere, with **a)** normalized V_{OC}, **b)** normalized J_{SC}, **c)** normalized FF, and **d)** normalized PCE plotted as a function of time. The normalization of the data points was performed on the average value considering eight devices.

3.3.3 Stability of Encapsulated and Operated Devices under Light Illumination

As described previously, the long-term stability of devices especially under operation is an important factor when evaluating the applicability of OSCs for commercialization [110]. The positive influence of solvent additives on the device performance has been reported for different additives [10,54,113,114] as well as shown in this work. However, it was previously found that this additive-induced change in film nanostructure might also influence the long-term stability of devices by the promoting degradation process [39,113]. According to Schaffer *et al.*, during the operation of devices with a solvent additive, the polymer moieties experience a strong reduction in size due to the volatilization of the additive molecules which leads to a

disjoint of the well-distributed nanostructure [39]. As a consequence, charge carriers cannot properly be transported via the system and accumulate in the small molecular islands which decreases the likelihood of charge carrier collection as well as in the end the FF value [39].

To examine the general light-soaking stability of the prepared devices as well as the influence of different additives, stability tests were conducted as described in section 2.4. In **Figure 24** the normalized device parameters are plotted against the measurement time for devices without additive (w.o.), with CN, and with DMN. For each device type, three functions are shown, which correspond to the operation parameter at which the stability test was performed, whereby the black line corresponds to the operation of the device at V_{OC}, red at J_{SC} and black at MPP under continuous light illumination of approx. 1200 lux which corresponds to typical room lightening conditions [115].

Interestingly, for all device types at all operation points the PCE nearly linearly decreases over time to approx. 80 % of their initial PCE except the device with DMN operated at J_{SC} which decreased until reaching a relatively constant PCE of 65 % of the starting PCE. Here, it has to be mentioned that due to the handling of the crocodile clips during the operation, the epoxy glue (EMCAST) broke on one side (see **Figure 25**) at some point in the first 50 h which produced a leakage in the sealant. This led to the assumption that the solar cell was in contact with air in contrast to the other neighboring cells on the substrate which showed still sufficient shielding. Furthermore, the J_{SC} for all devices showed a rather constant behavior reaching values of approximately. 94 % of the initial values except for the devices with CN and DMN operated at the J_{SC}. For these two solar cells, the J_{SC} decreased by 21 and 25 % of their starting values. In addition, the V_{OC} hardly changed over operation time observed for every composition at every operating point. The behavior of the FF over time follows the same trend as observed for the PCE. Since the FF, as well as the PCE, relatively decreased similarly for all device types, it is assumed that both solvent additives do not severely induce nano-structural instability in the film morphology as seen for other solvent additive systems [39,113].

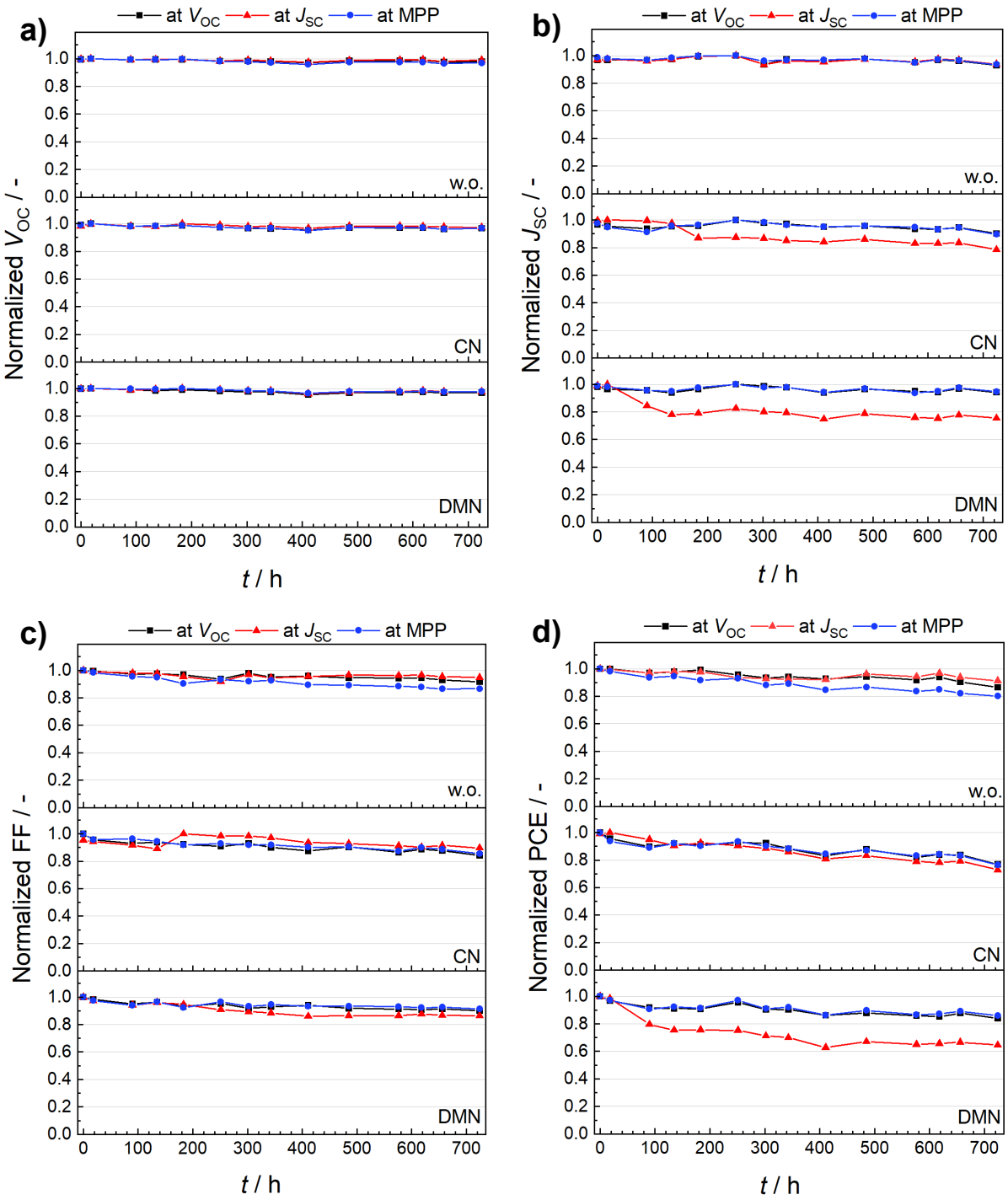

Figure 24. Comparison of the light-soaking stability (test 1) over time of devices with different solvent additives (no additive, CN and DMN), operated (black: at V_{OC}, red: at J_{SC}, blue MPP) under an illumination intensity of 1200 lux in ambient atmosphere, whereby **a)** the normalized V_{OC}, **b)** normalized J_{SC}, **c)** normalized FF and **d)** normalized PCE are plotted as a function of time; for encapsulation the EMCAST epoxy glue was used.

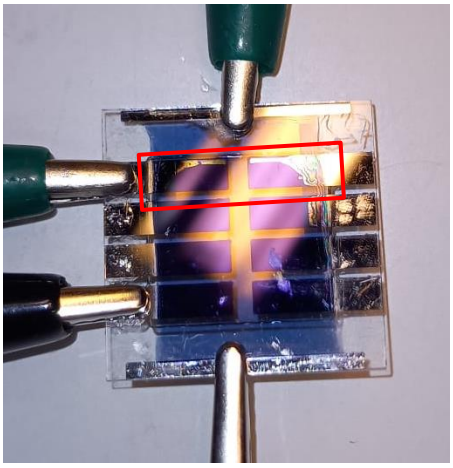

Figure 25. Picture of the one-sided broken encapsulation of a substrate using CN as additive. The red box marks the affected area, which includes the device operated at J_{SC}.

A second light-soaking stability test was simultaneously performed with test conditions equivalent to the previously discussed one to address reproducibility. The obtained results are presented in **Figure 26**.

In the second experiment, it could be observed that the V_{OC} showed a constant behavior over time in equivalence to the first light-soaking stability test (see **Figure 24**). For the J_{SC} the trend differentiated from the first test as for the pristine devices (w.o.) all three operation points strongly deviated from each other, whereby the device operated at MPP showed the lowest final value retaining 42 % of the initial J_{SC}. Following this, the device operated at the J_{SC} and the MPP showed a decrease of 30 % and 16 %, respectively. For the devices with CN, the J_{SC} only slightly reduced over time to 91 % of the initial J_{SC}. Similarly to the first stability test, the device with DMN operated at J_{SC} suffered a distinct decrease starting after approx. 200 h operation time, in the end, retaining 75 % of the starting value. Interestingly, for all device types, the same trend with respect to the V_{OC} was monitored as compared to the first experiment. The overall trend observed for the PCE closely follows the results seen for the J_{SC}. Thereby, the majority of measured devices still exhibit a PCE of over 80 % of the initial values. As for the previous experiment, it is assumed here that due to damaged encapsulation, some of the devices were strongly aged.

To avoid further aging non-related to the operation, two more light-soaking experiments were performed, whereby, in this case, the more flexible DELO epoxy glue was used. In the course of this test, the influence of illumination intensity on the light-soaking stability of the devices was examined (see section 2.4). In **Figure 27** and **Figure 28**, the light-soaking stability of the devices operated at V_{OC}, J_{SC} and MPP under respective illumination of 1200 lux and 3000 lux are shown.

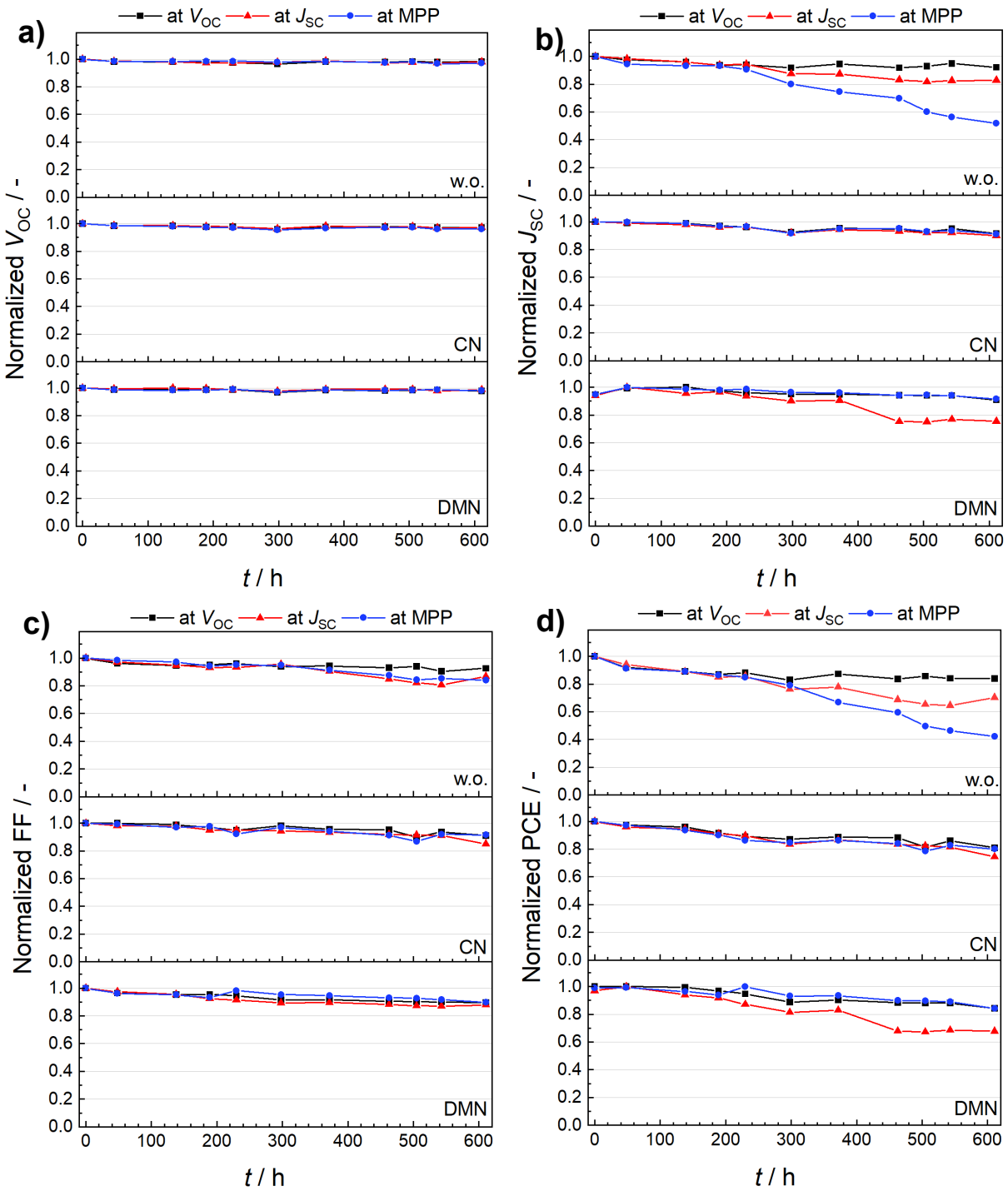

Figure 26. Comparison of the light-soaking stability over time (test 2) of devices with different solvent additives (w.o. additive, CN and DMN), operated (black: at V_{OC}, red: at J_{SC}, blue MPP) under an illumination intensity of 1200 lux in ambient atmosphere, whereby **a)** the normalized V_{OC}, **b)** normalized J_{SC}, **c)** normalized FF and **d)** normalized PCE are plotted as a function of time; for encapsulation the EMCAST epoxy glue was used.

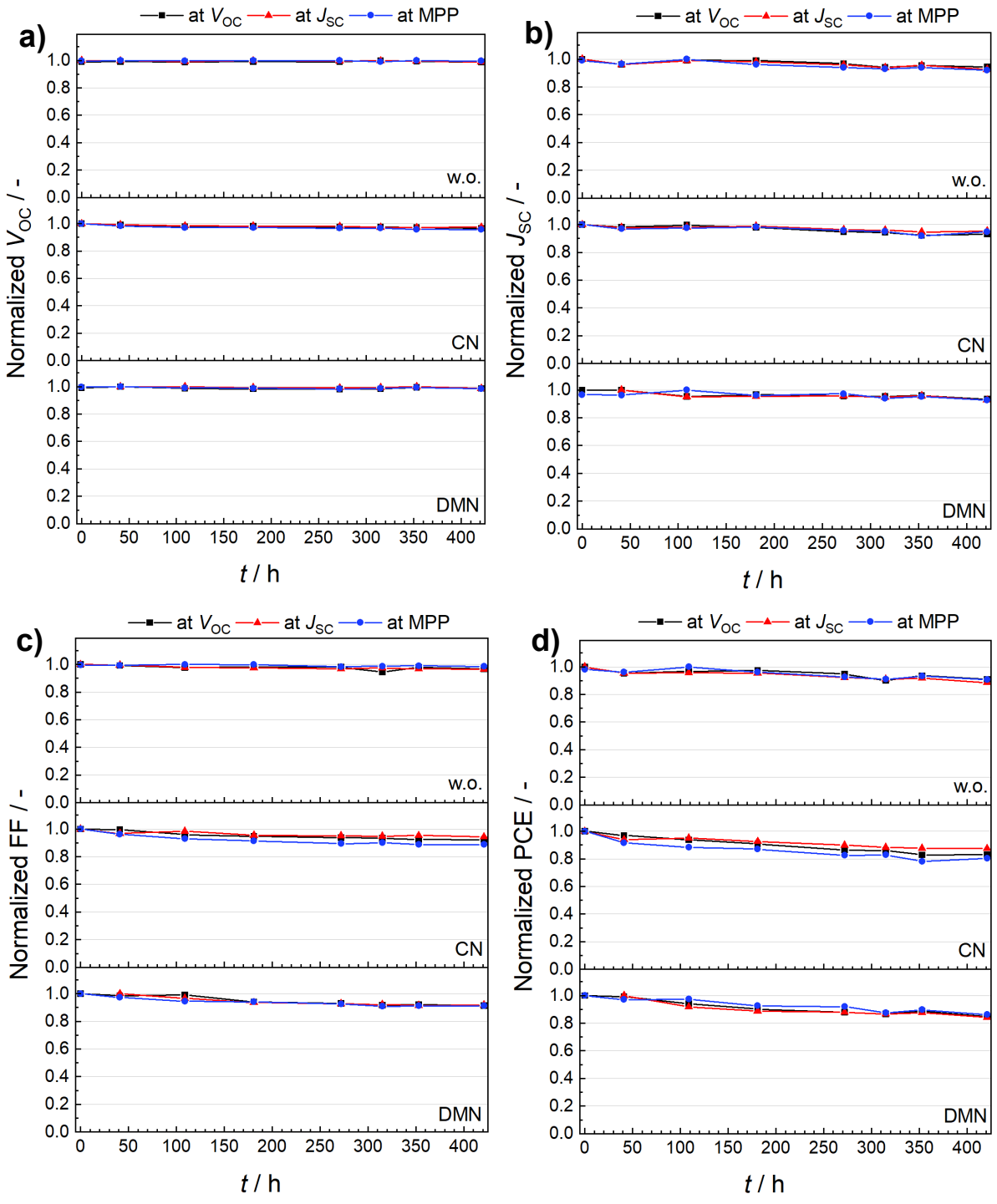

Figure 27. Comparison of the device stability over time (test 3) of devices with different solvent additives (w.o. additive, CN and DMN), operated (black: at V_{OC}, red: at J_{SC}, blue MPP) under an illumination intensity of 1200 lux in ambient atmosphere, whereby **a)** the normalized V_{OC}, **b)** normalized J_{SC}, **c)** normalized FF and **d)** normalized PCE are plotted as a function of time; for encapsulation the DELO epoxy glue was used.

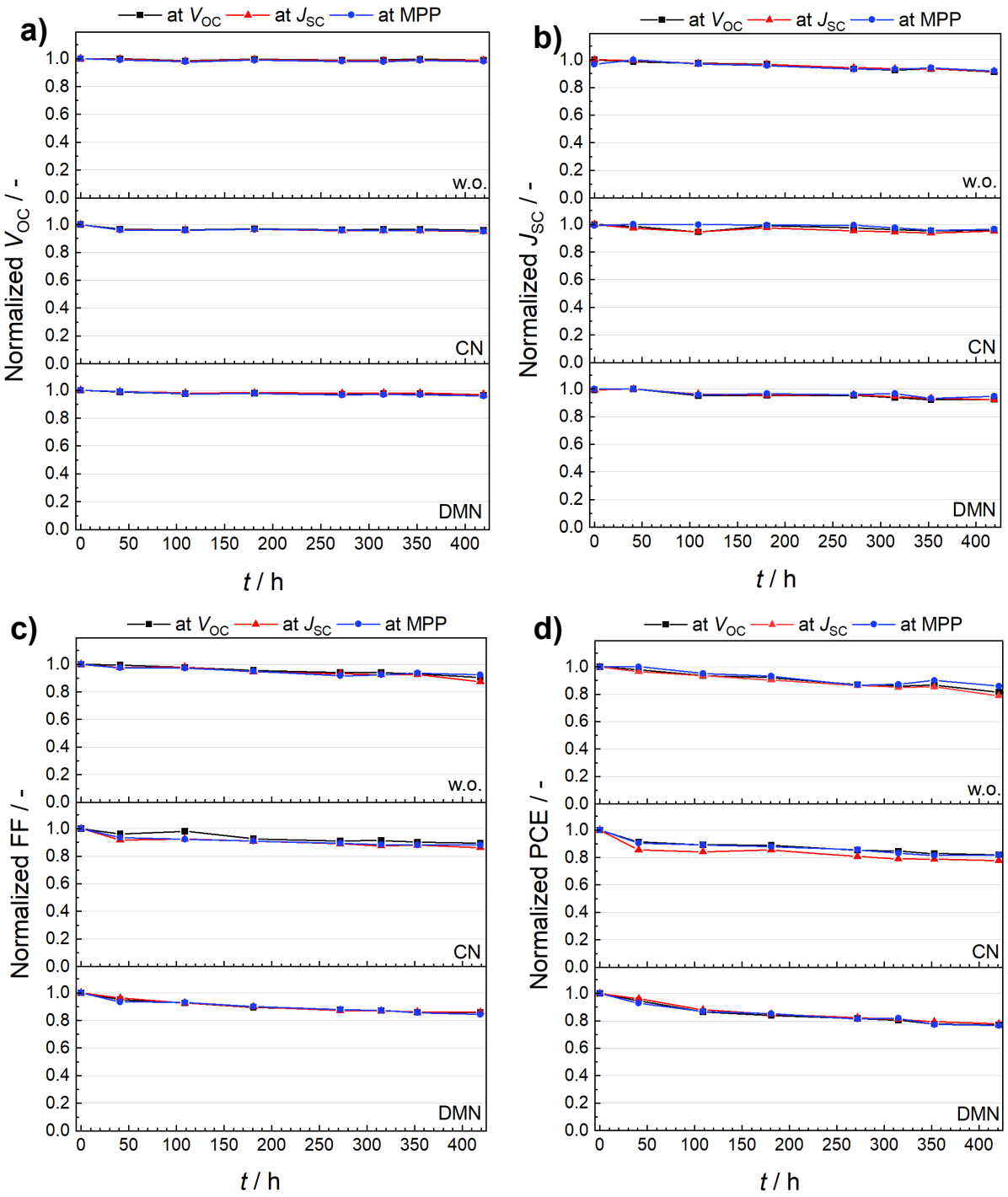

Figure 28. Comparison of the device stability over time (test 4) of devices with different solvent additives (w.o. additive, CN and DMN), operated (black: at V_{OC}, red: at J_{SC}, blue MPP) under an illumination intensity of 3000 lux in ambient atmosphere, whereby **a)** the normalized V_{OC}, **b)** normalized J_{SC}, **c)** normalized FF and **d)** normalized PCE are plotted as a function of time; for encapsulation the DELO epoxy glue was used.

Notably, in the third test, all monitored devices showed a similar behavior without distinct exceptions, as observed in the previous stability tests. This led to the assumption that the DELO glue provides a leak-free and enduring encapsulation, which is more suitable when working with crocodile clamps. When directly comparing the PCE over time for the three device types, the pristine device retained 91 %, the CN device approx. 83 % and the DMN-containing device 85 % of the initial PCE value. Referred to this, the functions of all respective FFs show similar trends for all devices. The V_{OC} and the J_{SC} do not fall below 93 % of the starting values. When considering these results, it is essential to note that the DMN-containing devices show notably higher PCE values compared to devices without additives, as described in section 3.2.2. Therefore, it is of particular interest that the solar cells still show a high performance despite being constantly operated under ambient conditions with room light illumination. To compare the starting and final PV performance of the tested devices, the respective data is listed in **Table 19**.

Table 19. Summary of the PV performance of the devices before and after illumination and operation at the MPP.

Intensity / *lux*	*Solvent additive*	V_{OC} / V	J_{SC} / mA cm^{-2}	$J_{SC,\,calc.}$* / mA cm^{-2}	FF / %	PCE / %
1200	w.o. (start)	0.72	19.7	19.0	57	8.0
	w.o. (end)	0.72	18.3	19.1	56	7.4
	0.5 % CN (start)	0.74	19.8	18.8	67	9.9
	0.5 % CN (end)	0.71	19.3	18.4	59	8.1
	0.5 % DMN (start)	0.75	22.4	20.5	65	10.9
	0.5 % DMN (end)	0.74	21.5	20.2	59	9.4
3000	w.o. (start)	0.74	18.9	17.6	62	8.7
	w.o. (end)	0.72	18.0	17.3	57	7.4
	0.5 % CN (start)	0.74	21.1	19.4	66	10.4
	0.5 % CN (end)	0.71	20.0	18.8	59	8.4
	0.5 % DMN (start)	0.76	22.6	20.7	64	11.1
	0.5 % DMN (end)	0.73	21.4	20.2	54	8.5

* Calculated from the respective EQE curve (shown in **Figure 29** and **Figure 30**)

It can be seen from **Figure 28** that the change in light intensity (to 3000 lux) only has a negligible impact on the stability of the device. All three device types, namely without additive, with CN and with DMN, still show a good performance after an operation period of 420 h, while retaining on average 82, 81 and 77 % of the initial PCE value, respectively. This final PCE value corresponds to a decrease by a factor of 0.9, 0.98, and 0.91 concerning the stability test using the lower light intensity (1200 lux). In this respect, the devices with CN show remarkable

stability besides still showing PCE values of 8.1 % (operated at MPP), as shown in **Table 19**. The functions of the other characteristic device parameters match the observations observed for the related stability test with illumination at lower light intensity.

Additionally, as listed in **Table 19**, all devices operated at MPP experienced a reduction in PCE over time, as stated previously. Furthermore, all devices show a good correlation between the J_{SC} extracted from the *J-V* curve as well as the calculated value from the respective EQE curve, which can also be observed in **Figure 29** and **Figure 30**.

Considering all these results, CN and DMN as solvent additives not only strongly improve the device performance with respect to the pristine device type but also do not noticeably reduce the stability of the tested devices. Moreover, the usage of PM6:Y6 in *o*-xylene with DMN allows the preparation of a non-halogenated and highly efficient OSC with long operational stability under indoor light. The ambient processing conditions additionally favor the employment of this laboratory-scale OSC system in roll-to-roll production for commercialized applications.

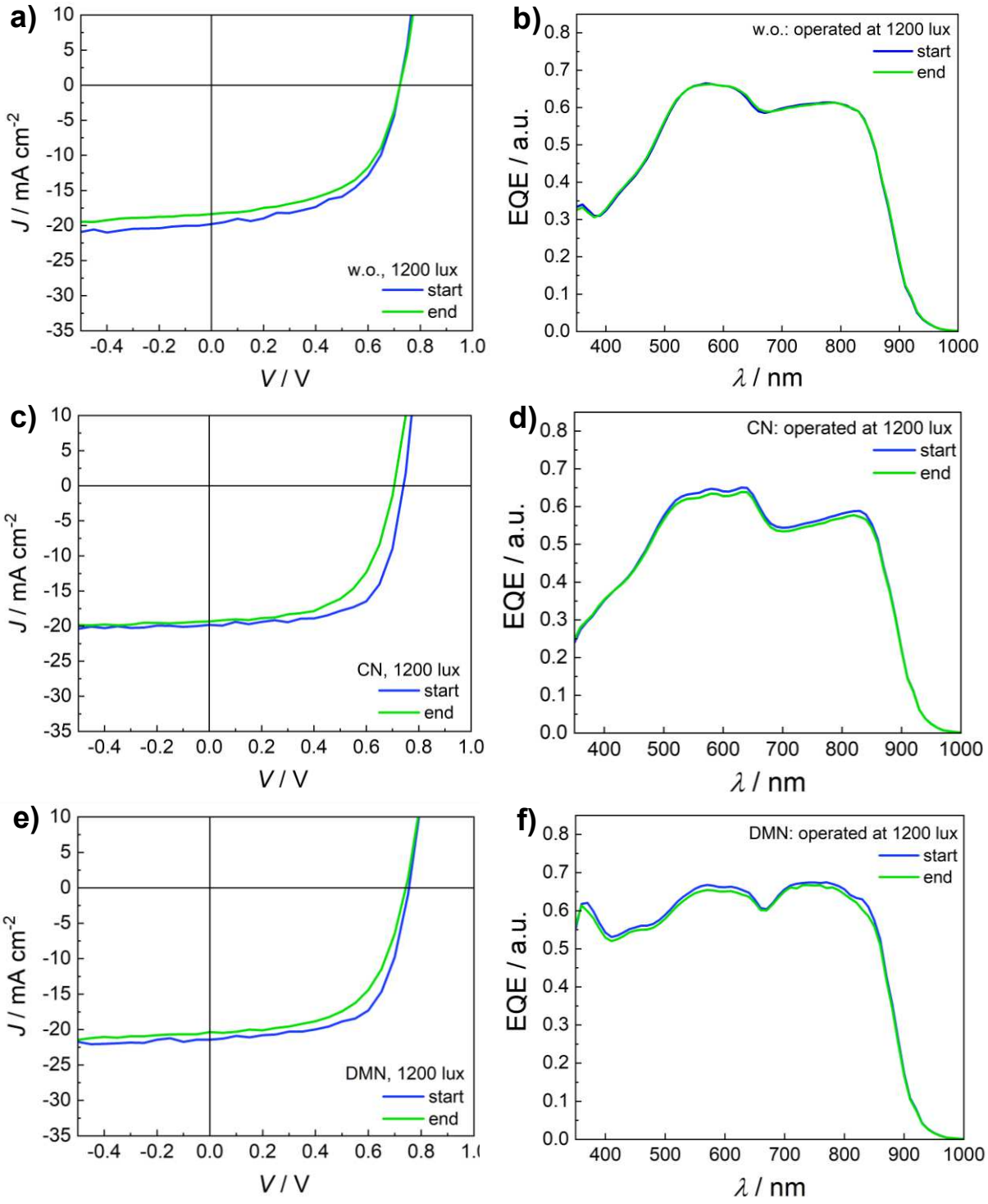

Figure 29. Comparison of the *J-V* curves and corresponding EQE curves of the devices operated at MPP under light illumination of 1200 lux. The *J-V* curves and EQE curves for the device without additive, with CN and with DMN are represented in **a)** and **b)**, **c)** and **d)**, as well as **e)** and **f)**, respectively.

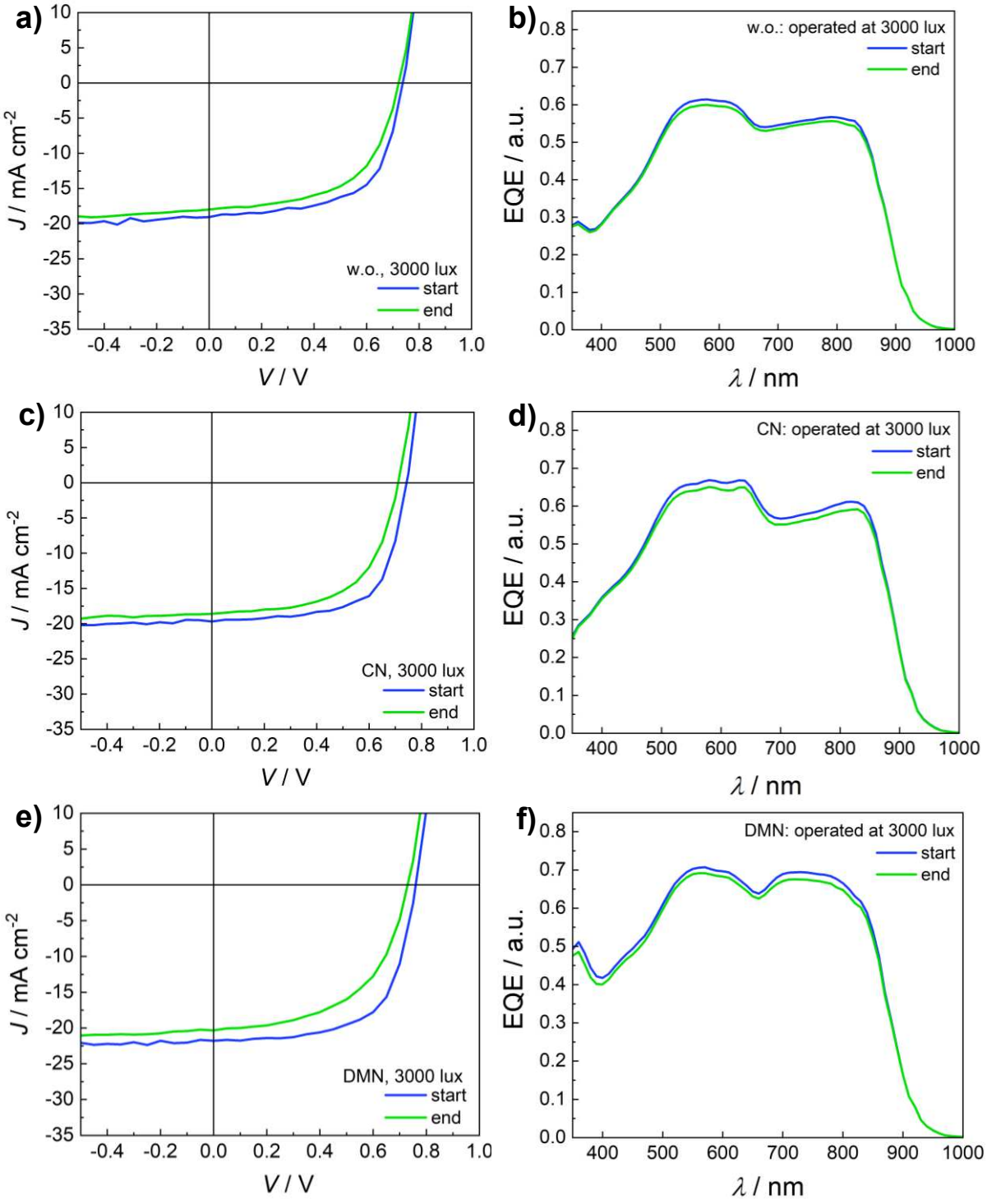

Figure 30. Comparison of the *J-V* curves and corresponding EQE curves of the devices operated at MPP under light illumination of 3000 lux. The *J-V* curves and EQE curves for the device without additive, with CN and with DMN are represented in **a)** and **b)**, **c)** and **d)**, as well as **e)** and **f)**, respectively.

3.3.4 Low-Light Intensity Power Output

Since thin film OPV materials characteristically show high exciton binding energies as well as short-distance diffusion (L_D) [64], typical thicknesses in the range of 60 - 100 nm are applied to guarantee high efficiency in charge carrier diffusion and transport [13,75]. However, the optical attenuation length of organic OPV materials is much larger than the width of the absorber layer, leading to a high amount of unabsorbed photons [13,74,116]. This especially presents a problem when talking about the application of OPVs for indoor light-harvesting, where low irradiance light intensities of ca. 1200 lux are common [64,117,118]. In this sense, adjusting the photoactive material in OSCs to a given indoor light source is crucial for achieving an optimized overlap in absorption and irradiance spectra, which would allow effective photocurrent generation [119,120]. The choice of photoactive material, as well as the device configuration, influence the behavior of the device performance upon different illumination light intensities [64]. Ma *et al.* [120] have reportedly used PM6:Y6-O for indoor OSCs, which showed a high efficiency of over 30 % measured at low light intensities.

Although in this work, the focus of research lies on the device performance of the prepared thin film OSCs at 1 sun (with AM1.5G), it would still be interesting to examine the power output of already operated devices at a lower light intensity. In this respect, the low-light intensity power output of PM6:Y6 devices after operation under the illumination of indoor light sources is of particular interest since it has not been published before. Therefore, the performance of devices was measured after 500 h of operation at the MPP with 1200 lux (see **Figure 31**), as described in section 2.4. From this performance data, the maximum power P_{max} was calculated

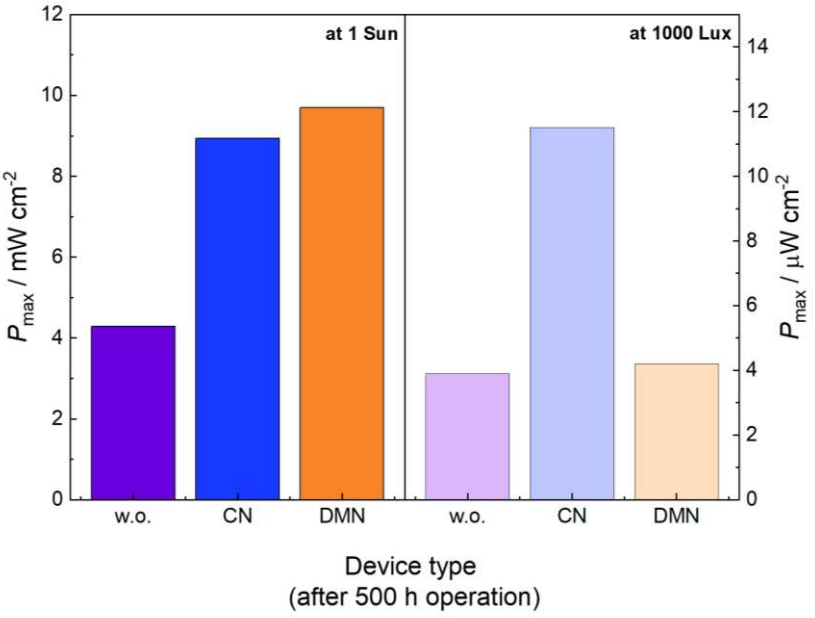

Figure 31. P_{max} of different device types (without additive, with CN and with DMN) measured at 1 sun and at 1000 lux.

and compared to the respective P_{max} value obtained at 1 sun with AM1.5G conditions in **Figure 31**. Additionally, the corresponding device performance is shown in **Table 20**.

Table 20. Summary of the PV performance of the devices with different solvent additives measured at varied light intensities.

Solvent additive	Intensity / lux	V_{OC} / V	J_{SC} / µA cm^{-2}	FF / %	P_{max} / µW cm^{-2}
w.o.	1000	0.17	70	33	3.9
	90000[2)]	0.72	13.0[3)]	46	4.29[4)]
CN	1000	0.29	120	33	11.5
	90000[2)]	0.74	21.2[3)]	57	8.94[4)]
DMN	1000	0.20	70	30	4.2
	90000[2)]	0.75	21.8[3)]	59	9.70[4)]
Silicon[1)] (Si)	1000	0.25	108	54.9	14.3
	10000	0.45	1.056[3)]	59.2	283.6

[1)] Reference data of a standard silicon solar cell measured under a white LED light (CCT 5600 K) taken from Dayneko *et al.* [66]
[2)] Light intensity measured with a lux meter for 100 mW cm^{-2} (solar simulator) by Park *et al.* [64]
[3)] The unit of J_{SC} is mA cm^{-2} (for measurement at a light intensity of 100 mW cm^{-2})
[4)] The unit of P_{max} is mW cm^{-2} (for measurement at a light intensity of 100 mW cm^{-2})

In **Figure 31**, the P_{max} measured at 1 sun and 1000 lux is illustrated for the three devices that were operated at MPP over a period of 500 h. Interestingly, the device with CN showed 11.5 µW cm^{-2}, a much higher P_{max} at 1000 lux than the other devices, whereby at 1 sun, the DMN device exhibits the highest value with 9.7 mW cm^{-2}. In comparison to that, a standard reference silicon solar cell exhibits with 14.3 µW cm^{-2} a comparable power output as the devices containing additives, as visible in **Table 20**. In literature, BHJ PM6-IDIC devices reportedly exhibit P_{max} values of 9.49 mW cm^{-2} and 50.5 µW cm^{-2} measured at 1 sun and 1000 lux (with a white LED), respectively [64]. This P_{max} literature value at 1000 lux is nearly 5 times larger than the highest value observed in this experiment. It is important to note that in this literature, a conventional device configuration with different interlayers (ITO/PEDOT:PSS/PM6:IDIC/ZnO nanoparticles/Ag) was used, which shows different characteristic performance parameters than the configuration used in this work. Furthermore, in literature, semi-transparent devices with a similar structure (ITO/ZnO/PM6:Y6:$PC_{71}BM$/MoO_x/Ag/ITO) compared to this work, exhibit a P_{max} of 15.1 µW cm^{-2} at 1200 lux [118]. This result correlates with the maximum power output found for all three device types at 1000 lux, as seen in **Table 20.** The origin of this similarity of the low P_{max} values might be traced back to the so-called light-soaking effect known to be characteristic of the used ETL layer ZnO [27,65,121–123]. Upon illumination with UV light, the width of the energy barrier between ZnO and the ITO layer is decreased, which leads to a better charge carrier

collection at the ITO electrode [121]. Consequently, the device performance, including the FF, is noticeably improved [121]. As in this experiment, an ordinary table lamp was used for illumination, and these light sources typically lack UV light, the strong reduction of the FF as well as the P_{max} can be explained [65]. To overcome this soaking effect, different strategies have been reported for instance introducing salts like cesium carbonate (Cs_2CO_3), tin(II) chloride ($SnCl_2$), or indium(III) chloride ($InCl_3$) into ZnO [122,124]. Further effective dopants include lithium fluoride (LiF) [28] or Al [27].

To conclude, the prepared devices not only showed high light-soaking stability over a period of up to 750 h but also the device performance parameters of the operated and aged OSCs are similarly high at low light intensity as compared to a standard silicon solar cell as well as literature OSCs systems. This suggests that these devices show great potential for indoor light-harvesting applications such as low-power electronic devices.

4 Conclusion and Outlook

Essential for the commercialization of OSCs for applications, e.g. in the field of indoor light harvesting and small electronics, is the dual presence of a highly efficient device performance as well as long-term operational stability under indoor illumination. In this thesis, the goal was to find a fabrication process that allows to produce highly efficient OSC using the novel PM6:Y6 system and to satisfy the requirements for a potential scale-up for industrial use including ambient processing conditions and the usage of a green non-halogenated solvent for the D/A blend mixture. With the best-performing devices the light-soaking stability was then investigated for its potential in commercial applications. It has been shown that the most promising devices were fabricated by blade-coating the photoactive layer at 80 °C followed by thermal annealing at 130 °C for 5 minutes. To obtain these results, the ink solution was prepared with PM6:Y6 in a 1:1.2 weight ratio dissolved in *o*-xylene as a solvent with CN or DMN as solvent additives. For the prepared devices, a PCE of up to 11.3 % and 13.5 % could be achieved with the addition of CN and DMN, respectively. By encapsulating the devices either with the epoxy sealant EMCAST or DELO, the device performances could be successfully retained under inert and ambient conditions. Additionally, upon 420 h of operation at the J_{SC}, V_{OC} and the MPP under the illumination of typical indoor light with an intensity of 1200 lux, the devices, respectively using CN and DMN, still showed remarkable stability by retaining on average 83 % and 85 % of their initial PCE. This high light-soaking stability could be again proved by increasing the illumination light intensity to 3000 lux, whereby the devices with CN and DMN exhibited PCE values corresponding to 81 % and 77 % of their initial PCE. The operation-related decrease in device performance parameters extracted from the *J-V* curves was in accordance with the data provided by the corresponding EQE curves. Notably, when measuring the maximum power at indoor light (1000 lux) for already operated devices (500 h at 1200 lux), values of 11.5 and 4.2 μW cm^{-2} could be obtained for CN and DMN-containing devices, respectively. This power output is comparable to values obtained for a standard Si cell and unoperated similarly structured OSCs from literature.

An essential limitation within the study of the light-soaking stability was the manual handling of the devices with crocodile clips, which could have primarily contributed to a decrease in device performance over time. It is therefore suggested to operate the OSCs using a different approach, such as wires attached to the contacts *via* a suitable conductive Ag epoxy sealant. Furthermore, it would be highly recommended to investigate the power output of operated devices using, for instance, a halogen lamp to avoid the lack of UV light, which is not only responsible for the light-soaking effect within ZnO but also is improving the device performance.

All in all, the chosen fabrication process has fulfilled the posed requirements for a large-scale implementation of the OSC system. Additionally, the prepared OSCs showed both excellent device performance and high light-soaking stability under indoor conditions, especially when using the environmentally favored non-halogenated additive DMN. These results present the great capability of this OSC system to be applied in small electronic devices included in the IoT.

A Appendix

Table 21. Other instruments used in this work.

Instrument	Name and Supplier	Settings
Plasma Cleaner	PE-25 – Plasma Etch Inc.	equipped with a JB Industries Inc. DV-142N - Platinum 5 CFM vacuum pump, used with O_2 gas, at 100 W for 5 min
Ultrasonic bath	VWR Ultrasonic Cleaner	-

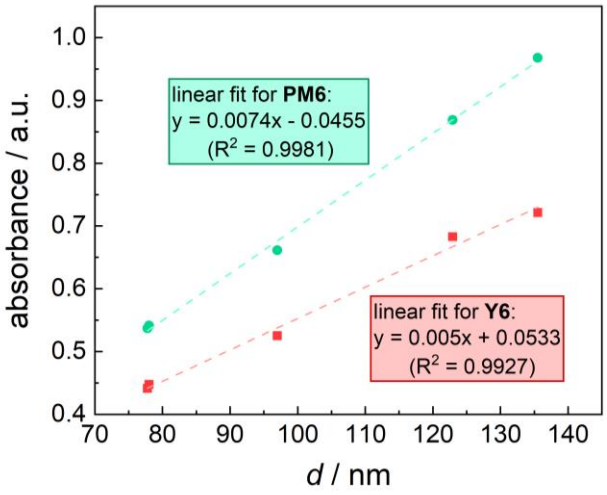

Figure 32. Linear fits for the peak absorbance of PM6 ($\lambda_{max} \approx 630$ nm) and Y6 ($\lambda_{max} \approx 830$ nm) plotted against the corresponding photoactive layer thickness of the measured films.

A.1 List of Symbols and Abbreviations

List of Symbols

β	Mass concentration
λ	Photon wavelength
v	Frequency
$\Phi_{\text{light source}}$	Photon flux of the light source
$c = 2.998 \times 10^{8}$ m s^{-1}	Speed of light in vacuum
d	Layer thickness
E_g	Band gap energy
$h = 6.626 \times 10^{-34}$ m^2 kg s^{-1}	Planck constant
I	Current
I_{SC}	Short-circuit current
J	Current density
J_{SC}	Short circuit current density
$J_{SC,calc.}$	Short circuit current density calculated from the measured EQE
L_D	Diffusion length
n	Number of devices included in the statistics
$S_{AM1.5G}$	Solar spectral irradiance at AM15.G conditions
P_{max}	Maximum power
q	Elementary charge
T	Temperature
t	Time
V	Voltage
V_{OC}	Open-circuit voltage

List of Symbols

A	Acceptor of a bulk heterojunction organic solar cell
Ag	Silver
BHJ	Bulk heterojunction
C	Carbon
$CHCl_3$	Chloroform
CN	1-Chloronaphthalene
CO_2	Carbon dioxide
Cs_2CO_3	Cesium carbonate
D	Donor of a bulk heterojunction organic solar cell
DMN	1,2-Dimethylnaphthalene
ETL	Electron transport layer
EQE	External quantum efficiency
FF	Fill factor
FA	Fullerene acceptor
H_2O	Water
HOMO	Highest occupied molecular orbital

HTL	Hole transport layer
$InCl_3$	Indium(III) chloride
IoT	Internet of Things
ITO	Indium tin oxide
LED	Light-emitting diode
LiF	Lithium fluoride
LUMO	Lowest unoccupied molecular orbital
MoO_x	Molybdenum oxide
MPP	Maximum power point
N2200	Poly{[*N,N′*-bis(2-octyldodecyl)-naphthalene-1,4,5,8-bis(dicarboximide)-2,6-diyl]-*alt*-5,5′-(2,2′-bithiophene)
NFA	Non-fullerene acceptor
O_2	Oxygen
OPVs	Organic photovoltaics
OSC	Organic solar cell
$PC_{71}BM$	(6,6)-Phenyl C71 butyric acid methyl ester
PCE	Power conversion efficiency
PEDOT	Poly(3,4-ethylene dioxythiophene)
PM6	Poly[(2,6-(4,8-bis(5-(2-ethylhexyl-3-fluoro)thiophen-2-yl)-benzo[1,2-b:4,5-b']dithiophene))-alt-(5,5-(1',3'-di-2-thienyl-5',7'-bis(2-ethylhexyl)benzo[1',2'-c:4',5'-c']dithiophene-4,8-dione))]
i-Prop	2-Propanol
PSS	Polystyrene sulfonate
PTQ10	Poly[[6,7-difluoro[(2-hexyldecyl)oxy]-5,8-quinoxalinediyl]-2,5-thiophenediyl]
PV	Photovoltaic
PVC	Polyvinyl chloride
rpm	Revolutions per minute
Si	Silicon
SnCl	Tin(II) chloride
SnO_2	Tin(II) oxide
TCO	Transparent conductive oxides
w.o.	Without additive
Y6	2,2'-((2Z,2'Z)-((12,13-bis(2-ethylhexyl)-3,9-diundecyl-12,13-dihydro-[1,2,5]thiadiazolo[3,4-e]thieno[2",3":4',5'] thieno[2',3':4,5]pyrrolo[3,2-g]thieno[2',3':4,5]thieno[3,2-b]indole 2,10-diyl) bis(methanylylidene))bi
ZnO	Zinc oxide

A.2 List of Figures

A.3 List of Tables

References

[1] L. Duan, A. Uddin, *Adv. Sci. (Weinheim, Ger.)* **2020**, *7*, 1903259.

[2] M. Riede, D. Spoltore, K. Leo, *Adv. Energy Mater.* **2021**, *11*.

[3] Hannah Ritchie, Max Roser, Pablo Rosado, *Our World in Data* **2022**.

[4] M. Hiramoto, S. Izawa (Eds.) *Organic solar cells*. *Energetic and nanostructural design*, Springer, Singapore, **2021**.

[5] G. Masson, E. Bosch, I. Kaizuka, A. Jäger-Waldau, J. Donoso, *Snapshot of Global PV Markets 2022 Task 1 Strategic PV Analysis and Outreach PVPS*, **2022**.

[6] Z. Hu, J. Wang, X. Ma, J. Gao, C. Xu, K. Yang, Z. Wang, J. Zhang, F. Zhang, *Nano Energy* **2020**, *78*, 105376.

[7] M. Kaltenbrunner, M. S. White, E. D. Głowacki, T. Sekitani, T. Someya, N. S. Sariciftci, S. Bauer, *Nat. Commun.* **2012**, *3*, 770.

[8] C. J. Brabec, N. S. Sariciftci, J. C. Hummelen, *Adv. Funct. Mater.* **2001**, *11*, 15.

[9] M. A. Alkhalayfeh, A. Abdul Aziz, M. Z. Pakhuruddin, K. M. M. Katubi, N. Ahmadi, *Phys. Status Solidi A* **2022**, *219*.

[10] R. Yu, G. Wu, Z. Tan, *J. Energy Chem.* **2021**, *61*, 29.

[11] S.-Y. Chang, P. Cheng, G. Li, Y. Yang, *Joule* **2018**, *2*, 1039.

[12] G. C. Mishra (Ed.) *Energy technology & ecological concerns*. *A contemporary approach*, Gyan Bindu Publications, New Delhi, **2014**.

[13] Yan-Gang Bi, Jing Feng, Jin-Hai Ji, Fang-Shun Yi, Yun-Fei Li, Yue-Feng Liu, Xu-Lin Zhang, Hong-Bo Sun, *Nanophotonics* **2018**, *7*, 371.

[14] M. C. Scharber, N. S. Sariciftci, *Prog. Polym. Sci.* **2013**, *38*, 1929.

[15] Y. Sun, J. H. Seo, C. J. Takacs, J. Seifter, A. J. Heeger, *Adv. Mater.* **2011**, *23*, 1679.

[16] E. N. Güler, A. Distler, R. Basu, C. J. Brabec, H.-J. Egelhaaf, *Flex. Print. Electron.* **2022**, *7*, 25003.

[17] X. Wan, G. Long, L. Huang, Y. Chen, *Adv. Mater.* **2011**, *23*, 5342.

[18] F. Hermerschmidt, A. Savva, E. Georgiou, S. M. Tuladhar, J. R. Durrant, I. McCulloch, D. D. C. Bradley, C. J. Brabec, J. Nelson, S. A. Choulis, *ACS Appl. Mater. Interfaces* **2017**, *9*, 14136.

[19] P. Qin, Q. He, D. Ouyang, G. Fang, W. C. H. Choy, G. Li, *Sci. China: Chem.* **2017**, *60*, 472.

[20] Y. Shirota, H. Kageyama in *Handbook of Organic Materials for Optical and (Opto)electronic Devices*, Elsevier, **2013**, pp. 3–82.

[21] V. D. Patel, D. Gupta, *Mater. Today Commun.* **2022**, *31*, 103664.

[22] Y.-J. Su, H. Nie, C.-F. Chang, S.-C. Huang, Y.-H. Huang, T.-W. Chen, K.-K. Hsu, T.-Y. Lee, H.-M. Shih, C.-W. Ko et al., *ACS Appl. Mater. Interfaces* **2021**, *13*, 59043.

[23] M. R. Niazi, H. Zhao, R. M. Lamarche, R. Munir, S. Trudel, J. Hu, G. C. Welch, *Adv. Mater. Interfaces* **2022**, *9*.

[24] F. Zhang, X. Xu, W. Tang, J. Zhang, Z. Zhuo, J. Wang, J. Wang, Z. Xu, Y. Wang, *Sol. Energy Mater. Sol. Cells* **2011**, *95*, 1785.

[25] a) T. Yang, W. Cai, D. Qin, E. Wang, L. Lan, X. Gong, J. Peng, Y. Cao, *J. Phys. Chem. C* **2010**, *114*, 6849; b) Y. Long, *Sol. Energy Mater. Sol. Cells* **2010**, *94*, 744.

[26] M. Prosa, M. Tessarolo, M. Bolognesi, O. Margeat, D. Gedefaw, M. Gaceur, C. Videlot-Ackermann, M. R. Andersson, M. Muccini, M. Seri et al., *ACS Appl. Mater. Interfaces* **2016**, *8*, 1635.

[27] Z. Jiang, S. Soltanian, B. Gholamkhass, A. Aljaafari, P. Servati, *RSC Adv* **2018**, *8*, 36542.

[28] M. Thambidurai, J. Y. Kim, H. Song, Y. Ko, N. Muthukumarasamy, D. Velauthapillai, V. W. Bergmann, S. A. L. Weber, C. Lee, *J. Mater. Chem. A* **2014**, *2*, 11426.

[29] Y. Tong, Z. Xiao, X. Du, C. Zuo, Y. Li, M. Lv, Y. Yuan, C. Yi, F. Hao, Y. Hua et al., *Sci. China: Chem.* **2020**, *63*, 758.

[30] A. J. Heeger, *J. Phys. Chem. B* **2001**, *105*, 8475.

[31] W. Brütting in *Physics of Organic Semiconductors* (Ed.: W. Brütting), Wiley, **2005**, pp. 1–14.

[32] H. Hoppe, N. S. Sariciftci, *J. Mater. Res.* **2004**, *19*, 1924.

[33] F. Nickel, *Herstellung und Charakterisierung mechanisch flexibler organischer Solarzellen durch Flüssigprozessierung*, KIT Scientific Publishing, **2014**.

[34] a) S. Babu Krishna Moorthy (Ed.) *Thin Film Structures in Energy Applications*, Springer International Publishing, Cham, **2015**; b) N. S. Sariciftci, D. Braun, C. Zhang, V. I. Srdanov, A. J. Heeger, G. Stucky, F. Wudl, *Appl. Phys. Lett.* **1993**, *62*, 585.

[35] G. Yu, J. Gao, J. C. Hummelen, F. Wudl, A. J. Heeger, *Science* **1995**, *270*, 1789.

[36] A. Dey, A. Singh, D. Das, P. K. Iyer in *Thin Film Structures in Energy Applications* (Ed.: S. Babu Krishna Moorthy), Springer International Publishing, Cham, **2015**, pp. 97–128.

[37] N. S. Sariciftci, L. Smilowitz, A. J. Heeger, F. Wudl, *Science* **1992**, *258*, 1474.

[38] C. Putz, *Master Thesis*, Johannes Kepler University Linz, Linz, **2021**.

[39] C. J. Schaffer, C. M. Palumbiny, M. A. Niedermeier, C. Burger, G. Santoro, S. V. Roth, P. Müller-Buschbaum, *Adv. Energy Mater.* **2016**, *6*.

[40] D. Neusser, B. Sun, W. L. Tan, L. Thomsen, T. Schultz, L. Perdigón-Toro, N. Koch, S. Shoaee, C. R. McNeill, D. Neher et al., *J. Mater. Chem. C* **2022**, *10*, 11565.

[41] Q. Guo, Q. Guo, Y. Geng, A. Tang, M. Zhang, M. Du, X. Sun, E. Zhou, *Mater. Chem. Front.* **2021**, *5*, 3257.

[42] W. Zhao, S. Zhang, J. Hou, *Sci. China: Chem.* **2016**, *59*, 1574.

[43] Y. Lin, X. Zhan, *Mater. Horiz.* **2014**, *1*, 470.

[44] Z.-C. Wen, H. Yin, X.-T. Hao, *Surf. Interfaces* **2021**, *23*, 100921.

[45] J. Cao, L. Yi, L. Zhang, Y. Zou, L. Ding, *J. Mater. Chem. A* **2022**, *11*, 17.

[46] L. Perdigón-Toro, H. Zhang, A. Markina, J. Yuan, S. M. Hosseini, C. M. Wolff, G. Zuo, M. Stolterfoht, Y. Zou, F. Gao et al., *Adv. Mater.* **2020**, *32*, e1906763.

[47] Y. Cui, H. Yao, J. Zhang, T. Zhang, Y. Wang, L. Hong, K. Xian, B. Xu, S. Zhang, J. Peng et al., *Nat. Commun.* **2019**, *10*, 2515.

[48] J. Yuan, Y. Zhang, L. Zhou, G. Zhang, H.-L. Yip, T.-K. Lau, X. Lu, C. Zhu, H. Peng, P. A. Johnson et al., *Joule* **2019**, *3*, 1140.

[49] J. Cao, L. Yi, L. Ding, *J. Semicond.* **2022**, *43*, 30202.

[50] X. Xu, L. Yu, H. Yan, R. Li, Q. Peng, *Energy Environ. Sci.* **2020**, *13*, 4381.

[51] Y.-Y. Yu, K.-Y. Shih, Y.-C. Peng, Y.-C. Chiu, C.-C. Kuo, C.-C. Yang, C.-P. Chen, *Mater. Chem. Phys.* **2022**, *282*, 125971.

[52] H. Zhao, H. B. Naveed, B. Lin, X. Zhou, J. Yuan, K. Zhou, H. Wu, R. Guo, M. A. Scheel, A. Chumakov et al., *Adv. Mater.* **2020**, *32*, e2002302.

[53] C. McDowell, G. C. Bazan, *Curr. Opin. Green Sustainable Chem.* **2017**, *5*, 49.

[54] C. McDowell, M. Abdelsamie, M. F. Toney, G. C. Bazan, *Adv. Mater.* **2018**, e1707114.

[55] X. Gu, Y. Zhou, K. Gu, T. Kurosawa, Y. Guo, Y. Li, H. Lin, B. C. Schroeder, H. Yan, F. Molina-Lopez et al., *Adv. Energy Mater.* **2017**, *7*.

[56] H. Hu, P. C. Y. Chow, G. Zhang, T. Ma, J. Liu, G. Yang, H. Yan, *Acc. Chem. Res.* **2017**, *50*, 2519.

[57] Y.-F. Ma, Y. Zhang, H.-L. Zhang, *J. Mater. Chem. C* **2022**, *10*, 2364.

[58] X. He, C. C. S. Chan, J. Kim, H. Liu, C.-J. Su, U.-S. Jeng, H. Su, X. Lu, K. S. Wong, W. C. H. Choy, *Small methods* **2022**, *6*, e2101475.

[59] H. Fan, H. Yang, Y. Wu, O. Yildiz, X. Zhu, T. Marszalek, P. W. Blom, C. Cui, Y. Li, *Adv. Funct. Mater.* **2021**, *31*.

[60] M. Hösel, H. F. Dam, F. C. Krebs, *Energy Technol.* **2015**, *3*, 293.

[61] Y.-H. Chang, S.-R. Tseng, C.-Y. Chen, H.-F. Meng, E.-C. Chen, S.-F. Horng, C.-S. Hsu, *Org. Electron.* **2009**, *10*, 741.

[62] G. Burwell, O. J. Sandberg, W. Li, P. Meredith, M. Carnie, A. Armin, *Sol. RRL* **2022**, *6*.

[63] I. Mathews, S. N. Kantareddy, T. Buonassisi, I. M. Peters, *Joule* **2019**, *3*, 1415.

[64] S. Y. Park, C. Labanti, J. Luke, Y.-C. Chin, J.-S. Kim, *Adv. Energy Mater.* **2022**, *12*.

[65] M. Mainville, M. Leclerc, *ACS Energy Lett.* **2020**, *5*, 1186.

[66] S. V. Dayneko, M. Pahlevani, G. C. Welch, *ACS Appl. Mater. Interfaces* **2019**, *11*, 46017.

[67] Y. Zhang, C. Duan, L. Ding, *Sci. Bull.* **2020**, *65*, 2040.

[68] L. Xiao, X. Wu, G. Ren, M. A. Kolaczkowski, G. Huang, W. Tan, L. Ma, Y. Liu, X. Peng, Y. Min et al., *Adv. Funct. Mater.* **2021**, *31*.

[69] R. Ma, T. Liu, Z. Luo, Q. Guo, Y. Xiao, Y. Chen, X. Li, S. Luo, X. Lu, M. Zhang et al., *Sci. China: Chem.* **2020**, *63*, 325.

[70] C.-H. Hsu, X.-Y. Zhang, H.-J. Lin, S.-Y. Lien, Y.-S. Cho, C.-S. Ye, *Energies* **2019**, *12*, 2541.

[71] A. Presciutti, F. Asdrubali, A. Marrocchi, A. Broggi, G. Pizzoli, A. Damiani, *Sustainability* **2014**, *6*, 6830.

[72] T. P. A. van der Pol, B. T. van Gorkom, W. F. M. van Geel, J. Littmann, M. M. Wienk, R. A. J. Janssen, *Adv. Energy Mater.* **2023**, *13*.

[73] J. Peet, L. Wen, P. Byrne, S. Rodman, K. Forberich, Y. Shao, N. Drolet, R. Gaudiana, G. Dennler, D. Waller, *Appl. Phys. Lett.* **2011**, *98*.

[74] S. Liu, S. Lin, P. You, C. Surya, S. P. Lau, F. Yan, *Angew. Chem., Int. Ed. Engl.* **2017**, *56*, 13717.

[75] L. Chen, W. E. I. Sha, W. C. H. Choy, *Opt. Express* **2012**, *20*, 8175.

[76] G. Dennler, M. C. Scharber, C. J. Brabec, *Adv. Mater.* **2009**, *21*, 1323.

[77] G. L. Schulz, M. Löbert, I. Ata, M. Urdanpilleta, M. Lindén, A. Mishra, P. Bäuerle, *J. Mater. Chem. A* **2015**, *3*, 13738.

[78] H. Chen, K. Ding, L. Fan, W. Liu, R. Zhang, S. Xiang, Q. Zhang, L. Wang, *ACS Appl. Mater. Interfaces* **2018**, *10*, 29076.

[79] Di Wang, G. Zhou, Y. Li, K. Yan, L. Zhan, H. Zhu, X. Lu, H. Chen, C.-Z. Li, *Adv. Funct. Mater.* **2022**, *32*.

[80] S. R. Amrutha, M. Jayakannan, *J. Phys. Chem. B* **2008**, *112*, 1119.

[81] G. Zhou, M. Zhang, J. Xu, Y. Yang, T. Hao, L. Zhu, L. Zhou, H. Zhu, Y. Zou, G. Wei et al., *Energy Environ. Sci.* **2022**, *15*, 3483.

[82] J. Yang, X. Wang, X. Yu, J. Liu, Z. Zhang, J. Zhong, *Coatings* **2023**, *13*, 1561.

[83] B. Ray, P. R. Nair, M. A. Alam, *Sol. Energy Mater. Sol. Cells* **2011**, *95*, 3287.

[84] R. Wang, C. Zhang, Q. Li, Z. Zhang, X. Wang, M. Xiao, *J. Am. Chem. Soc.* **2020**, *142*, 12751.

[85] S. Bao, H. Yang, H. Fan, J. Zhang, Z. Wei, C. Cui, Y. Li, *Adv. Mater.* **2021**, *33*, e2105301.

[86] R. Basu, K. S. Siah, A. Distler, F. Häußler, J. Franke, C. J. Brabec, H.-J. Egelhaaf, *Adv. Eng. Mater.* **2023**, *25*.

[87] M. Shaban, M. Benghanem, A. Almohammedi, M. Rabia, *Coatings* **2021**, *11*, 863.

[88] M. Fernández-Castro, J. Truer, M. Espindola-Rodriguez, J. W. Andreasen, *Front. Nanotechnol.* **2022**, *4*.

[89] P. Cheng, R. Wang, J. Zhu, W. Huang, S.-Y. Chang, L. Meng, P. Sun, H.-W. Cheng, M. Qin, C. Zhu et al., *Adv. Mater.* **2018**, *30*.

[90] H.-W. Cheng, C.-Y. Juan, A. Mohapatra, C.-H. Chen, Y.-C. Lin, B. Chang, P. Cheng, H.-C. Wang, C. W. Chu, Y. Yang et al., *Nano Lett.* **2021**, *21*, 2207.

[91] D. Li, L. Zhu, X. Liu, W. Xiao, J. Yang, R. Ma, L. Ding, F. Liu, C. Duan, M. Fahlman et al., *Adv. Mater.* **2020**, *32*, e2002344.

[92] S. Dong, K. Zhang, T. Jia, W. Zhong, X. Wang, F. Huang, Y. Cao, *EcoMat* **2019**, *1*.

[93] M. Deng, H. Meng, X. Xu, J. Tang, L. Yu, R. Li, Q. Peng, *Chem. Eng. J.* **2022**, *440*, 135975.

[94] Y. Xu, J. Yuan, S. Zhou, M. Seifrid, L. Ying, B. Li, F. Huang, G. C. Bazan, W. Ma, *Adv. Funct. Mater.* **2019**, *29*.

[95] T. Kobori, T. Fukuda, *Org. Electron.* **2017**, *51*, 76.

[96] A. Rani, K. A. Mohamad, B. K. Ghosh, I. Saad, P. Ibrahim, A. Alias, A. B. Abd Rahman in *5th IET International Conference on Clean Energy and Technology (CEAT2018)*, Institution of Engineering and Technology, **2018**, 6 (5 pp.)-6 (5 pp.).

[97] H. W. Ro, J. M. Downing, S. Engmann, A. A. Herzing, D. M. DeLongchamp, L. J. Richter, S. Mukherjee, H. Ade, M. Abdelsamie, L. K. Jagadamma et al., *Energy Environ. Sci.* **2016**, *9*, 2835.

[98] Y. Li, H. Liu, J. Wu, H. Tang, H. Wang, Q. Yang, Y. Fu, Z. Xie, *ACS Appl. Mater. Interfaces* **2021**, *13*, 10239.

[99] L. Zhang, B. Lin, B. Hu, X. Xu, W. Ma, *Adv. Mater.* **2018**, *30*, e1800343.

[100] W. Ma, J. Reinspach, Y. Zhou, Y. Diao, T. McAfee, S. C. B. Mannsfeld, Z. Bao, H. Ade, *Adv. Funct. Mater.* **2015**, *25*, 3131.

[101] H. A. Becerril, M. E. Roberts, Z. Liu, J. Locklin, Z. Bao, *Adv. Mater.* **2008**, *20*, 2588.

[102] B. S. S. Pokuri, J. Sit, O. Wodo, D. Baran, T. Ameri, C. J. Brabec, A. J. Moule, B. Ganapathysubramanian, *Adv. Energy Mater.* **2017**, *7*.

[103] W. Karcher, *Spectral Atlas of Polycyclic Aromatic Compounds*, Springer Netherlands, Dordrecht, **1988**.

[104] C.-C. Chueh, K. Yao, H.-L. Yip, C.-Y. Chang, Y.-X. Xu, K.-S. Chen, C.-Z. Li, P. Liu, F. Huang, Y. Chen et al., *Energy Environ. Sci.* **2013**, *6*, 3241.

[105] C. H. Peters, I. T. Sachs-Quintana, J. P. Kastrop, S. Beaupré, M. Leclerc, M. D. McGehee, *Adv. Energy Mater.* **2011**, *1*, 491.

[106] S. B. Sapkota, A. Spies, B. Zimmermann, I. Dürr, U. Würfel, *Sol. Energy Mater. Sol. Cells* **2014**, *130*, 144.

[107] C. J. Brabec, S. Gowrisanker, J. J. M. Halls, D. Laird, S. Jia, S. P. Williams, *Adv. Mater.* **2010**, *22*, 3839.

[108] M. Jørgensen, K. Norrman, F. C. Krebs, *Sol. Energy Mater. Sol. Cells* **2008**, *92*, 686.

[109] W. R. Mateker, J. D. Douglas, C. Cabanetos, I. T. Sachs-Quintana, J. A. Bartelt, E. T. Hoke, A. El Labban, P. M. Beaujuge, J. M. J. Fréchet, M. D. McGehee, *Energy Environ. Sci.* **2013**, *6*, 2529.

[110] Y. Ge, X. Xiao, G. Yao, S. Yuan, L. Zhang, W. Zhou, *ACS Appl. Mater. Interfaces* **2021**, *13*, 57664.

[111] G. Dennler, C. Lungenschmied, H. Neugebauer, N. S. Sariciftci, M. Latrèche, G. Czeremuszkin, M. R. Wertheimer, *Thin Solid Films* **2006**, *511-512*, 349.

[112] K. C. Tam, H. Saito, P. Maisch, K. Forberich, S. Feroze, Y. Hisaeda, C. J. Brabec, H.-J. Egelhaaf, *Sol. RRL* **2022**, *6*.

[113] W. Kim, J. K. Kim, E. Kim, T. K. Ahn, D. H. Wang, J. H. Park, *J. Phys. Chem. C* **2015**, *119*, 5954.

[114] L. Chang, I. E. Jacobs, M. P. Augustine, A. J. Moulé, *Org. Electron.* **2013**, *14*, 2431.

[115] M. Revilla-León, S. G. Subramanian, W. Att, V. R. Krishnamurthy, *J. Prosthodontics* **2021**, *30*, 157.

[116] A. K. K. Kyaw, D. H. Wang, D. Wynands, J. Zhang, T.-Q. Nguyen, G. C. Bazan, A. J. Heeger, *Nano Lett.* **2013**, *13*, 3796.

[117] J.-D. Chen, L. Zhou, Q.-D. Ou, Y.-Q. Li, S. Shen, S.-T. Lee, J.-X. Tang, *Adv. Energy Mater.* **2014**, *4*, 1301777.

[118] B.-H. Jiang, H.-E. Lee, J.-H. Lu, T.-H. Tsai, T.-S. Shieh, R.-J. Jeng, C.-P. Chen, *ACS Appl. Mater. Interfaces* **2020**, *12*, 39496.

[119] S. Mishra, S. Ghosh, B. Boro, D. Kumar, S. Porwal, M. Paul, H. Dixit, T. Singh, *Energy Adv.* **2022**, *1*, 761.

[120] L.-K. Ma, Y. Chen, P. C. Chow, G. Zhang, J. Huang, C. Ma, J. Zhang, H. Yin, A. M. Hong Cheung, K. S. Wong et al., *Joule* **2020**, *4*, 1486.

[121] J. Kim, G. Kim, Y. Choi, J. Lee, S. Heum Park, K. Lee, *J. Appl. Phys.* **2012**, *111*.

[122] Z. Ling, Y. Zhao, S. Wang, S. Pan, H. Lian, C. Peng, X. Yang, Y. Liao, W. Lan, B. Wei et al., *J. Mater. Chem. C* **2019**, *7*, 9354.

[123] Y. Wang, L. Yan, G. Ji, C. Wang, H. Gu, Q. Luo, Q. Chen, L. Chen, Y. Yang, C.-Q. Ma et al., *ACS Appl. Mater. Interfaces* **2019**, *11*, 2243.

[124] Z. Hu, L. Ying, F. Huang, Y. Cao, *Sci. China: Chem.* **2017**, *60*, 571.